Heat Transfer and Pressure Drop in Microchannels with Different Inlet Geometries for Laminar and Transitional Flow of Water

by

D.V. Garach

Submitted in the full fulfilment of the requirements of the degree

MASTER OF ENGINEERING in Mechanical Engineering

in the

Faculty of Engineering, Built Environment and Information Technology

University of Pretoria

Supervisors: Dr. J. Dirker and Prof. J.P. Meyer

February 2014

Title: Heat Transfer and Pressure Drop in Microchannels with Different Inlet Geometries for Laminar and Transitional Flow of Water

Author: Darshik Vinay Garach

Student Number: 28475705

Supervisors: Dr J Dirker and Prof JP Meyer

Degree: Master of Engineering (Mechanical)

Department: Mechanical and Aeronautical Engineering

Abstract

This study consists of an experimental investigation into the fluid flow and heat transfer aspects of microchannels. Rectangular copper microchannels of hydraulic diameters 1.05 mm, 0.85 mm and 0.57 mm were considered. Using water as the working fluid, heat transfer and pressure drop characteristics were determined under a constant surface heat flux for different inlet configurations in the laminar and transitional regimes. Three inlet geometries were experimentally investigated: a sudden contraction inlet, a bellmouth inlet and a swirl-generating inlet. The influence of the inlet conditions on the pressure drop, Nusselt number and critical Reynolds number was determined experimentally. Pressure drop results showed good agreement with existing correlations for adiabatic conditions. Diabatic friction factor results for the sudden contraction and bellmouth inlets were overpredicted when using the friction factor results from literature. It is noted that a relationship between the pressure drop and heat flux existed in the laminar regime, where an increase in the heat input resulted in a decrease in the friction factor. The bellmouth inlet condition showed an enhancement of the heat transfer in the transition regime compared with the sudden contraction inlet. The critical Reynolds number for the onset of transition for the sudden contraction inlet was found to be approximately 1 950, with a sharp rise to the turbulent regime thereafter. The bellmouth inlet influenced the originating point of the transition regime, which commenced at a Reynolds number of approximately 1 600. A smoother and more gradual increase to the turbulent regime was observed as an effect of the bellmouth inlet over the sudden contraction inlet. The swirl-generating inlet condition produced higher friction factor results in all three flow regimes. Transition occurred at a Reynolds number of approximately 1 500 and the turbulent regime was quickly

reached thereafter. The turbulent regime friction factor was found to be significantly higher with the swirl inlet compared with both the sudden contraction and bellmouth inlets. Nusselt numbers continued to increase until the onset of the transition regime, and did not converge to a constant value as stated in theory. Similar enhancement of the transition regime with the bellmouth inlet was observed for the Nusselt numbers as with the friction factors. The initial turbulent regime results followed the trend of the theory for both the sudden contraction and bellmouth inlet conditions for most of the data sets, with deviation occurring in some of the 0.57 mm test cases. The swirl inlet Nusselt number results were significantly underpredicted by the theory in the early turbulent regime.

Keywords: microchannel, heat transfer, pressure drop, inlet conditions, single-phase, water

Publications in journals and conferences

Article in related journal

1. DIRKER J, MEYER JP, and GARACH DV, “Inlet flow effects in microchannels in the laminar, transitional, and early turbulent flow regimes on single-phase heat transfer coefficients and friction factors”, Submitted to the International Journal of Heat and Mass Transfer. (Reference Number: HMT-D-13-00415).

Conference paper

1. GARACH DV, DIRKER J, and MEYER JP, “Heat transfer and pressure drop in microchannels with different inlet conditions for water in the laminar and transitional regimes”, Proceedings of the 9th International Conference on Heat Transfer, Fluid Mechanics and Thermodynamics (HEFAT2012), pp. 763 – 770, 16 - 18 July 2012.

Acknowledgements

I would like to thank the following people for their support during my studies:

- My parents, for their unconditional love and support through the good times and the bad. Your love and guidance have inspired me to do my utmost best and overcome the obstacles in front of me. To my brother and sister, whose influence guides me to be a better person. I love you both more than you can imagine.
- My friends, who have supported, assisted, and guided me throughout my life. Thank you for your support, your guidance and your friendship.
- My colleagues at the University of Pretoria, whose company, help and guidance I know to be the reason why I have learnt so much during my studies. Thanks for making this part of my life unforgettable. Special thanks to Louw Coetzee, for his tremendous partnership during our collaboration together, and to Mduduzi Ntuli, for all the assistance and friendship gained both on and off campus. You are good scholars, but friends, there are no better.
- My supervisors, Dr. Jaco Dirker and Prof. Josua Meyer, whose continuous guidance, assistance, enthusiasm and faith in my work have inspired me to do my utmost best.
- Mr. Danie Gouws, whose input and help have been crucial in all my experimental work - you are truly an asset to the department and the students; Mr. Koos Mthombeni, for his continuous assistance and inspiring personality; Mr. Neels Smith, whose guidance and instruction in the workshop ensured the success of this project.

I would like to thank the following people and institutions for their assistance in this study:

- The funding obtained from the NRF, TESP, University of Stellenbosch/ University of Pretoria, SANERI/SANEDI, CSIR, EEDSM Hub and NAC is acknowledged and duly appreciated.
- Mr. Joe de Oliveira of Executive Mould Services. Thank you for the manufacturing of the microchannels used in this study. Your assistance over the period of my work has shed a new light on manufacturing techniques and processes.
- Dr. Suretha Potgieter of the CSIR, Manufacturing and Materials division, whose assistance with laser microscopy has been beneficial in the validation of the surface roughness of the microchannels. Thank you for your assistance and your patience.
- Mr. Tony Wynne of the TUT Centre for Advanced Manufacturing, for the laser manufacturing of the micro-holes in the test section. Thank you for your assistance and input with regard to my studies.

Contents

List of appendices

List of figures

List of tables

Nomenclature

A_c	Channel cross-sectional area	m^2
A_s	Channel wall surface area	m^2
$A_{s,m}$	Material bottom surface area	m^2
Br	Brinkman number	$-$
$C_{1,2}$	Correlation factors of surface material (see Table 3)	$-$
$C_{f,lam}$	Laminar friction factor coefficient (see Table 2)	$-$
$C_{f,turb}$	Turbulent friction factor coefficient (see Table 2)	$-$
C_p	Specific heat of fluid	J/kgK
C_{sl}	Shah and London friction factor constant	$-$
D_h	Hydraulic diameter	m
D_i	Inner-tube diameter	m
D_o	Outer-tube diameter	m
eb	Energy balance	$-$
f	Friction factor	$-$
$f_{blasius}$	Blasius turbulent friction factor	$-$
f_{meas}	Measured friction factor	$-$
f_{pred}	Predicted friction factor	$-$
f_{sl}	Shah and London laminar friction factor	$-$
$\bar{h}$	Average heat transfer coefficient	W/m^2K
H	Microchannel height	m

$\bar{I}$	Average input current (DC)	A
j	Colburn *j*-factor	$-$
k_f	Fluid thermal conductivity	W/mK
k_s	Solid thermal conductivity	W/mK
L	Channel length or entrance length	m
L_{hydro}	Hydrodynamic entrance length	m
L_p	Pressure-drop length	m
$L_{thermal}$	Thermal entrance length	m
$\dot{m}$	Mass flow rate of water	kg/s
M	Axial heat conduction number	$-$
Nu	Nusselt number	$-$
$\overline{Nu}_{Gnielinski}$	Gnielinski average turbulent Nusselt number	$-$
$\overline{Nu}$	Average measured Nusselt number	$-$
$\overline{Nu}_{pred}$	Average predicted Nusselt number	$-$
P	Pressure	Pa
P_w	Wetted perimeter	m
Pr	Prandtl number	$-$
$\bar{q}$	Average channel-surface-area heat flux	W/m^2
$\bar{\dot{Q}}_{in}$	Average heat input by heater	W
$\bar{\dot{Q}}_{out}$	Average power output to water	W
r_a	Channel surface roughness	m
Re	Reynolds number	$-$

$\bar{T}_b$	Average bulk fluid temperature	$°C$
$\bar{T}_{in}$	Average fluid inlet temperature	$°C$
$\bar{T}_w$	Average wall temperature	$°C$
$\bar{T}_{out}$	Average fluid outlet temperature	$°C$
v	Average fluid velocity	m/s
$\bar{V}$	Average input voltage (DC)	V
W	Microchannel width	m
W_b	Bottom width of trapezoidal microchannel	m
W_c	Centre-to-centre distance between microchannels	m
W_t	Top width of trapezoidal microchannel	m
W_m	Microchannel material width	m

Greek Symbols

α	Channel aspect ratio (see Table 2)	$-$
ε	Relative surface roughness	$-$
Δ	Differential	$-$
μ_b	Bulk fluid temperature dynamic viscosity	kg/ms
$\mu_{T_{in}}$	Fluid inlet temperature dynamic viscosity	kg/ms
ρ	Fluid density	kg/m^3

Commonly used abbreviations

GUI	Graphical user interface
$NIDAQ$	National Instruments data acquisition system
$PTFE$	Polytetraflouroethylene
$Sudden\ cont.$	Sudden contraction inlet section

1 Introduction

1.1 Background

Heat exchangers can remove heat from systems effectively, and the requirement of accurate predictability is warranted for modern-day applications. The aspects that require accurate prediction are generally the heat transfer rate and pressure drop across the length of the heat exchanger. With the current improvement in miniaturisation technologies, interest has shifted to heat transfer at a much smaller dimensional scale. This has led to the development of microchannels to provide an effective heat transfer mechanism to miniature systems.

Research into microchannel heat transfer was initially inclined towards the cooling of integrated circuitry. Tuckerman and Pease [1] were the first to document and report on the use of microchannels for such applications. This sparked an increase in the amount of interest into the heat transfer mechanisms involved in this very effective and efficient heat exchange method. It was motivated that the idea might not only be confined to electronic cooling applications. As a result, microchannel flow became an independent research area in the field of heat transfer. Nowadays, the concept of microchannels is still not established well enough to be considered accurately predictable. There have been many inconsistencies with the experimental pressure drop and heat transfer results since the commencement of microchannel studies. The behaviour of heat transfer mechanisms and friction factors in microchannels is generally case-specific, resulting in disagreement with the conventional theory used with the prediction of similar macrochannel systems. With such result variations in the experimental microchannel field, numerical and analytical methods have been employed to determine the causes for deviations and/or methods to correct them. A combination of experimental and numerical work is common and there seems to be a great dependency on numerical work to validate case-specific experimental results.

In the next section, an in-depth literature survey is presented to compare and discuss the results of studies conducted over the period since the establishment of single-phase microchannel flow and heat transfer. The conclusions from the literature research drive the motivation required for this study, and a new outlook on experimental microchannel work is required to surpass the inconsistency that has stemmed from previous studies.

1.2 Previous work

As previously mentioned, microchannel flow was first applied to heat transfer applications by Tuckerman and Pease [1]. The work involved a multiport microchannel system of rectangular cross-sectional shape to enhance the heat transfer from a constant heat flux boundary condition. They were able to remove a maximum of 790 W/m^2 with water, stating that their flow conditions were very well predicted by conventional theory. This first attempt at improving heat transfer in small heat-dissipating objects proved to be ground-breaking, and the interest in microchannels pursued.

Peng and Peterson [2] thereafter experimentally tested multiport microchannels. Their experiments utilised stainless steel channels rather than the fused silica used in the work of Tuckerman and Pease. With rectangular channels, and using water as their working fluid, they reported that the measured friction factor was either lower than that in the conventional theory, or higher, depending on the hydraulic diameter. They proposed a correlation to predict the pressure drop along the length of a microchannel. Similarly, they noticed deviations in their Nusselt number values, and proposed correlations for both the laminar and turbulent regimes. Their results indicated that transition to turbulence occurred between a Reynolds number of 2 000 and 3 000.

Shortly after the work of Peng and Peterson, Mala and Li [3] conducted adiabatic experiments in circular microchannels manufactured in stainless steel and fused silica. Their findings showed that there was early transition-to-turbulence occurring for both materials, and the friction factor was predictable by theory up to a Reynolds number of 500. Thereafter, the friction factor increased, which was interpreted as the beginning of the transitional regime. They conducted their experiments in channels smaller than 0.254 mm.

Weilin *et al.* [4] experimentally measured the pressure drop along the length of trapezoidal-shaped microchannels manufactured from fused silica. With an adiabatic boundary condition, they reported an increase in friction factor over the conventional theory for microchannels smaller than 0.17 mm. They were some of the first to also report on the microchannel surface roughness, measuring a relative surface roughness between 1.24% and 1.75%. Reporting that the friction factor deviates at a Reynolds number of 500, they suggested that the deviation is due to the surface roughness and proposed a roughness-viscosity model to predict the pressure drop in a microchannel.

In the same year, Harms *et al.* [5] conducted experiments on rectangular microchannels with a constant surface heat flux boundary condition. The hydraulic diameters ranged from 0.4 mm to 1.9 mm, and were etched from fused silica. Two test sections were manufactured, one with a single

channel, and the other with an array of channels. They reported that the friction factor is predicted well by conventional theory and the transition to turbulence occurred at a Reynolds number of 1 500. They reported higher Nusselt number values, noting exceptionally higher values for the single channel. They assumed that this is a result of the 'inlet bend', where the water entered the test section via a port, was placed perpendicularly to the orientation of the test section.

The effect of various fluid media was explored by Judy *et al*. [6]. They experimentally tested water, methanol and isopropanol in square and circular channels manufactured from fused silica and stainless steel. They ran their experiments under adiabatic conditions for microchannels with diameters varying from 0.015 mm to 0.15 mm. They did not report on the surface roughness, but found good agreement of the friction factor with conventional theory. Their experiments were conducted in the laminar regime and they noticed that the onset of transition occurs at a Reynolds number of 2 000 for the stainless steel test section.

Hegab *et al.* [7] tested refrigerant R134a as the working fluid for single-phase microchannel flow in rectangular channels smaller than 0.21 mm. With a constant heat flux boundary condition, the friction factors and Nusselt numbers were measured and compared with conventional theory. They reported lower friction factor values for the transition and turbulent regimes, and provided correlations to predict the pressure drop along the channel. The transition regime occurred between a Reynolds number of 2 000 to 4 000, with turbulent flow noticed thereafter. Heat transfer results were measured in the turbulent regime, and the Nusselt number deviated between 6% and 84% from the Gnielinski equation. They then proposed a correlation for the prediction of the Nusselt number for Reynolds numbers between 4 000 and 15 000.

A well-documented paper on a constant surface temperature boundary condition was produced by Celata *et al.* [8] in 2004. They conducted experiments on circular channels manufactured from fused silica. A constant surface temperature boundary condition was used and the added heat was removed with water. They reported mixed results, with both equal and increased friction factor measurements for channels of hydraulic diameters between 0.08 mm to 0.17 mm. The transitional regime occurred between a Reynolds number of 1 900 and 2 500 with turbulent flow following thereafter. The Nusselt number was reported to deviate in the laminar regime and was correlated in the turbulent regime using the turbulent Gnielinski equation. They reported the relative surface roughness to be less than 0.1%.

In 2004, Garimella and Singhal [9] micro-milled rectangular test sections from stainless steel of hydraulic diameters ranging from 0.25 mm to 1 mm. They measured the pressure drop along the

channel length, and found no sign of severe deviation from conventional theory. The laminar and turbulent regime pressure drop measurements agreed well, and they found that the transition regime occurred between a Reynolds number of 2 000 and 2 800. With regard to the Nusselt number, they noted that the Nusselt number increased in the laminar regime as the Reynolds number increased, and did not converge to a constant value. They concluded that more work into heat transfer in microchannels must be done to gain further insight into why this increase occurs.

Hao *et al.* [10] conducted experiments on water in a trapezoidal fused-silica channel of diameter 0.24 mm. Conducting adiabatic experiments, they measured the pressure drop along the length of a single microchannel. They concluded that conventional theory can predict the friction factor behaviour for values of Reynolds number lower than 1 400, noting that transition occurred between 1 500 and 1 800. Their relative surface roughness was measured at 0.03%.

Steinke and Kandlikar [11] conducted experiments on a multichannel microchannel test section in the laminar regime with water. They conducted adiabatic experiments with a test section consisting of 26 rectangular channels of dimensions 0.20 mm x 0.25 mm. Experimentally testing to a Reynolds number of 800, they noticed that the friction factors would increase unpredictably after a Reynolds number of 300. By correcting for developing flow, they reduced the high deviation from conventional theory. They then documented the measured friction factor at 33% higher than what conventional theory predicts. They reported that the uncertainty in microchannels is very high with regard to inlet and exit pressure losses, and channel geometry, and put emphasis for future work on the accurate measurement of geometric details.

Hrnjak and Tu [12] conducted experiments on five test sections manufactured from polyvinyl chloride (PVC). They used refrigerant R134a as their working fluid, and ran adiabatic liquid and vapour tests in channels of hydraulic diameters ranging from 0.07 mm to 0.31 mm. Looking at only the liquid-phase results, the authors concluded that the laminar friction factor can be predicted using conventional theory, noting a 9% increase over the predicted values. They found that transition occurred at a Reynolds number between 2 150 and 2 290. The turbulent regime results showed an increase in friction factor of up to 30%. The channels had a relative surface roughness less than 0.3%.

Natrajan and Christensen [13] experimented on a single copper microchannel and varied the wall surface roughness. This was done using replaceable channel walls of different roughness. Using a 0.6 mm rectangular channel, they conducted both friction factor and Nusselt number measurements, concluding that both are predictable by conventional theory. Their results showed that by increasing

the surface roughness, the critical Reynolds number was lowered from 1 800 to 1 300. Full turbulence occurred thereafter between Reynolds numbers of 2 300 and 2 700 depending on the experiment.

Morini *et al.* [14] conducted experiments in stainless steel microchannels of diameters between 0.146 mm and 0.440 mm using water, and 0.280 mm using coolant FC-72. They conducted their research in the laminar and transition regime, testing only the Nusselt number. They found that the transition in heat transfer occurred between a Reynolds number of 2 380 and 3 100 for water, and at 2 430 for FC-72. The Sieder and Tate [15] correlation was found to underpredict the Nusselt number in the laminar regime.

In order to clarify the effect the surface roughness has on a microchannel, Li *et al.* [16] conducted experiments in fused silica and stainless steel microchannels, with the stainless steel variants having the roughened surface. The fused silica hydraulic diameters ranged from 0.05 mm to 0.1 mm, while the stainless steel channels ranged from 0.373 mm to 1.570 mm. With a single channel test section, they conducted both pressure and heat transfer experiments in the laminar regime and concluded that there is good correlation between their measured friction factor and conventional theory. Their Nusselt number results were lower than predicted for low values of Reynolds number, and converging to the constant theoretical value at a Reynolds number above 100. They owe this to the interpretation of the bulk fluid temperature, stating that a linear approximation may be a cause of deviation. They also concluded that the axial heat conduction effect must be taken into consideration when conducting low Reynolds number experimentation with microchannels.

Park and Punch [17] conducted experiments in multichannel microchannels for friction factor and Nusselt number experiments on hydraulic diameters ranging between 0.106 mm and 0.307 mm. They found that the friction factor can be predicted using conventional theory, with results falling within a range of ±20%. Their reported Nusselt number values were found to be different from conventional theory and they proposed a correlation for predicting the heat transfer through their microchannels with respect to the Brinkman number.

Considering the discussed research, there is a high inconsistency in the conclusions reported by researchers in the field of microchannels. There is very little consensus in the theory for the prediction in these small heat exchangers, with many authors – some mentioned above - reporting that the conventional heat transfer and pressure drop correlations are not adequate. A comparison of the research discussed above and that of other research conducted in microchannels is tabulated

in Table 1. With it, the geometry, material and manufacturing, boundary conditions and the important results associated with single-phase liquid flow in microchannels can be compared.

It can be concluded from table 1 that the most common single-phase liquid used in microchannel experimentation is water, with a few researchers testing with R134a, methanol and isopropanol. For different investigations, thermal boundary conditions were varied. In some cases, no thermal boundary condition was used (adiabatic tests). A constant heat flux and constant wall temperature boundary conditions are the two most common thermal boundary conditions. Adiabatic tests focus on the friction factor associated with microchannels, while with a constant heat flux or wall temperature boundary conditions, the Nusselt number and/or friction factor is measured. The material used and the manufacturing method of the microchannel determines the surface roughness of the walls of the channel. The most common materials used for the test sections are fused silica, aluminium and stainless steel. Two groups of researchers, Jiang *et al.* [18] and Natrajan and Christensen [13], used copper, while Gamrat *et al.* [19] used bronze. Microchannels manufactured from fused silica were etched out of the material, and the lid was anodically bonded to the base material, which consists of the channel(s). The channel hydraulic diameter (D_h) and surface roughness (r_a) determine the relative surface roughness (ε). Fused silica can yield smaller hydraulic diameter channels as the etching process can be well controlled. Manufacturing channels from metals requires a material removal process.

Table 1 also indicates how researchers' results compared with conventional theory. Research was either conducted on single- or multichannel test sections of different materials. Authors measured either lower ($<$) or higher ($>$) friction factors and Nusselt numbers with respect to conventional theory, with some researchers such as Peng and Peterson [2] reporting both increased and decreased values of friction factor in their study ($<, >$). For some such cases, semi-empirical correlations were published for the prediction of the friction factor (Table 2) and Nusselt number (Table 3) in the laminar and turbulent regimes. Many authors have also concluded that the conventional theory holds for the prediction of the friction factors ($=$) and did not find any drastic deviation from the theory.

The critical Reynolds numbers are also compared with each other in Table 1. Different values of critical Reynolds number have been reported. Comparing the measured and theoretical friction factors (*f*) also shows differences in the published results. The results of the Nusselt number comparison (*Nu*) show even less conformity to theory. This offers very little confidence in the current predictive models.

A review paper by Morini [20] suggests that with the improvement of technology, geometrical characterisation has improved and measurement uncertainties – which play a major role in the analysis of data on micro-scale – have been reduced. The implications are that recent work in microchannels should rather be taken into consideration when comparing publications.

Ref	*Year*	*Author*	*Fluid*	*Cross-section*	*Material*	*Fabrication*	*Channels*	*Boundary condition*	*Diameter [μm]*	*Relative roughness*	*Critical Re*	*f*	*Nu*
[1]	1981	Tuckerman, Pease	Water	Rectangular	Fused silica	Etching	Multi	Constant heat flux	86 – 95	-	2 300	-	-
[2]	1996	Peng, Peterson	Water	Rectangular	Stainless steel	Milling	Multi	Constant heat flux	133 – 267	-	2 000 – 3 000	<>	<
[21]	1997	Jiang *et al.*	Water	Trapezoidal	Fused silica	Etching	Single	Adiabatic	6 – 18	-	-	<	N/A
			Water	Circular	Fused silica	Etching	Single		8 – 420	-	-	=	
[3]	1999	Mala, Li	Water	Circular	Fused silica	Etching	Single	Adiabatic	50 – 250	-	300 – 900	>	N/A
			Water	Circular	Stainless steel	Milling	Single		64 – 254	-	500 – 1 500	>	
[5]	1999	Harms *et al.*	Water	Rectangular	Fused silica	Etching	Multi	Constant heat flux	404 – 1 923	0 - 0.02%	1 500	=	≥
[4]	2000	Weilin *et al.*	Water	Trapezoidal	Fused silica	Etching	Single	Adiabatic	51 – 169	1.24 - 1.75%	-	>	N/A
[22]	2000	Xu *et al.*	Water	Rectangular	Aluminium	Milling	Single	Adiabatic	47 – 344	0.0015 - 0.011%	2 300	=	N/A
				Rectangular	Fused Silica	Etching	Single		30 – 79	± 0%	2 300	=	
[6]	2002	Judy *et al.*	Water	Square	Fused silica	Etching	Single	Adiabatic	50 – 100	-	2 300	=	N/A
			Methanol	Circular	Fused silica	Etching	Single		15 – 150	-	2 300	=	
			Isopropanol	Circular	Stainless steel	Milling	Single		75 – 125	-	2 300	=	
[7]	2002	Hegab *et al.*	R134a	Rectangular	Aluminium	Milling	Multi	Constant heat flux	112 – 210	0.16 - 0.74 %	2 000 – 4 000	<	<
[23]	2003	Wu, Cheng	Water	Trapezoidal	Fused silica	Etching	Single	Adiabatic	49 – 291	< 0.12%	1 500 – 2 000	=	N/A
				Triangular	Fused silica	Etching	Single		26 – 103		1 500 – 2 000	=	
[24]	2004	Lelea *et al.*	Water	Circular	Stainless steel	Drilling	Single	Constant heat flux	125 – 500	-	-	=	=
[8]	2004	Celata *et al.*	Water	Circular	Fused silica	Etching	Single	Constant wall temperature	80 – 166	< 0.10%	1 800 – 2 500	≥	
[9]	2004	Garimella, Singhal	Water	Rectangular	Stainless steel	Milling	Single	Constant wall temperature	250 – 1 000	-	2 000	=	≥
[25]	2004	Chen *et al.*	Methanol	Triangular	Fused silica	Etching	Multi	Constant heat flux	57 – 267	-	2 300	=	-
[26]	2004	Owhaib, Palm	R134a	Circular	Stainless steel	-	Single	Constant heat flux	800 – 1 700	-	-	=	=
[19]	2005	Gamrat *et al.*	Water	Rectangular	Bronze	-	Multi	Constant heat flux	100 – 1 000	-	-	-	<
[27]	2005	Zhang *et al.*	Water	Rectangular	Aluminium	Milling	Multi	Constant heat flux	420	0.55%	-	<	=
[10]	2005	Hao *et al.*	Water	Trapezoidal	Fused silica	Etching	Single	Adiabatic	237	0.03%	1 500 – 1 800	≤	N/A
[28]	2005	Kang *et al.*	Water	Rectangular	Fused silica	Etching	Multi	Constant heat flux	80 – 333	-	-	-	-
[29]	2005	Colgan *et al.*	Water	Rectangular	Fused silica	Etching	Multi	Constant heat flux	108	-	-	>	>
[11]	2006	Steinke, Kandlikar	Water	Rectangular	Fused silica	Etching	Multi	Adiabatic	26 – 222	0.20%	-	<	N/A
[12]	2007	Hrnjak, Tu	R134a	Rectangular	Polyvinyl-chloride	Milling	Multi	Adiabatic	70 – 305	0.14 - 0.35%	2 150 – 2 290	=	N/A
[16]	2007	Li *et al.*	Water	Circular	Fused silica	Etching	Single	Constant heat flux	50 – 100	-	2 300	=	≥
			Water	Circular	Stainless steel	Etching	Single		373 – 1 570	0.95% - 2.4%	2 300	≥	
[30]	2007	Costaschuk *et al.*	Water	Rectangular	Aluminium	Milled	Single	Adiabatic	169	0.10%	2 370	=	N/A
[31]	2007	Mishan *et al.*	Water	Rectangular	Aluminium	Milling	Multi	Constant heat flux	440	2.30%	-	-	=
[32]	2008	Gamrat *et al.*	Water	Rectangular	Fused silica	Etching	Multi	Adiabatic	100 – 300	4.00 - 15.00%	2 000	=	N/A
[33]	2008	Jung, Kwak	Water	Rectangular	Fused silica	Etching	Multi	Constant heat flux	100	0.15 - 0.17%	-	=	>
[17]	2008	Park, Punch	Water	Rectangular	Fused silica	Etching	Multi	Constant heat flux	106 – 307	0.007% - 0.02%	-	=	<>
[18]	2008	Jiang *et al.*	Water	Rectangular	Copper	Milling	Multi	Constant heat flux	126	-	1 100	<	≥
[34]	2009	Wang *et al.*	Water	Trapezoidal	Fused silica	Etching	Single	Constant heat flux	155	-	-	-	=
[35]	2009	Wibel, Ehrhard	Water	Rectangular	Stainless steel	-	Single	Constant wall temperature	128 – 144	1.40 - 1.50 %	1 900 – 2 200	-	-
[13]	2010	Natrajan, Christensen	Water	Rectangular	Copper	Milling	Single	Constant heat flux	600	0.015 - 2.51%	1 800 – 1 300	=	≥
[14]	2010	Morini *et al.*	Water	Circular	Stainless steel	-	Single	Constant heat flux	146 – 440	4.11 - 0.68%	2 380 – 3 100	-	>
			FC-72 Coolant	Circular	Stainless steel	-	Single	Constant heat flux	280	1.07%	2 430	-	
[36]	2011	Barlak *et al.*	Water	Circular	Stainless steel	Milling	Single	Adiabatic	200 – 589	-	2 000 – 2 500	=	N/A
[37]	2011	Moharana *et al.*	Water	Rectangular	Copper	Milling	Multi	Constant heat flux	907	0.364%	1 100	>	>

Table 1 Comparison of experimental literature over the past 30 years comparing the fluid, cross-section, fabrication, number of channels, boundary conditions, hydraulic diameter, relative roughness, critical Reynolds number, friction factor and Nusselt number. Friction factors and Nusselt numbers are given to be either lower (<), higher (>), or equal to (=) the conventional macrochannel theory

Where deviations have been found in the friction factors, a few authors have produced their own semi-empirical correlations to predict the friction factor in microchannels. Table 2 lists some of these semi-empirical correlations, as well as the Reynolds number range of their applicability.

Author	*Ref*	*Fluid*	*Correlation*	*Regime*
Peng & Peterson	[2]	Water	$f = \frac{C_{f,lam}}{Re^{1.98}}$	$Laminar$
			$f = \frac{C_{f,turb}}{Re^{1.72}}$	$Turbulent$
Hegab et al.	[7]	Refrigerant R134a	$f = \frac{64}{Re}\ (Poiseuille)$	$Laminar$
			$f = 0.000173Re^{0.646}$	$Transition$
			$f = \frac{0.611}{Re^{0.35}}$	$Turbulent$
Wu & Cheng	[23]	Water	$f = \frac{1}{Re}\{11.43 + 0.8e^{2.67\alpha}\}$	$Laminar$

Table 2 Semi-empirical friction factor correlations developed by previous experimental research

Figure 1 compares the results correlations in Table 2. Peng and Peterson [2] produced case-specific equations that require different coefficients ($C_{f,lam}$ and $C_{f,turb}$), which depend on the layout of the test section. Two coefficients of $C_{f,lam} = 109\,000$ $C_{f,turb} = 38\,600$ were chosen based on a channel aspect ratio of 1. Hegab *et al.* [7] developed correlations to describe the friction factor in the transition and the turbulent regimes, stating that the Poiseuille equation holds for the laminar regime. The correlations derived by Wu and Cheng [23] differ vastly from conventional theory.

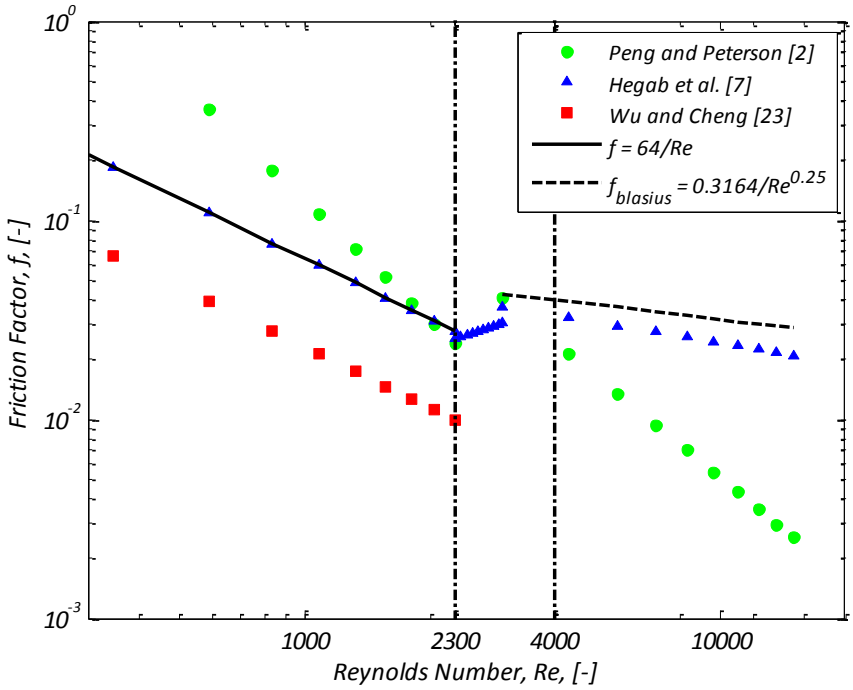

Figure 1 Comparison of semi-empirical friction factor correlations for water flowing through a microchannel of hydraulic diameter 1 mm and an aspect ratio of 1, evaluated at a temperature of 20°C

Though the correlations of Hegab *et al.* are for refrigerant R134a, they were conducted under single-phase flow and could be applicable to the friction factor prediction using water as the working fluid. Figure 1 shows the very large differences in the results of these authors, with only Hegab *et al.* reporting similar results to the conventional theory of Poiseuille flow in the laminar regime. Peng and Peterson's results have a much steeper gradient to the theory in both the laminar and turbulent regimes, while Wu and Cheng, who only reported the friction factors in the laminar regime, reported results lower but parallel to the macrochannel theory. Peng and Peterson and Hegab *et al.* reported lower results in the turbulent regime compared with the Blasius equation.

Correlations were also developed for the Nusselt number prediction in microchannels. Figure 2 is a plot of these semi-empirical correlations found in Table 3. The results of the Nusselt number correlations differ vastly from each other and from the conventional theory. Peng and Peterson [2] reported lower Nusselt numbers in the turbulent regime than those of the theory, while reporting an increasing Nusselt number in the laminar regime. Hegab *et al.* [7] reported very high turbulent Nusselt numbers, while Park and Punch [17] and Wu and Cheng [23] reported very high laminar Nusselt numbers. Jung and Kwak [33] reported low but increasing Nusselt numbers in the laminar regime. The results were plotted for a Prandtl number of 7 and a constant Brinkman number of 5×10^{-8}.

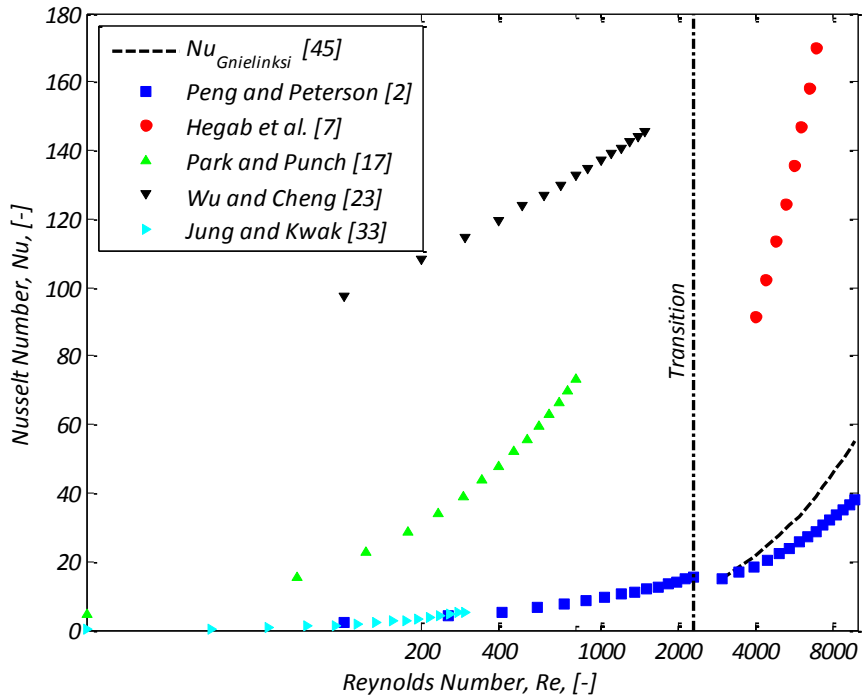

Figure 2 Comparison of semi-empirical Nusselt number correlations for the flow of water in a microchannel of hydraulic diameter 1 mm, aspect ratio 1 and a Prandtl number of 7.

Author	Ref.	Cross-section	Fluid	Correlation	Range
Peng & Peterson	[2]	Rectangular	Water	$Nu = 0.1165\left(\frac{D_h}{W_c}\right)^{0.81}\left(\frac{H}{W}\right)^{-0.79}Re^{0.62}Pr^{\frac{1}{3}}$	$Re < 1000$
				$Nu = 0.072\left(\frac{D_h}{W_c}\right)^{1.15}\{1-2.421(\alpha-0.5)^2\}Re^{0.8}Pr^{\frac{1}{3}}$	$1500 < Re < 4000$
Hegab et al.	[7]	Rectangular	Refrigerant R134a	$Nu = 0.003561Re^{1.1306}Pr^{0.4}$	$4000 < Re < 15000$
Park & Punch	[17]	Rectangular	Water	$Nu = 0.015Br^{-0.22}Re^{0.62}Pr^{\frac{1}{3}}$	$Re < 800$
Wu and Cheng	[23]	Trapezoidal	Water	$Nu = C_1Re^{0.946}Pr^{0.488}\left(1-\frac{W_b}{W_t}\right)^{3.547}\left(\frac{r_a}{D_h}\right)^{0.041}\left(\frac{W_t}{L}\right)^{-3.577}\left(\frac{D_h}{L}\right)^{1.369}$	$10 < Re < 100$
				$Nu = C_2Re^{0.148}Pr^{0.163}\left(1-\frac{W_b}{W_t}\right)^{0.908}\left(\frac{r_a}{D_h}\right)^{0.033}\left(\frac{W_t}{L}\right)^{-1.001}\left(\frac{D_h}{L}\right)^{0.798}$	$100 < Re < 1500$
Jung & Kwak	[33]	Rectangular	Water	$Nu = 0.00058Re^{1.15}Pr^{\frac{1}{3}}\left(\frac{\mu_{T_{in}}}{\mu_b}\right)^{2.78}\left(\frac{W}{H}\right)^{0.3}$	$Re < 300$

Table 3 Semi-empirical Nusselt number correlations developed by previous experimental research

The semi-empirical correlations given in Table 3 show the extent of the variation of results obtained in experimental Nusselt number research. These are but a few of the proposed correlations, with Morini [20] stating a few others not represented here. The variation in results is as recent as 2007 when Jung and Kwak developed a correlation to predict the Nusselt number for flows lower than a Reynolds number of 300.

As a result of the non-conforming published results and the proposal of new correlations, stagnation in the prediction of single-phase microchannel friction factors and Nusselt numbers still exists. The question that has been posed is whether the Navier-Stokes equations are valid for such small channels or if new theory must be established.

More recent work by authors such as Costaschuk *et al.* [30], and Wibel and Ehrhard [35], has focused on the effects that are responsible for the reported deviations in the frictional and/or heat transfer behaviour in microchannels. A major influence on heat transfer in microchannels is the axial heat conduction effect, which has been shown to affect the Nusselt number values in the laminar regime.

1.3 The effect of axial heat conduction

Axial heat conduction is an effect that influences the average heat transfer coefficient, as measured by conventional techniques. It depends highly on three dominating factors:

- Thermal conductivity of material
- Thickness of the material around the channel
- Fluid mass flow rate

Under thermal heat flux conditions, the channel material temperature rises. With the lowest fluid temperature at the inlet of the channel and the highest at the exit, the wall temperature is varied along the length of the channel. At low flow rates, there is a large fluid temperature gradient between the inlet and exit, and this also applies to the wall temperature gradient. When there is excessive wall material, there is a stronger thermal gradient effect. This thermal gradient allows a dominating conductive component to exist within the wall, changing the temperature profile of the wall, hence changing the applied boundary condition.

The influence of the axial heat conduction was analytically and numerically determined by Maranzana *et al.* [38]. They established the relationship between three non-dimensional parameters

that affect a general channel flow problem. Combining the Biot number, the number of transfer units, and the wall size ratio, they established a relation between the conductive and convective components of internal flow. This is expressed by the axial heat conduction number M, defined by equation (1).

$$M = \left(\frac{k_s}{k_f}\right)\left(\frac{D_o^2 - D_i^2}{D_i L}\right)\frac{1}{Re\ Pr} \leq 0.01 \qquad (1)$$

When M is less than 0.01, the effect of the axial heat conduction can be neglected as it does not affect the thermal boundary condition significantly. For research conducted before this criterion was established, the axial heat conduction effect was not determined as the cause of the deviation of the Nusselt number from conventional theory. The axial heat conduction causes a reduction in the heat transfer coefficient measurement when compared with conventional theory. By assuming the bulk temperature to be linear and the wall conduction to be one-dimensional, the mean heat transfer coefficient is calculated lower than the actual value. When using the conventional experimental and data-analysis methods, the Nusselt number is measured lower.

Due to this effect, care must be taken when designing a microchannel test section. The axial heat conduction effect must be calculated and documented to ensure that its effect is accounted for. The literature shows that prediction methods of friction factors and Nusselt numbers for microchannels are not established as well as for macrochannel flow. The comparisons made in Table 1 show the high discrepancy in results, especially before the year 2000. Thereafter, better consensus has been reached with respect to friction factor prediction, but factors such as the axial heat conduction, inlet conditions, and the number of channels in a test section still dominate the Nusselt number results.

1.4 Inlet Conditions

The effect on inlet conditions has been experimentally investigated by researchers such as Tam and Ghajar [39] and Olivier and Meyer [40] for macrochannel test sections. Both their research reported a delayed transition regime substantially with the addition of a bellmouth inlet. With respect to microchannels, research into inlets has not been actively investigated. The effect of the addition of inlets is therefore a potential area for improvement of microchannel heat transfer.

1.5 Purpose of the study

The purpose of this study is to experimentally determine the single phase heat transfer and pressure drop characteristics of a single phase fluid in microchannels with different inlet configurations for laminar and transitional flow.

1.6 Scope of study

The fluid being considered was limited to water and the microchannels were heated at a constant heat flux. Three square cross-sectional test sections of copper were manufactured, with hydraulic diameters of approximately 1.05 mm, 0.85 mm and 0.57 mm. The base material length was kept constant for all the test sections at 200 mm. Three inlet conditions were manufactured and tested on the 1.05 mm channel, while two inlet conditions were tested on the 0.85 mm and the 0.57 mm channels. The effect of inlet conditions on the pressure drop and heat transfer was experimentally determined. For each test case, three heat fluxes were applied to each test scenario to compare the effects of the inlet condition over a wide range of experiments. Experimentation was conducted in the laminar and transitional regimes. The results were compared with conventional theory used in the prediction of macrochannel flow for the friction factor and Nusselt number.

1.7 Overview of the thesis

This thesis documents experimental work and data analysis associated with the determination of the friction factors and Nusselt numbers associated with heat transfer in microchannels. The experimental facility is discussed (Chapter 2), as well as the test section. The experimental procedure is discussed and a data analysis methodology is proposed (Chapter 3). Finally, the results are determined and compared with each other and with the analytical theory (Chapter 4). The results are discussed in Chapter 5, and the thesis is concluded with proposals for future work in the determination of the effects of inlet conditions for diabatic flow in microchannels.

2 Experimental facility

2.1 Introduction

A test facility was constructed to experimentally investigate the heat transfer and pressure drop characteristics in microchannels. From the literature research, it is clear that the test facility and test section design must be approached very carefully, considering that the equipment must provide sufficient operating conditions for these very small channels. A test facility was designed to meet the requirements of the proposed test sections (discussed in Section 2.3). Once the test facility construction was completed, the test sections were manufactured and assembled.

2.2 Test facility design

A test facility for microchannels requires specific instrumentation to meet the requirements of low flow rate and low heat transfer operating conditions. Due to the nature of this study, equipment selection played a major role in ensuring that the outcomes of the study were met.

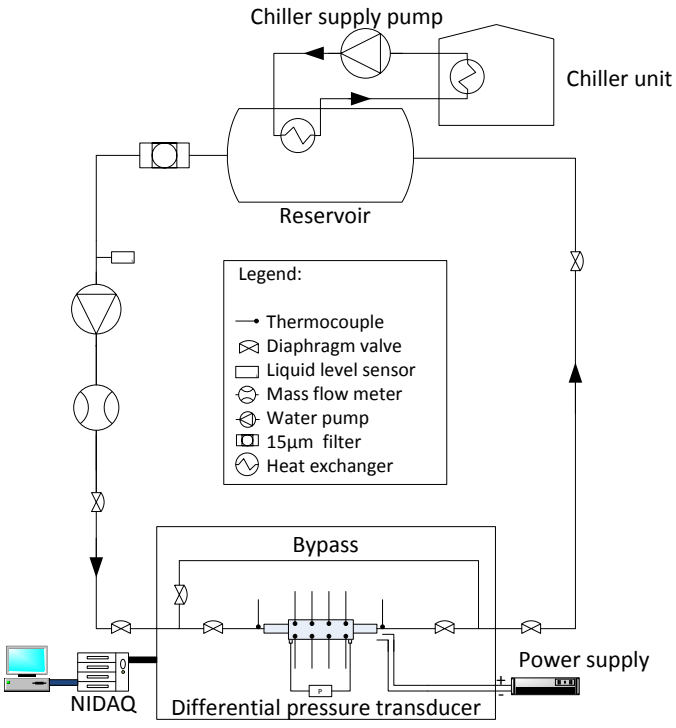

Figure 3 Schematic diagram of microchannel test facility

A closed-loop system was employed to conduct the experimental work. A schematic diagram of the facility is given in Figure 3. Water was pumped through the test facility and the test section, where it absorbed the heat that was applied to the test section. A separate coolant loop could be used to remove the heat from this main loop and control the water temperature in the reservoir. The test facility used 6.35 mm (1/4 inch) copper refrigeration tubing to connect the system components together. The piping was insulated to reduce heat transfer to the ambient. Using valves positioned around the system loop and the test section as shown in Figure 3, water was redistributed away from the test section via a bypass line when necessary. During testing conditions, the bypass valve remained fully closed.

Water stored in the reservoir flowed through a 15 μm filter and a liquid level sensor before reaching the pump. If air particles were detected by the sensor, the pump was automatically switched off. An *Ismatec BVP-Z standard* analogue gear pump was used to provide pulseless flow at low flow rates. The pump had interchangeable head units, which could be used to produce different flow rate ranges at different pressure ratings. A single head unit was used for experimentation, and its specifications are given in Table 4.

	Quantity	***Units***
Model	1 830	-
Minimum flow rate	5	*ml/min*
Maximum flow rate	550	*ml/min*
Maximum system pressure	2 100	*kPa*
Maximum differential pressure	520	*kPa*
Maximum operating temperature	177	*°C*

Table 4 Gear pump specifications

The mass flow rate was measured using a *CMF10 Micro Motion* Coriolis mass flow meter. This flow meter was able to provide a relatively high accuracy reading at low flow rates. The mass flow meter had a full-scale measurement value of 1.36 kg/min with a standard uncertainty of 0.05% of the measurement value.

A *Kwikot 150 litre* geyser unit was used as the reservoir and was chosen due to its large storage capacity and insulated walls. This unit was sized to keep the water at a relevant constant temperature by damping out significant ambient temperature fluctuations which could alter the stored water temperature. A coiled heat exchanger was embedded in the reservoir, which was connected to the laboratory chiller unit. This could aid in cooling the water stored within the reservoir, controlling a specific temperature that could be maintained for the duration of the testing.

The equipment measurement and control were conducted using a *National Instruments* data acquisition system (NIDAQ). Their proprietary control software, *Labview V9.0*, was used to provide a control and measurement graphical user interface. The NIDAQ controlled the pump while measuring the mass flow rate, differential pressure, temperatures and power supply outputs simultaneously. A four-slot chassis contained the terminal cards that were used for the investigation.

The differential pressure measurement was done using a *Validyne DP15* differential pressure transducer. This pressure transducer had interchangeable diaphragms, which were used to measure different pressure ranges. The DP15 provided a low millivolt output of 0 – 35 mV, and required a signal conditioner to upscale this reading to a 0 – 10 V, which was compatible with the NIDAQ. A *CD280* signal conditioner was used for this upscaling procedure. The CD280 could be interfaced with up to four pressure transducers, each with its own dedicated *zero* and *span* dials for calibration.

Heating of the test section was done using a custom-built resistance heater element. The power input to the heater element (which was located under the test section) was supplied by a DC power supply. The *Kikusui PWR800M* DC power supply could provide up to 800 W while maintaining a constant supply of voltage and current. The specifications of the power supply are found in Table 5. The voltage and power output could be controlled either via the NIDAQ or manually using the control dials on the unit. The voltage and current values of the set power output were measured via the power supply's output card. The signals were interfaced with the NIDAQ and logged using the *LabView V9.0* software.

	Quantity	***Units***
Maximum voltage output	320	*V*
Maximum current output	12.5	*A*
Rated power	800	*W*
Noise specification	140	*mV (peak-to-peak)*
Transient response time	8	*ms*
Voltage line regulation	0.05% (of reading) + 3	*mV*
Current line regulation	0.1% (of reading) + 10	*mA*
Voltage control signal	0 – 10	*V*
Voltage monitoring signal	0 – 10	*V*
Current monitoring signal	0 - 10	*V*

Table 5 DC power supply specifications

The heater element was manufactured from constantan wire. Constantan wire offers a high reluctance and therefore yields a high resistance value. The heater element specifications are given

in Table 6. Since a small wire gauge constantan element was used, a low current was required to prevent the heater element from short-circuiting. This higher resistance heater therefore required high voltage and low current inputs to provide the desired power output. Both the voltage and current values were logged to determine the heat input to the test section.

	Quantity	***Units***
Maximum voltage input	320	*V*
Maximum current input	2.054	*A*
Maximum power output	657	*W*
Length	3.724	*m*
Calculated resistance	156	Ω
Measured resistance, T = 25°C	154	Ω
Change in resistance for 0-100°C	0.234	Ω
Constantan reluctance	4.89×10^{-7}	$\Omega \cdot m$

Table 6 Heater element specifications

Twenty-four *Omega T-type* thermocouples were used to measure the temperatures in the test sections. Two different gauge wires were used for the different measurement locations, gauge #30 and gauge #40, and their specifications are given in Table 7.

	Gauge #30	***Gauge #40***	***Units***
Wired diameter	0.25	0.08	*mm*
Thermocouple dimensions (with sheathing)	0.6 x 1.0	0.4 x 0.7	*mm x mm*
Length	3	3	*m*
Standard uncalibrated uncertainty	0.25	0.25	*°C*
Junction bonding method	Soldered	Fused	-

Table 7 Thermocouple wire specifications

Multiple thermocouples were used at certain locations (see Table 8) to provide a more precise temperature measurement. The wall thermocouples were placed at four stations along the length of the channel, with two thermocouples located per station, measuring on the left and right wall. Four inlet and four outlet thermocouples were spaced evenly around the inlet and exit measurement points to provide a more accurate single-value temperature measurement.

Position	*# of Thermocouples*	*Gauge #*
Water inlet	4	30
Water outlet	4	30
Wall	8	40
Insulation	4	30
Ambient	2	30
Heater element	2	40

Table 8 Thermocouple distribution and gauges

The heater element temperature was monitored and served two purposes: the first was to ensure that the heater temperature did not rise excessively during testing, and the second was to use as a check for steady-state conditions by monitoring its convergence into a roughly constant value. Insulation thermocouples placed on the inside of the insulation and ambient thermocouples placed outside the insulation were used to monitor the heat loss from the test section.

2.3 Test section design

Three rectangular test sections of hydraulic diameters 1.05 mm, 0.85 mm and 0.57 mm were considered for the study (discussed in Section 2.3.1). The effect of various inlet conditions, as mentioned in the literature, is a known cause for result deviation. It was therefore proposed to experimentally determine the effects that inlet conditions have on the pressure drop and heat transfer coefficient in microchannel experimentation. Three inlet sections were therefore considered for the study: a sudden contraction inlet, a bellmouth inlet, and a swirl inlet (discussed in Section 2.3.2). These three inlets were designed as separate components from the test section, allowing them to be attached or removed from an already assembled test section when required. To ensure that the test section operated accurately with respect to the flow assumptions made for the conventional analytical theory (used in the prediction of friction factors and heat transfer coefficients), additional system interface components, such as a flow calmer, were used to reduce flow uncertainty and mimic the theoretical approach as best as possible.

Utilising three test sections with three inlets resulted in 21 test scenarios that were experimentally investigated, as given in Table 9. The design and construction details of the test sections, inlet conditions and system interface components are discussed in from Section 2.3.2 to Section 2.3.3.

The swirl inlet was limited to the 1.05 mm test section due to manufacturing constraints. Three experiments were conducted for each test section for different heat flux boundary conditions.

		Hydraulic diameter [mm]		
	Inlet condition	***1.05***	***0.85***	***0.57***
Number of tests	Sudden contraction	3	3	3
	Bellmouth	3	3	3
	Swirl	3	N/A	N/A

Table 9 Experimental test matrix

2.3.1 Microchannel design and construction

The microchannel test sections were manufactured from copper bars of cross-sectional dimensions 20 mm x 5 mm. Two such bars were used: one was used as the test section base (into which the channel was machined), and the other was used as the lid (into which the pressure ports were manufactured). The lid was kept common for the three test sections due to the manufacturing limitations on the pressure ports. The effective channel hydraulic diameters (D_h) were determined using equation (2).

$$D_h = \frac{4A_c}{P_w} \quad (2)$$

The channel dimensions and surface roughness are given in Table 10. The surface roughness of the microchannels in this investigation was measured using a laser scanning microscope. Three measurements were taken for each channel, one at each end and one at the middle. Using an area-averaged surface roughness measurement, an overall average surface roughness was determined for each microchannel. The lid surface roughness measured at 0.103 µm. This was due to the polished surface finish that was applied to the material. Two polytetrafluoroethylene (PTFE) layers were placed between the base and the lid to prevent water leakage (discussed later). This increased the total height of the microchannel by 50 µm.

Dimensions [mm]				*Measured Surface Roughness [µm]*				*Relative Roughness, ε, [-]*
Width	**Height**	**PTFE layer**	D_h	**Inlet**	**Middle**	**Outlet**	**Average**	
1.044	1.001		***1.05***	2.527	2.172	2.267	2.322	0.00232
0.833	0.810	0.05	***0.85***	2.625	3.177	2.071	2.624	0.00328
0.522	0.568		***0.57***	4.719	3.885	3.933	4.179	0.00836

Table 10 Microchannel geometric specifications

A square groove was milled lengthwise into the centre of the base material, creating a 200 mm long microchannel. Perpendicular grooves were milled 0.25 mm away from the microchannel inner wall of the channel (see Figure 4). Four of these grooves were milled on each side of the microchannel, each spaced 40 mm away from each other. The grooves were used to position and secure the wall thermocouples. Along the length of the material, 14 threaded holes were manufactured. These holes were used to secure the lid to the base using M2.5 x 0.5 hexagon screws.

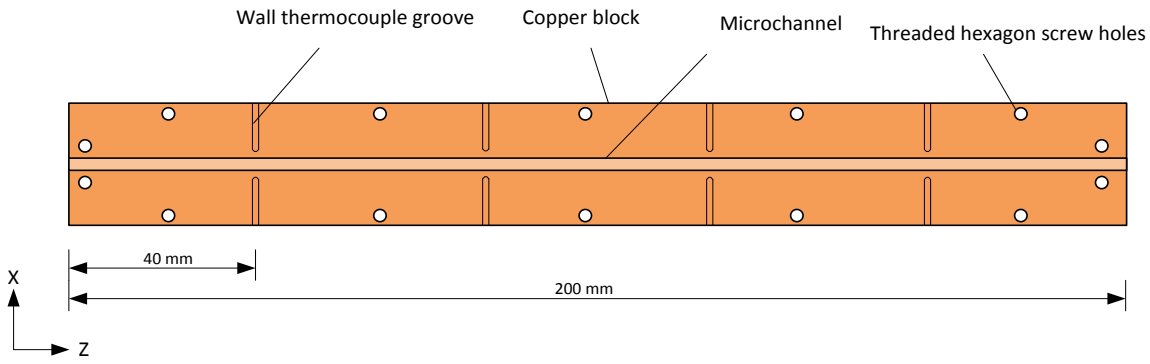

Figure 4 Microchannel base as seen from the top

The lid was reused for all the test sections, and had a thickness of 5 mm (as was the base). Unthreaded holes of diameter 2.6 mm were made on the lid for attachment to the test section base, as shown in Figure 5.

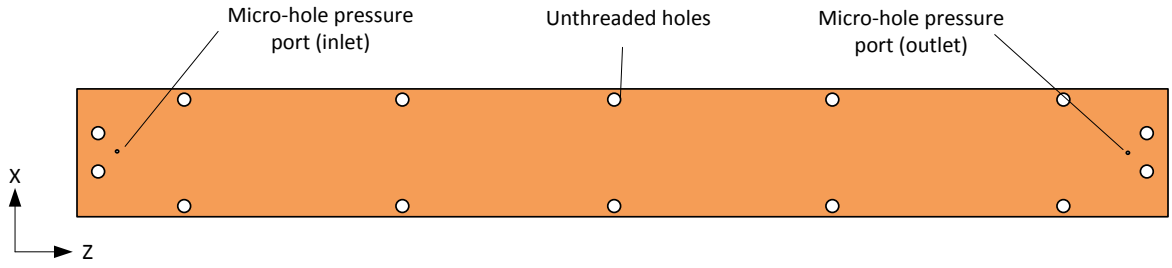

Figure 5 Microchannel lid as seen from below

Two circular cuts were milled into the top surface of the lid to a depth of 4.5 mm. These were placed at the widthwise centre of the lid, and located 5 mm away from the lengthwise edges. Micro-holes of diameter 0.1 mm were lasered through the remaining material thickness of 0.5 mm, as shown in Figure 6. The micro-holes, spaced 190 mm from each other, were used as the pressure ports to measure the differential pressure along the length of the microchannel.

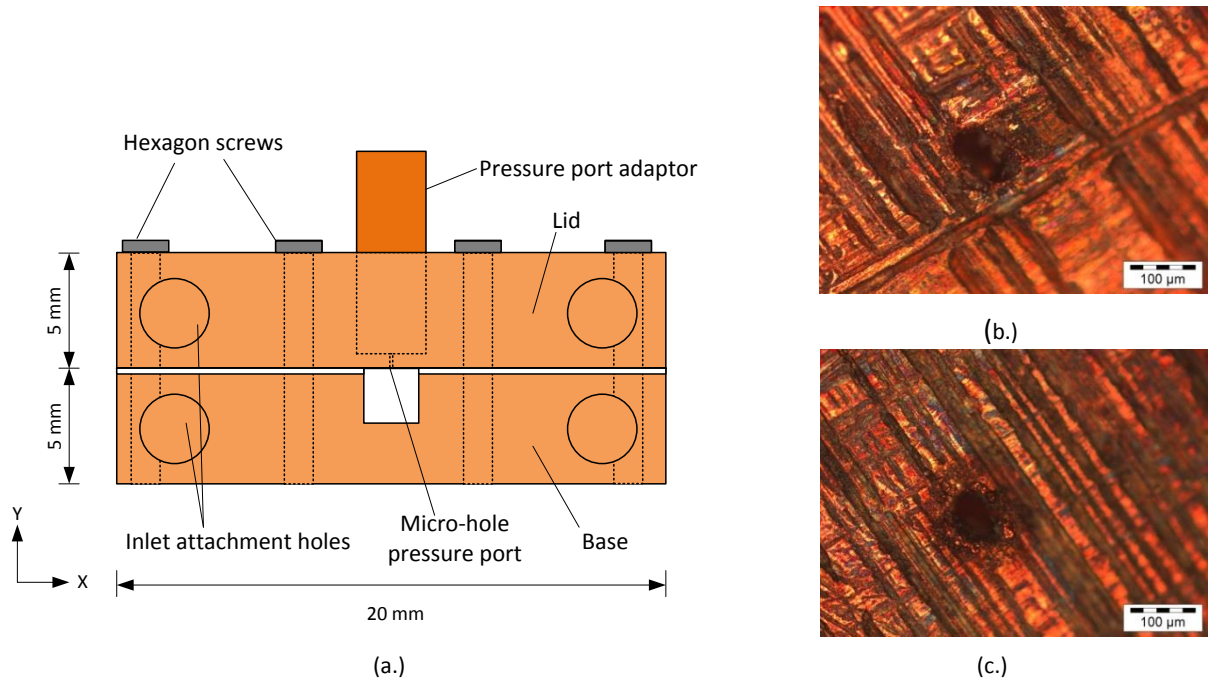

Figure 6 (a.) Pressure port position in test section (top left), (b.) Inlet pressure port (top right), (c.) Exit pressure port (bottom right)

Two layers of PTFE tape were used between the lid and the base to provide a seal at the interface. The two blocks were fastened to each other using 14 stainless steel hexagon screws. Four threaded holes were cut at both the inlet and the exit faces of the assembled test section to secure the inlet sections and connect the test section to the test facility (inlet attachment holes in Figure 6). The dimensions of the base and lid were selected to ensure that the attachment of the inlet conditions and the securement of the test section to the system were possible. The thickness in material influences the axial conduction and was determined prior to testing.

2.3.1.1 Axial heat conduction in the test sections

The axial heat conduction has been cause for much concern for heat transfer results in microchannels. Researchers have reported result deviation in the laminar regime, and have used the axial heat conduction equation, given by equation (1), to determine the region in which there is significant effect. As discussed in Section 1.3, the axial heat conduction plays a significant role when

the value of M is greater than 0.01 (the axial heat conduction constraint value). This has been established as the critical value used to determine if this conduction affects experimental results. The conduction effect was calculated for the three test sections, and the results are given in Figure 11.

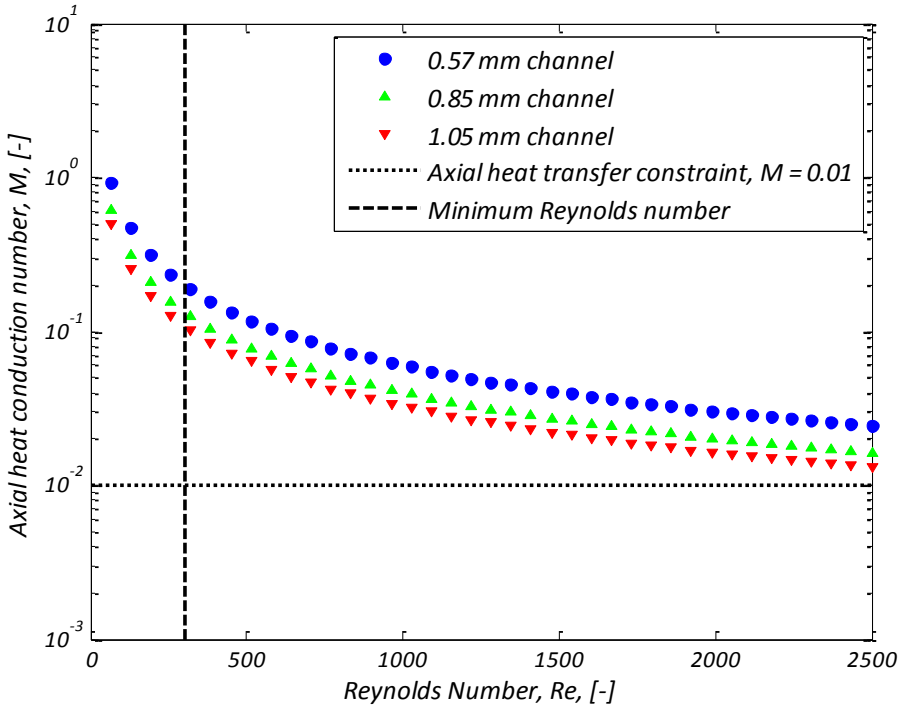

Figure 7 The effect of axial heat conduction on the three test section hydraulic diameters

The results of the calculation show the values of Reynolds number for the three test sections over the entire test range. The values above the axial heat conduction constraint are where the effect shows prominence for each test section. All the test sections were influenced by the axial heat conduction effect throughout the experimental Reynolds number range. The minimum operating Reynolds number criterion is the minimum value of experimentation as determined by the pump and mass flow meter specifications. Interpreting the graph results in the expectation that there will be a decrease in the Nusselt number throughout the laminar regime. The transition and turbulent regimes have more fluid mixing, and therefore the effect cannot be noticed in these regimes.

2.3.1.2 Thermal and hydrodynamic entrance lengths

Thermal and hydraulic entrance lengths yield different results compared with fully developed flow. Theoretical assumptions are usually made that flow is both thermally and hydrodynamically fully developed to allow for a less complicated analytical solution. In practice, the flow may not always be developed for both these cases. As cited in Céngel [46], equations (3) and (4) are used to check for the hydrodynamic and thermal entry lengths in the laminar regime respectively.

$$L_{hydro} = 0.05 D_h Re \quad (3)$$

$$L_{thermal} = 0.05 D_h RePr \quad (4)$$

Applying these equations to the 1.05 mm test section with a length of 200 mm yields the results plotted in Figure 8. The results show the entrance length for various Reynolds numbers for both the thermal and hydrodynamic entry length. Using this figure, it is evident that the flow is thermally developing at Reynolds numbers above 700. This illustrates beforehand that the Nusselt number will most probably not reflect the conventional values (Nusselt number is constant for fully developed flow through a rectangular tube), which are based on the assumption that the flow is thermally and hydrodynamically fully developed. Similar results were found for the other test sections.

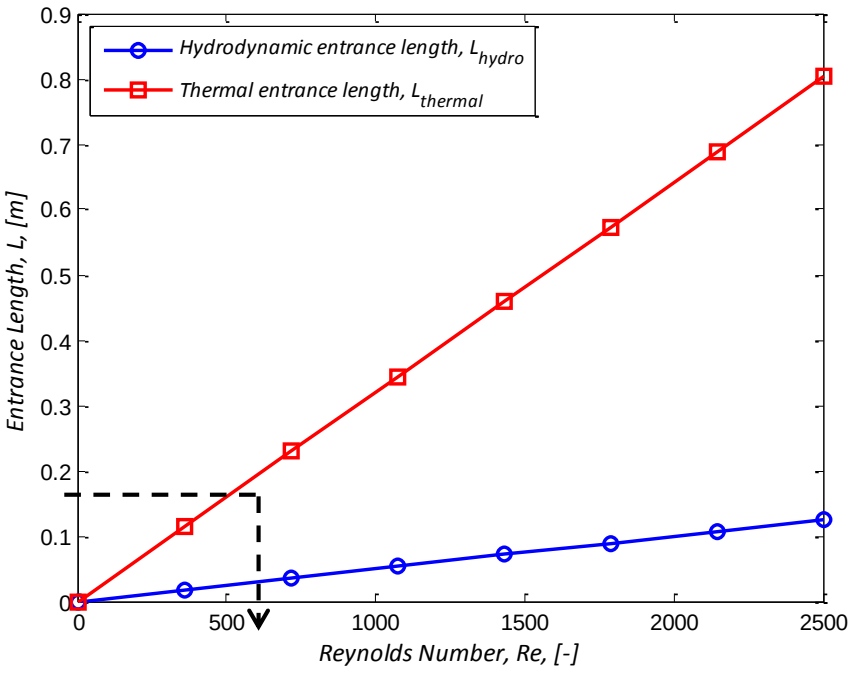

Figure 8 Thermal and hydrodynamic entrance lengths for the 1.05 mm microchannel at different Reynolds numbers

2.3.2 Inlet section design and construction

Inlet conditions, as discussed in the literature study, have been found to cause result deviation in microchannels. Generally, the assumption is made that flow enters a channel with a uniform velocity, and the velocity profile then develops as the fluid travels along the channel. In the literature, some authors such as Garimella and Singhal [9] designed their test sections such that water enters and exits the channel at a position perpendicular to that of the channel. Perpendicular entry of flow can cause uneven distribution of flow, altering the velocity profile in the test section. In some cases, multichannel systems were used, and the authors assumed that the flow rate in each channel was equal. Some researchers such as Kang *et al.* [28] used numerical methods to approximate the flow rate distribution in each channel of the array of channels.

In order to investigate the effect of the inlet conditions, the test section was designed to allow quick attachment and de-attachment of inlet sections with the least amount of disruption to an assembled test section. The test section, inlet and system interface components were placed on the same plane, removing the need for any sharp bends that could alter the flow distribution before entering the test section. For the purpose of illustrating the effects of the inlet conditions on microchannels, different types of inlet sections were used for the investigation.

The sudden contraction inlet was considered the base inlet as it was equivalent to most of the inlets found in the literature study. The bellmouth was to provide a more constant and equal flow distribution of water into the test section, ensuring that the analytical flow assumptions might be accurately met. The swirl inlet condition provided a controlled mixing effect to provide greater heat transfer in the microchannel.

2.3.2.1 Sudden contraction inlet condition

The sudden contraction inlet condition is a direct contraction from the system piping to the test section. This inlet was expected to yield results similar to those reported in the literature by Tam and Ghajar [39], and Olivier and Meyer [40]. The inlet was made of copper, and was connected to the test section inlet using four M2.5 x 0.5 hexagon screws.

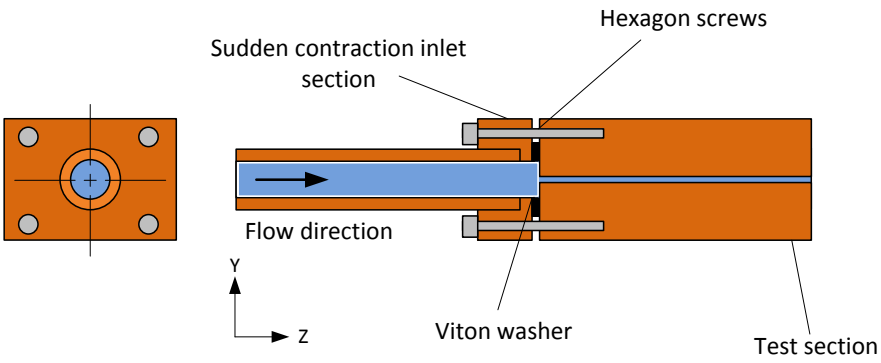

Figure 9 Sudden contraction inlet condition design

The sudden contraction sections provided a dual function – apart from being an inlet, it was also used as the system interface components at the inlets and the exits of the test sections. The exit component was attached similarly to the inlet - using four hexagon screws (see Figure 9). Located between the inlet and exit components, and the test section, were circular viton washers. These prevented leakage of water between the test section and the interface block, and acted as an insulation barrier to reduce heat from escaping to the system piping. The sudden contraction section also acted as the interface to connect the bellmouth inlet section. This allowed for a secure interface from the system piping to the bellmouth inlet without disruption.

2.3.2.2 Bellmouth inlet condition

The bellmouth inlet sections (one for each test section hydraulic diameter) provided a smooth profile for the water to follow to enter the microchannel from a circular to a square cross-section. The bellmouth shape theoretically induces a uniform velocity profile at the entrance of a channel, allowing the flow conditions to be similar to the analytical theory.

The bellmouth inlet was also used by Olivier and Meyer [40] in macrochannel flow. For their work, circular test sections were experimentally investigated. In comparison with this investigation, a bellmouth inlet condition is applied to contract a circular 6.35 mm (¼ inch) tube to a square channel equal to and smaller than 1.05 mm. As with the work of Olivier and Meyer, the inlet condition was designed using the method prescribed by Morel [41]. The system piping internal diameter stayed constant for each of the test sections, providing different contraction ratios for each channel. Table 11 gives the contraction ratio for each test section. The contraction ratio is defined as the ratio between the pre-contraction and post-contraction internal diameters.

D_h $[mm]$	*Contraction Ratio*
1.05	5
0.85	6.25
0.57	10

Table 11 Bellmouth inlet condition contraction ratios

Each bellmouth was manufactured in two halves from perspex using the same CNC machine that manufactured the microchannels. The base and lid were first aligned using a square aluminium alignment rod, and then bonded to each other using *Acrifix* perspex adhesive. Each inlet section was constructed using the same procedure with each having its own alignment tool. The tools were manufactured approximately 30 µm smaller than the microchannel. This provided a clearance fit between the rod and the microchannel walls, resulting in a maximum misalignment of 30 µm between the inlet section and the test section.

The inlet sections were attached to the channel using four M2.5x0.5 hexagon screws (see Figure 10). Between the bellmouth and the test section, layers of PTFE tape were stacked around the periphery of the contraction exit to provide a seal at the interface between the inlet and the test section.

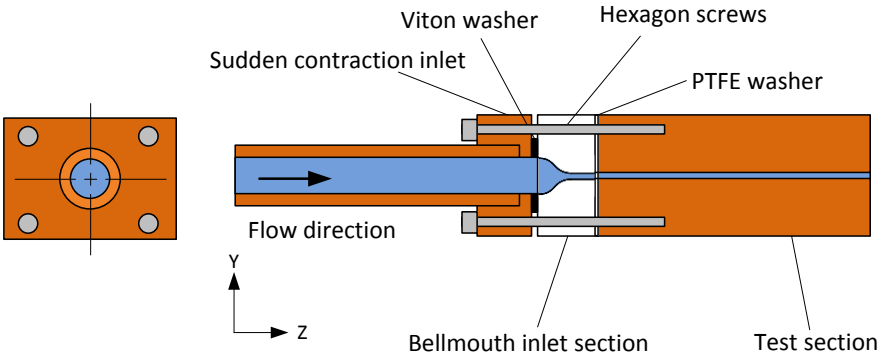

Figure 10 Bellmouth inlet condition design

The inlet was first aligned to the channel using the alignment tool (the same used with the assembly of the inlet sections) and the sudden contraction inlet block was placed in front of the bellmouth section. A viton washer was placed between the two components to prevent water leakage and reduce heat distribution to the system. The structure was then secured using four hexagon screws. The alignment tool was removed once the inlet was secured between the inlet block and the bellmouth section.

2.3.2.3 Swirl inlet condition

With the swirl inlet, it was attempted to increase the heat transfer coefficient by causing the fluid to spiral as it flowed through the microchannel. To create a swirl in the flow, two off-centre in-plane holes were made in a copper microchannel inlet section. The holes were located at the bottom and top walls on opposite edges close to the wall. This caused the water to flow around the periphery of the microchannel, creating a swirl flow (see Figure 11). The design of the swirl inlet was based on the work of Aydin and Baki [42], who used a similar design on a macrochannel test section. The design was verified using a computational fluid dynamics model before it was manufactured. Numerical results indicated that significant swirl is present, but that it dissipates along the length of the channel.

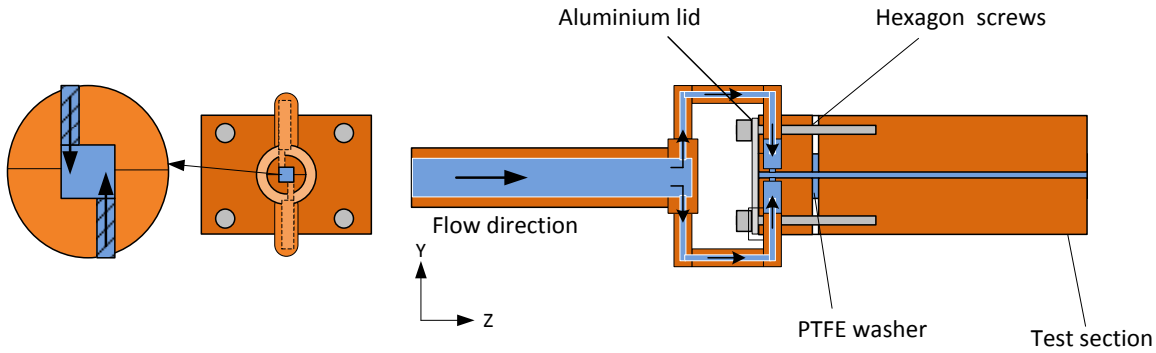

Figure 11 Swirl inlet condition design

The swirl inlet section was only tested with the 1.05 mm microchannel due to manufacturing limitations, and was manufactured from copper. It consisted of a base and a lid, each with a 0.5 mm deep, 1 mm wide channel milled into the block. On the outer surface of the blocks, two 3.5 mm diameter holes were drilled 0.1 mm away from the channel and were threaded to allow the attachment of the connector block. A 0.4 mm hole was drilled from the microchannel to the bottom of the channel. This was done on the base and lid of the inlet condition, with the holes placed on opposite ends to each other. The lid and the base were soldered together using tin-lead solder, and 3 mm diameter holes were drilled through the front face as attachment holes – similar to those made for the bellmouth inlet. A threaded copper adaptor was made to connect the inlet to the system piping.

The inlet was aligned using the aluminium alignment tool (as was used with the bellmouth inlet section assembly) and layers of PTFE tape were placed on the face of the inlet condition to prevent water leakage between the inlet section and the test section. Once positioned and aligned, two hexagon screws were tightened to secure the inlet. The alignment tool was then removed, and the

remaining two screws were placed. These two screws held in place an aluminium lid to cover the open end of the inlet. PTFE tape was placed over the aluminium cover to act as a sealant.

2.3.3 System interface components

Figure 12 indicates how the test section was interfaced with the system, shown here with a bellmouth inlet section. Unlike the other inlets, the swirl inlet was attached to the system directly using its specially made copper adaptor.

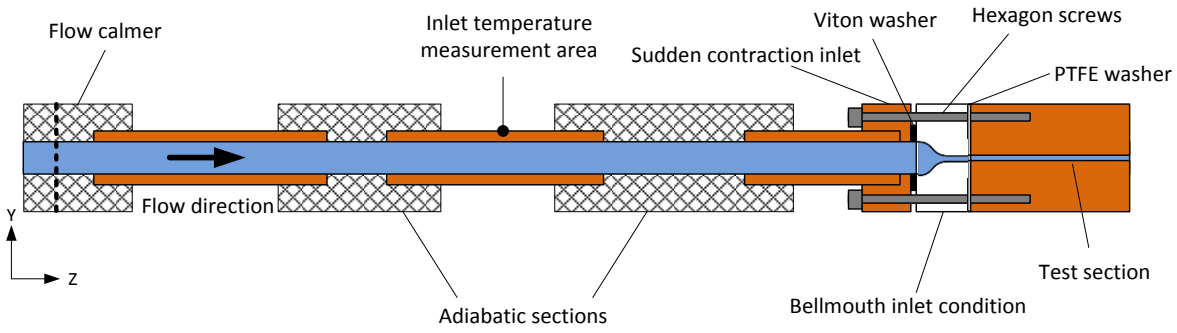

Figure 12 System interface components at the inlet

Before the water entered the inlet section, the inlet temperature measurements were made. To prevent any upstream heat conduction from the heater element affecting the temperature measurement (axial heat conduction), the measurement area was isolated from the system piping using two perspex tubes (adiabatic sections). The inlet temperature measurement was made using four thermocouples placed on the surface of the copper tube located between the adiabatic sections.

A calming section was placed before the inlet temperature measurement area to reduce flow inconsistencies. Two flow calmers were manufactured, one from perspex and the second from copper. The copper calming section was manufactured after the perspex calming section failed due to the high system pressure over prolonged operation time periods. The perspex flow calmer consisted of 18 0.4 mm holes while the copper flow calmer consisted of 15 0.6 mm holes. The holes were drilled radially in the material, providing a honeycomb-like effect, calming the flow before entering the test section (see Figure 13).

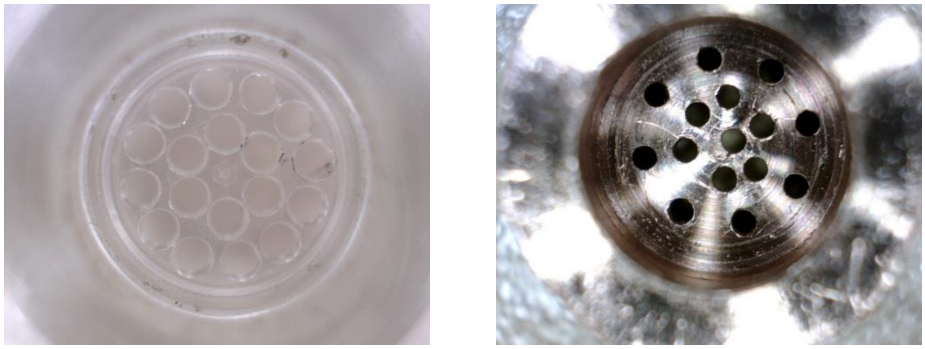

Figure 13 Calming sections to reduce flow inconsistencies, perspex calmer (left) and copper calmer (right)

Figure 14 shows how the test section was interfaced with the system at the exit of the test section. The exit temperature was measured similarly to the inlet temperature – using a copper measurement area bounded by perspex insulation sections. A flow mixer was placed in the pipe at the exit of the test section and before the temperature measurement area. This reduced temperature gradients that could exist in the heated water and resulted in a condition where the copper section assumed the water bulk outlet temperature.

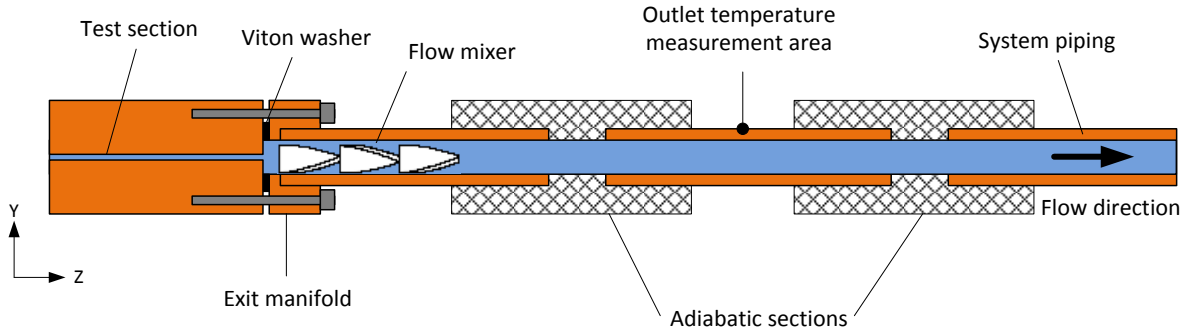

Figure 14 System interface components at the outlet

The flow mixer was made from three copper rectangular sheets measuring 1 mm x 5 mm x 10 mm. Each sheet was bent to form a twist so that the rear end was perpendicular to the front end. The first and last sheets were bent in a clockwise direction, while the middle sheet was bent anti-clockwise (see Figure 15). The sheets were then bonded together using tin-lead solder. The flow mixer was placed in the system piping before the attachment of the adiabatic section.

Figure 15 Flow mixer used at the exit of the microchannel to allow for more accurate temperature measurements

2.3.4 Microchannel test section assembly

The test sections were assembled by initially attaching the wall thermocouples, then placing the PTFE tape layers over the top surface of the base without overlapping into the channel. The wall thermocouple tips were measured to be at a maximum distance of 0.4 mm from the channel wall. The wall slots were designed to hold the thermocouple tips at the midpoint of the wall.

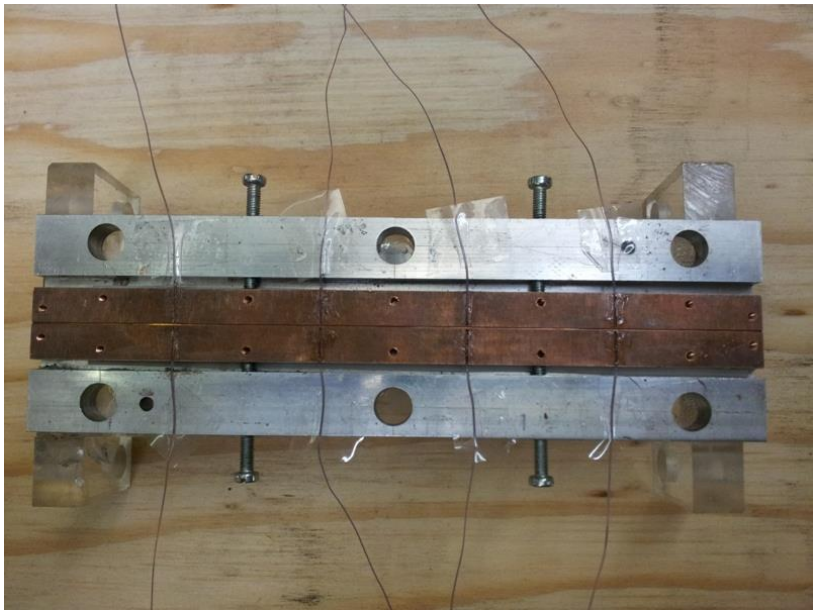

Figure 16 Attachment of thermocouples to the base of the test section

The wall thermocouples were attached to the microchannel base, as shown in Figure 16. The wall thermocouples were then secured using adhesive, preventing any loosening of the thermocouple while completely sealing the channel slot. Once cured, any excess protruding adhesive was removed using fine sandpaper. Thereafter, PTFE tape was carefully placed on top of the base of the test section. Care was taken to prevent the tape from overlapping into the channel. Once the first layer was positioned, the second layer was applied in a similar fashion, as shown in Figure 17 (a.) and (b.).

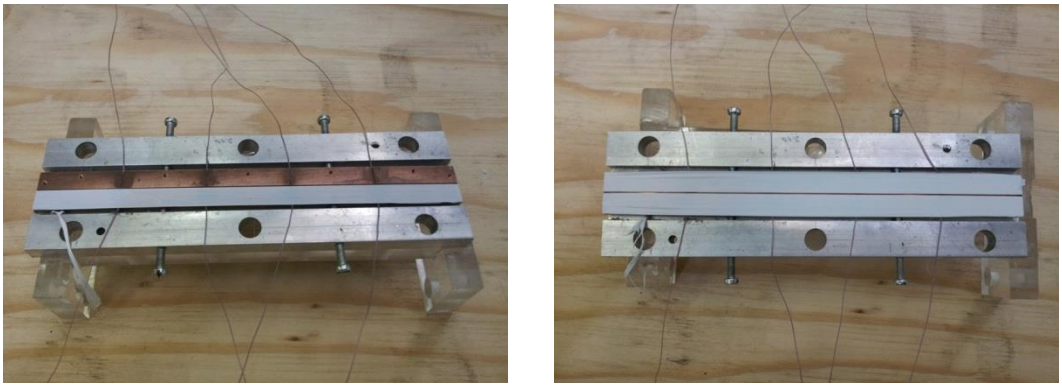

(a.) *(b.)*

Figure 17 Placement of PTFE tape above the base, (a.) First layer (left), (b.) Completion (right)

With the PTFE layers in place, slits were made in the tape located over the threaded holes' positions to prevent the hexagon screws from displacing the tape during the lid tightening procedure. The tightening process was done in sequence, and the tightening sequence was consistent for all three test sections. Figure 18 shows a complete test section with the lid attached to the base.

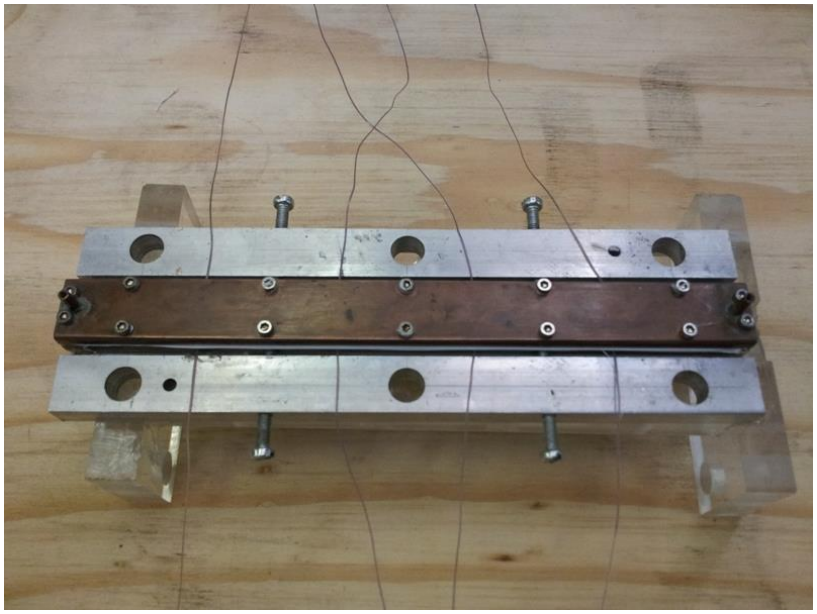

Figure 18 Securing of lid to the base by means of hexagon screws

An inlet section was attached to the test section after assembly using four M2.5 x 0.5 mm hexagon screws. The inlet and exit manifold blocks were attached thereafter, where the flow mixer was placed within the exit manifold (as shown in Figure 19).

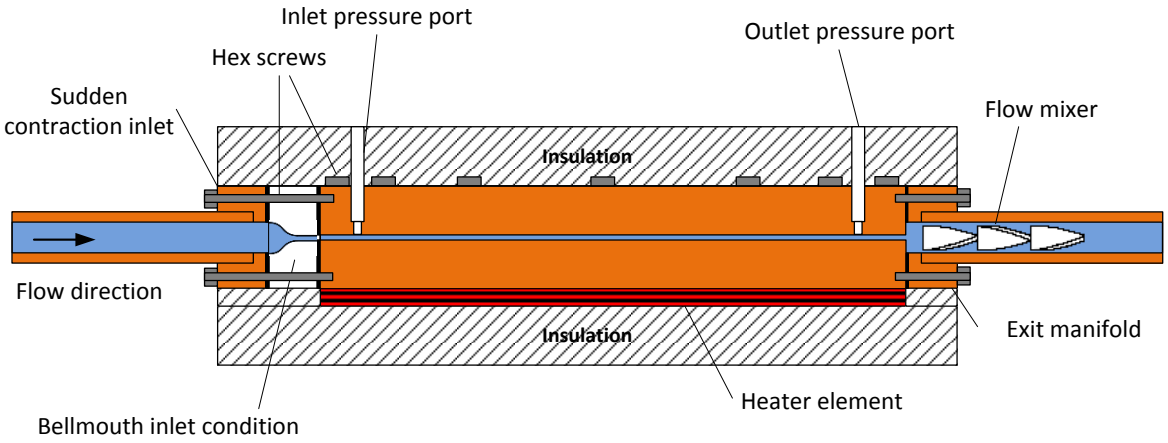

Figure 19 Assembly diagram of a test section

The test system piping was attached to the inlet using a compression fitting, while the exit of the test section was attached to the system piping using 6.35 mm (¼ inch) copper piping. The test section was insulated using 200 mm thick *ISOboard* polystyrene insulation having a manufacturer specified thermal conductivity of 0.03 W/m^{2}K. Insulation of equal thickness was placed around the entire test section and system interface components.

Figure 20 shows a test section fully assembled and ready for experimentation. Once all the hexagon screws linking the test section to the system were tightened, the test section was attached to the system to commence with initial pressure testing. Pressure testing ensured that the in-channel pressure ports were not blocked and that there were no leaks at any connection interfaces. The test section was placed in a polystyrene insulation base, and a polystyrene lid was placed over to provide insulation around the entire test area.

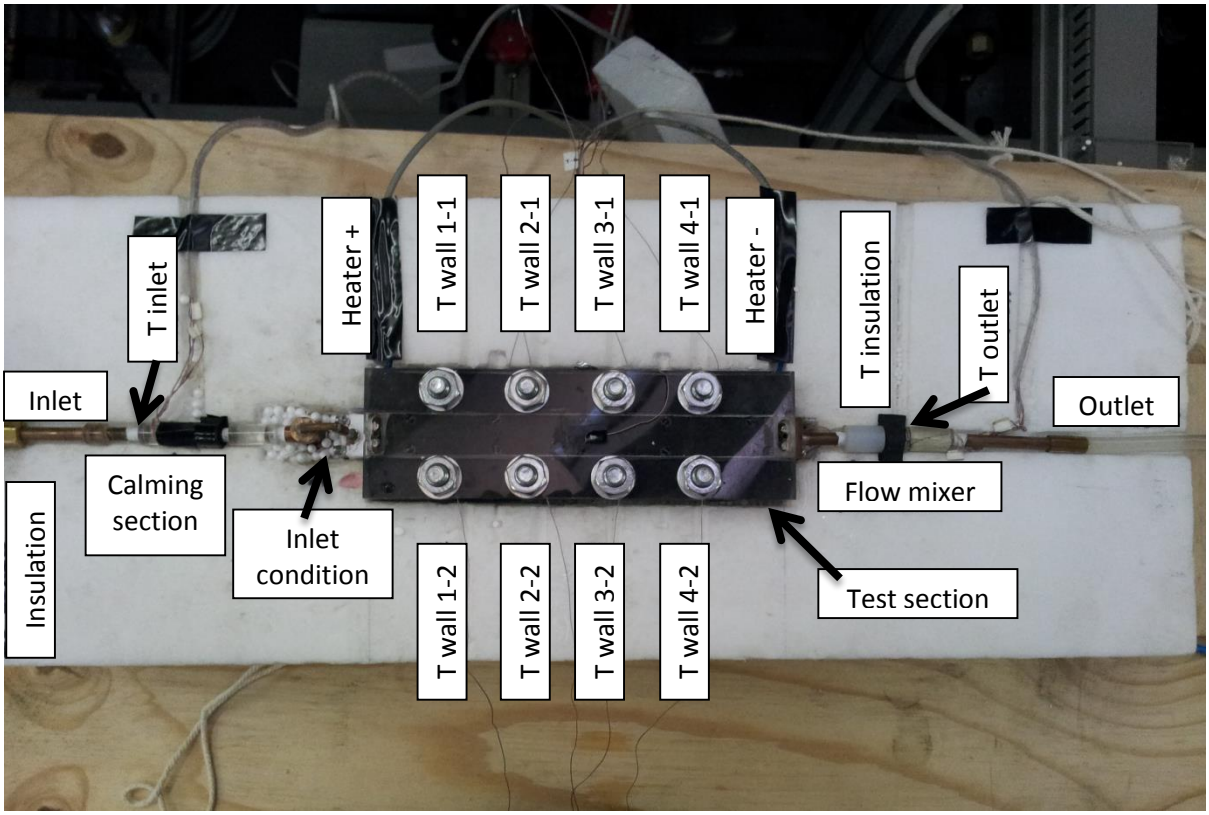

Figure 20 Complete test section ready for experimentation

2.4 Summary

A test facility for experimentally determining the heat transfer and pressure drop in microchannels was designed and constructed using equipment that meet the requirements of the low flow rates and small dimensional characteristics of microchannels. Three test sections were fabricated from copper along with three inlet sections to determine the effects of inlet conditions on microchannels. The inlets were designed as separate components to provide easy attachment and removal from a test section without disrupting the assembly of the test section. Wall temperatures were measured along with inlet and outlet temperatures to accurately determine Nusselt numbers. A calming section was placed before the test section to reduce flow instabilities before the water entered into the test section. A flow mixer was placed after the test section to provide adequate mixing of the outlet water, thereby allowing a more accurate outlet fluid temperature measurement. The test section and interfaced components were insulated to reduce ambient heat loss during experimentation.

3 Experimental procedure, calibration and data reduction

3.1 Introduction

Data reduction was required to be done on the logged results to determine the friction factors, Nusselt numbers and Colburn *j*-factors. Determining these results required accurate interpretation of the test section measurements. For some measurements such as the temperatures and differential pressures, calibration was required to accurately determine the measurement values.

Along with measurements and their respective calibration values, there is an associated uncertainty value, which determines the accuracy of the measurement. The uncertainty of each instrument was considered when doing the data analysis, and prescribed methods (which are discussed in this chapter) were employed to analyse these uncertainties and apply them to the final results.

Consistent logging and data interpretation procedures were used during experimentation for each test case scenario to ensure consistency among results. This chapter discusses the procedures involved in logging the measurements, calibrating the equipment and analysing the results.

3.2 Experimental procedure

The experimental procedure began with all the equipment switched off. Once the test facility valves were correctly adjusted to allow the water to flow through the test section, the electronic equipment was switched on. The pump was initially set to a high flow rate to provide a high pressure at the microchannel pressure ports. This allowed for any encapsulated air to escape the pressure transducer via the bleed ports located in the pressure transducer. Once there was no sign of any air escaping, the bleed ports were closed and the pressure was left to stabilise. In order to ensure that the pressure transducer was measuring the correct zero value, a check was done by closing the valves connecting the test section to the test facility and opening the bypass valve (refer to the test facility schematic diagram, Figure 3). The pressure in the test section was left to stabilise within the test section and was monitored on the Labview software interface. Once the pressure stabilised, a zero-correction value was logged. This procedure was done for all test scenarios prior to testing. The test section's valves were reopened thereafter and the bypass valve was closed in preparation for testing.

Testing began at a high flow rate, and was incrementally decreased to the minimum flow rate equivalent to a Reynolds number of approximately 300. Experimenting from a low flow rate to a high flow rate would have resulted in an increased system temperature as the thermal gradient between the hot water and the test section material would be low. This low gradient would cause the test section and the surrounding insulation to store more heat before being lost to the environment. By increasing the flow rate thereafter, this stored heat would be absorbed back into the flowing water in the test section. This would result in a higher heat output measurement (by raising the measured outlet temperature), resulting in wrong results. It was therefore decided to test from an initial high flow rate and decrement to the lowest flow rate, ensuring that there was no re-absorption of heat.

Achievement of steady state was evaluated by calculating the energy balance of the system using equation (5). The energy balance expresses the ratio of the heat lost with respect to the average heat transferred to the system. Once the power supply output was set for a specific experiment, the energy balance was monitored. The steady-state criterion was reached when there was a long time period of stability in the value of the energy balance equation. On average, the energy balance was recorded at 4% over all the test scenarios, with a minimum value of 0.5% found in the transition regime, and a maximum value of 15% found in the laminar regime.

$$eb = \frac{\bar{\dot{Q}}_{in} - \bar{\dot{Q}}_{out}}{\bar{\dot{Q}}_{in}} \qquad (5)$$

To provide further confirmation of steady state, the wall temperature, bulk fluid temperature and heater element temperature were monitored. At steady-state conditions, these values remained fairly constant with low fluctuations of 0.04 °C observed. This value was determined to hold true for all experiments after much experimental iteration.

The flow rate decrement was set for a Reynolds number step size of between 80 and 100. This allowed for the capturing of the differential pressures and temperatures with good resolution to obtain results in all three flow regimes. Once the final value of flow rate was set, which resulted in a Reynolds number of approximately 300, the power supply was switched off and the test section was allowed to cool by setting the pump to provide a high flow rate. The pump was switched off once the test section temperatures measured approximately 25°C. When all the electronic equipment was switched off, the test facility valves were closed, and the system was returned to the original off-condition.

3.3 Logging of measurement data

During experimentation, measurements were logged using the *National Instruments* data acquisition hardware and software. A Labview graphical user interface was designed to monitor and control the system. The interface was able to control the pump and power supply, while monitoring the differential pressure, mass flow rate, temperature measurements and the energy balance. The measurements were logged into individual files and were analysed after an experiment was completed. Each data file consisted of 100 measuring points. Data logging took place at a frequency of 10 Hz. Each file consisted of the following measurements:

- Date and time
- Mass flow rate*
- Differential pressure*
- Differential pressure zero value
- Inlet, outlet and wall temperatures*
- Insulation, ambient and heater element temperatures*
- Power supply output voltage and current values*
- Test section output power
- Energy balance

The test section power output and energy balance were included in the file to allow quick access to information from the file directly without any post-data analysis. Calibration coefficients were applied to the uncalibrated measurements during data analysis process.

3.4 Equipment calibration and uncertainty

Instruments were either purchased pre-calibrated or required calibration. Calibration of certain equipment, such as thermocouples, resulted in more accurate representation of measurements and a reduced uncertainty value than the standard manufacturer's uncertainty specification. Calibration was applied on the thermocouples and pressure transducer. The mass flow meter was pre-calibrated, and the uncertainty was given by the manufacturer.

* Uncalibrated values

3.4.1 Mass flow meter calibration

The Coriolis mass flow meter was purchased pre-calibrated, and had a manufacturer-specified standard uncertainty of 0.05% of the measurement for flow rates above 5% of the full-scale value (1.36 kg/min). For flow rates below 5% of the full-scale value, the uncertainty was calculated using equation (D.8) in Appendix D.

3.4.2 Thermocouple calibration

The thermocouples were calibrated against a PT100 thermocouple probe. The PT100 had a manufacturer-specified maximum uncertainty of 0.04°C (which was included in the uncertainty analysis). The thermocouples were calibrated using a cooling-down process from a temperature of approximately 70°C to a temperature ranging between 20°C and 30°C. Increments of 2°C were logged between the upper and lower limits. The uncertainties of the thermocouples were determined using the method prescribed by Kline and McClintock [43]. Of the thermocouples used, 98% were determined to have an uncertainty below 0.1°C. A value of 0.1°C was adopted for all the thermocouple uncertainties as a more cautious approach. The calibration coefficients were calculated using linear regression techniques. This resulted in each thermocouple calibration consisting of two coefficients, a gradient and a constant. Further information on thermocouple calibration can be found in Appendix B.

3.4.3 Pressure transducer calibration

The pressure transducer used for the experimentation allowed for interchange diaphragms. Two diaphragms were used and each was calibrated using a different method due to their full-scale value. The first diaphragm measured a maximum differential pressure of 22 kPa. This diaphragm was calibrated against a 2 bar digital differential pressure meter using a 3 m high water column. Ten different water levels were used to get incremental values to determine an accurate calibration curve. The pressure transducer and digital meter were placed in parallel, providing equal pressure to both the transducer and the meter.

The second diaphragm had a maximum full-scale value of 220 kPa. This diaphragm was calibrated using a dead-weight system against a 7 bar digital differential pressure meter. The dead-weight system involved pumping a piston to a specific pressure and logging the measured pressure and the digital meter reading. Using linear regression techniques, calibration curves were determined for both pressure transducers. Details of the procedure and calibration to calculate the overall uncertainty are given in Appendix C.

3.4.4 Measurement equipment uncertainties

The thermocouple, mass flow meter and pressure transducer uncertainties were calculated and are presented in Table 12. The absolute and relative uncertainties are given for each test section over the operating range. These values, along with the uncertainties of the fluid properties play a major role in determining the uncertainties of the Reynolds numbers, friction factors, Nusselt numbers and Colburn *j*-factors.

Equipment		***Uncertainty***	***Operating Range***	***Uncertainty Range***
Thermocouples		0.1°C	20 – 57 °C	0.18% - 0.50%
Pressure Transducer	***#34***	57.6 Pa	700 – 20 000 Pa	0.29% - 8.23%
	#44	435.6 Pa	1000 – 160 000 Pa	0.27% - 43.6%
Mass Flow Meter		0.000027 kg/s	0.00013- 0.0027 kg/s	0.1% - 52%
Hydraulic Diameter		0.01 mm	-	0.95% - 1.75%
Length		0.2 mm	-	0.10%

Table 12 Uncertainties related to the experimental measurement equipment for the different test sections

3.5 Data reduction

The friction factor, average Nusselt number and Colburn *j*-factor had to be calculated using the experimental data. Each data file consisted of 100 measurement points, which were averaged to form a single value. The calibration factors were applied to the applicable values, and the data was ready to be analysed.

Once the pressure transducer calibration coefficients were applied, the zero-pressure correction value was factored in. Average inlet and outlet temperatures were calculated, and the average bulk fluid temperature was determined thereafter. Water properties were determined using the equations proposed by Popiel and Wojtkowiak [44] at the bulk-fluid temperature. More detail of this can be found in Appendix A. The average wall temperature was calculated using the trapezoidal rule due to most of the experimentation being under the influence of a thermally developing flow. The trapezoidal rule provided a more accurate average wall temperature calculation. Using the calculated temperatures, calibrated differential pressures and mass flow rates, as well as the water properties, the data reduction proceeded.

The Reynolds number were calculated using equation (6) at the bulk-fluid temperature.

$$Re = \frac{\rho v D_h}{\mu} \qquad (6)$$

3.5.1 Friction factor data reduction

The measured friction factor was calculated using equation (7) from the measured differential pressure (ΔP), the pressure port length (L_p), microchannel hydraulic diameter (D_h), fluid properties and the average fluid velocity (v). The average fluid velocity was obtained from the measured mass flow rate and cross-sectional area of the microchannel.

$$f = \Delta P \frac{D_h}{L_p} \frac{2}{\rho v^2} \qquad (7)$$

Rectangular-shaped channels require different methods to predict the friction factor. The Shah and London correlation of 1978 [45] is one such equation that is used for the prediction of friction

factors in the laminar regime. The correlation is well documented in literature for the prediction of rectangular macrochannels and microchannels, and is given by equation (8).

$$C_{sl} = f_{sl}.Re = 96(1 - 1.3553\alpha + 1.946\alpha^2 - 1.7012\alpha^3 + 0.9564\alpha^4 - 0.2537\alpha^5) \quad (8)$$

The Shah and London correlation is based on the channel aspect ratio, defined by equation (9).

$$\alpha = \frac{\max(W,H)}{\min(W,H)} \quad (9)$$

The turbulent regime friction factor was compared with the Blasius equation, given by equation (10).

$$f_{blasius} = 0.3164/Re^{\frac{1}{4}} \quad (10)$$

Experimentally obtained friction factors were compared with these of the Shah and London and the Blasius equations later in this report.

3.5.2 Heat transfer data reduction

The test section was designed to transfer heat from the heater element to the water flowing through the channel. Different constant surface heat conditions were applied to the test section, and the average power input was calculated using equation (11).

$$\bar{\dot{Q}}_{in} = \bar{V}\bar{I} \quad (11)$$

The average power input is defined as the averaged supplied voltage ($\bar{V}$) multiplied by the averaged supplied current ($\bar{I}$) of the power supply. Each test case had three heat flux values applied by the power supply. The heat fluxes for each test section were determined by calculating an equivalent average surface heat flux, given by equation (12).

$$\bar{\dot{q}} = \frac{\bar{\dot{Q}}_{in}}{A_{s,m}} \quad (12)$$

The average surface area was based on the area where the heater element makes contact with the channel material (microchannel base bottom surface area), given by equation (13).

$$A_{s,m} = W_m L \quad (13)$$

This resulted in the approximately equal heat flux values with respect to the microchannel surface area for all three test cases and the values of the power input and heat fluxes for each test section are given in Table 13.

D_h $[mm]$	*Heat input [W] or heat flux* $[W/m^2]$		
1.05	20	30	40
	(5 000)	(7 500)	(10 000)
0.85	16	24	32
	(4000)	(6 000)	(8 000)
0.57	10	15	20
	(2 500)	(3 750)	(5 000)

Table 13 Power and heat flux input matrix for each test section. The heat input values are without brackets and the heat flux values are in brackets.

The average heat transferred to the water was calculated using equation (14).

$$\bar{\dot{Q}}_{out} = \dot{m} C_p (\bar{T}_{out} - \bar{T}_{in}) \quad (14)$$

The average wall temperature and bulk fluid temperature measurements were used to calculate the average heat transfer coefficient, given by equation (15).

$$\bar{h} = \frac{\bar{\dot{Q}}_{out}}{A_s (\bar{T}_w - \bar{T}_b)} \quad (15)$$

The surface area of the heat transfer coefficient is based on the microchannel wall surface area, given by equation (16).

$$A_s = 2(W + H)L \quad (16)$$

The mean bulk temperature was determined using equation (17).

$$\bar{T}_b = \frac{1}{2}(\bar{T}_{in} + \bar{T}_{out}) \quad (17)$$

Using the average heat transfer coefficient, the hydraulic diameter and the fluid thermal conductivity (k_f) at the bulk-fluid temperature, the average Nusselt number was calculated by using equation (18).

$$\overline{Nu} = \frac{\bar{h}D_h}{k_f} \quad (18)$$

For comparative purposes, the Nusselt number was also calculated using conventional equations generally used for larger scaled channels. In the laminar regime, a constant Nusselt number value of 3.61 for square channels with fully developed flow was used. The turbulent Nusselt number was compared to the Gnielinski equation of 1976, given by equation (19) and found in Céngel [46].

$$\overline{Nu}_{Gnielinski} = \frac{(f/8)(Re - 1\,000)Pr}{1 + 12.7(\sqrt{f/8})^{\frac{1}{2}}\left(Pr^{\frac{2}{3}} - 1\right)} \quad (19)$$

3.5.3 Colburn *j*-factor

The Colburn *j*-factor (20) expresses the Nusselt number while taking into account the effect of the fluid Prandtl number variation.

$$j = \frac{\overline{Nu}}{RePr^{\frac{1}{3}}} \quad (20)$$

A comparison between the friction factor and the *j*-factor can be made due to similarities in the profile shape. Its application to this study is discussed in Chapter 5.4.

3.6 Uncertainty analysis of data reduction

The uncertainty analysis was done for the Reynolds number, friction factor, Nusselt number and Colburn *j*-factor to determine the bounds in which the results lay. The methods proposed by Moffat [47] and Kline and McClintock [43] were used to determine the uncertainties of the above-mentioned equations, and the derivation of the uncertainties is given in Appendix D. Table 14 gives the uncertainties for the equations used in the data analysis.

Hydraulic diameter	*Result*	*Result Range [-]*	*Uncertainty Range [±]*	*Average Uncertainty [±]*
1.05 mm	*Reynolds number*	365 - 2 620	2.32% - 26.1%	6.14%
	Friction factor	0.028 - 0.14	2.16% - 27.4%	4.24%
	Nusselt number	3 - 16.3	4.98% - 26.4%	7.55%
	Colburn j-factor	0.0018 - 0.0051	5.71% - 37.2%	8.97%
0.85 mm	*Reynolds number*	371 - 3 000	2.47% - 30.1%	7.06%
	Friction factor	0.029 - 0.094	2.82% - 50.7%	9.99%
	Nusselt number	4.35 - 31.71	6.48% - 30.5%	12.9%
	Colburn j-factor	0.0017 - 0.0049	7.11% - 42.9%	15.4%
0.57 mm	*Reynolds number*	357 - 2 833	2.95% - 45.4%	11.5%
	Friction factor	0.038 - 0.13	3.98% - 46.3%	12.1%
	Nusselt number	2.53 - 29.84	12.6% - 45.6%	19.1%
	Colburn j-factor	0.0021 - 0.0039	15.3% - 64.4%	23.1%

Table 14 Range of results and uncertainties for the Reynolds number, friction factor, Nusselt number and Colburn *j*-factor for the three test sections

3.7 Summary

The experimental procedure used for logging the data for each test section was discussed. The energy balance was used to determine when steady-state conditions were reached. A single data file consisting of 100 points for each measurement was averaged to determine a single result for the friction factors, Nusselt numbers and Colburn *j*-factors. Each set of experiments consisted of approximately 25 points to capture the laminar and transition regimes. Three heat fluxes were used for each test section for each inlet section. Using conventional theory applicable to macro-scale systems, the data was analysed and the results were determined. Water properties were analytically calculated using the mean bulk fluid temperature. The associated uncertainties of the results were calculated to determine the accuracy of the measurements.

4 Results: Friction factor and Nusselt number

4.1 Introduction

The results for the friction factor and Nusselt number for various inlet conditions are the main outcomes of the study. The experimental work was first performed with adiabatic testing with the 1.05 mm and the 0.57 mm test sections for verification purposes to provide insight into the expected behaviour of the test section during final testing. Thereafter, diabatic experiments were performed with the three test sections and their respective inlet conditions for the three considered heat fluxes.

4.2 Adiabatic results

The friction factor for the 1.05 mm channel with sudden contraction inlet test section was captured and is presented in Figure 21. The laminar results were compared with the Shah and London [45] correlation for square channels while the late transition regime results were compared with the Blasius equation [46]. The laminar regime results show very good agreement with the conventional theory, resulting in a maximum deviation of 5% throughout the entire range. Transition results were overpredicted by the Blasius equation by up to 14%. The transition regime commenced at a Reynolds number of approximately 1 800 and ended at a Reynolds number of approximately 2 300.

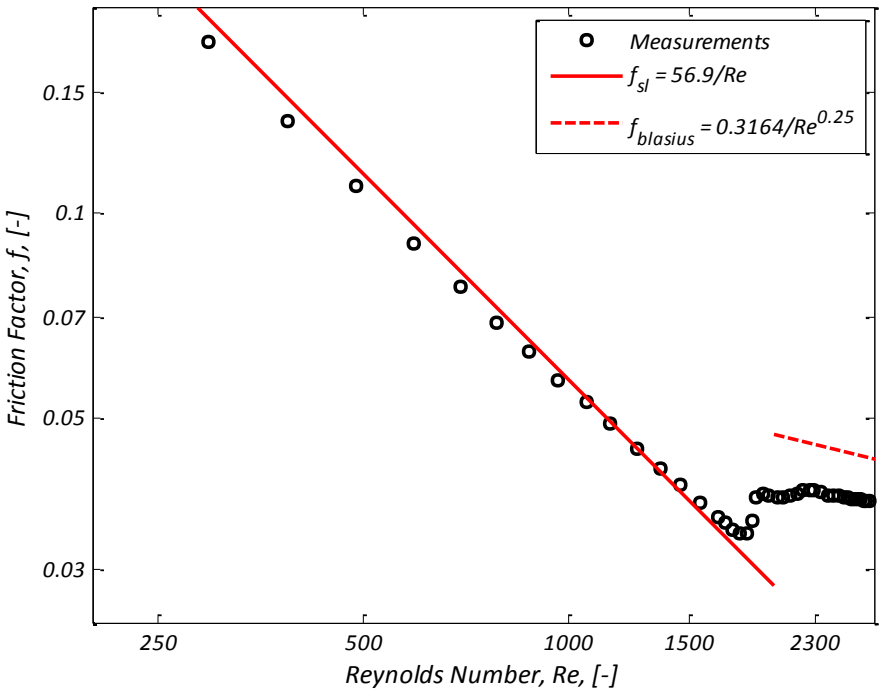

Figure 21 Adiabatic results for the 1.05 mm test section with a sudden contraction inlet

The result of the 1.05 mm bellmouth inlet adiabatic test is presented in Figure 22. A smaller Reynolds number increment to that of the sudden contraction inlet experiment was used to capture the effect of the bellmouth over the transition regime. The results show good agreement with the London and Shah correlation [45] in the laminar regime up to a Reynolds number of approximately 1 100. At this point (Point A), the friction factor spikes and continues parallel to the Shah and London correlation up to a Reynolds number of approximately 1 500. The transition regime commences thereafter until a Reynolds number of approximately 2 150.

The laminar regime results show deviation from the Shah and London correlation within 5%. The transition regime results are overpredicted by the Blasius equation by approximately 10%.

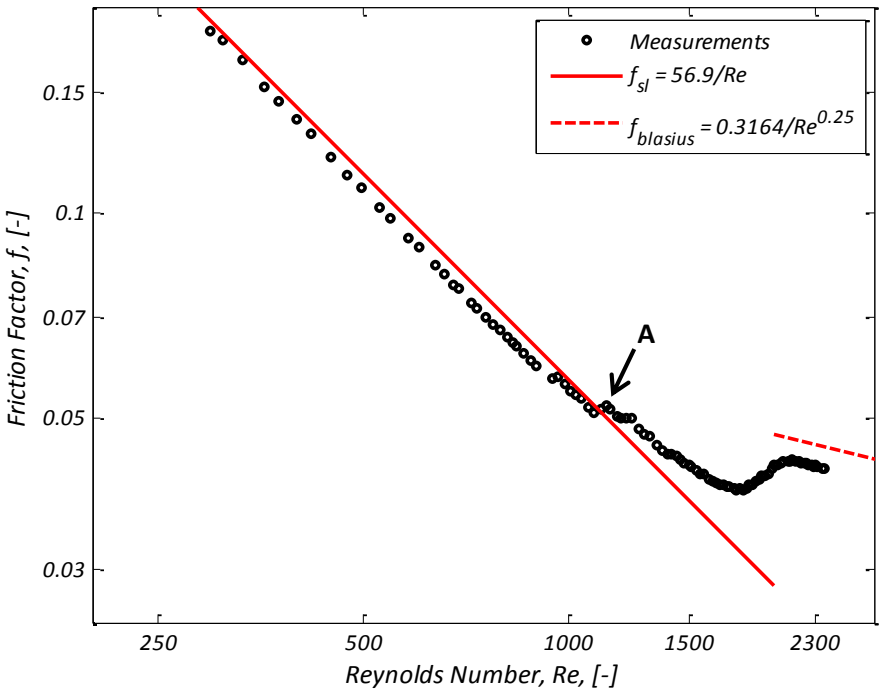

Figure 22 Adiabatic results for the 1.05 mm test section with a bellmouth inlet

The increase in friction factor of the transition regime was a direct result of the bellmouth inlet section. Changing the entry condition into the microchannel caused a change in the duration and profile of the entire regime. Figure 23 gives a magnified view of the comparison of the transition regime results for the 1.05 mm sudden contraction inlet and bellmouth inlet adiabatic results. The effect of attaching the bellmouth inlet section on the transition regime (originating from Point A) was compared to the sudden contraction inlet results. It is unclear whether this rise can be seen as the onset of the transition regime or simply a laminar regime effect caused by the changing the inlet condition. The bellmouth effect on the friction factor and Nusselt number for the diabatic experimentation provided more insight into these currently distinctive results.

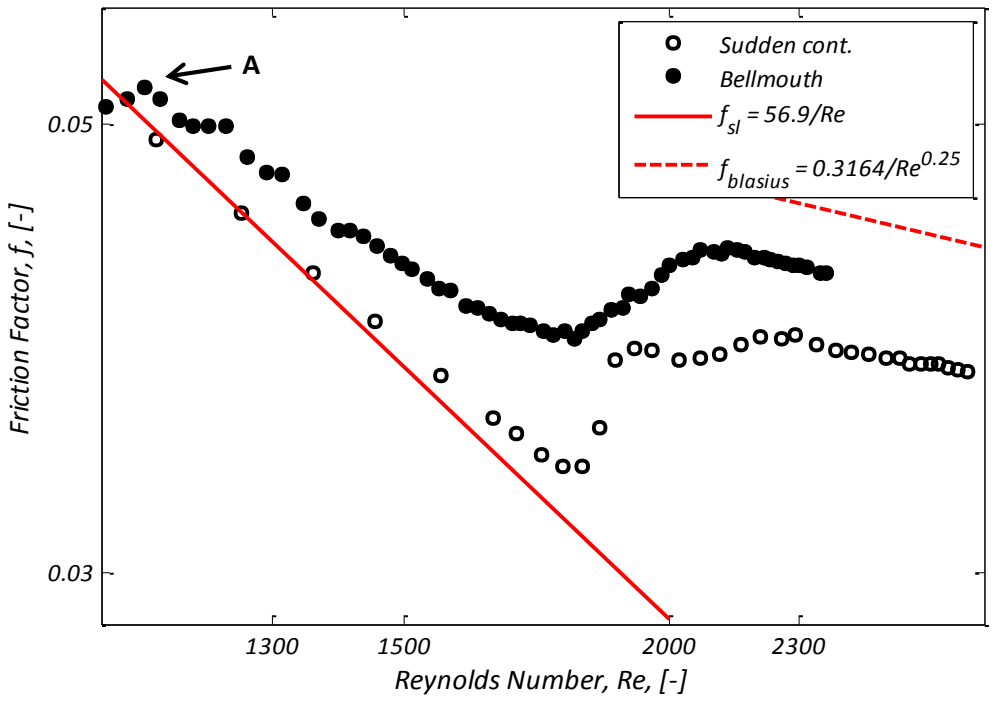

Figure 23 Comparison of the 1.05 mm sudden contraction and bellmouth adiabatic friction factor results for the transition regime

The bellmouth inlet condition offers a unique set of results and its effect in the transition regime instills curiosity in the upcoming diabatic results. Compared with the work of Olivier and Meyer [40], however, the results do not behave similarly. Olivier and Meyer experimentally investigated the effect of inlet condition on larger circular channels. Their work utilised a similar design procedure to construct the inlet condition. Their bellmouth inlet section results showed a delay in the start of the transition regime, commencing at Reynolds numbers higher than those proposed by the theory. Similar delayed transition results were found by Tam and Ghajar [39]. In this study it was, however, found that the transition occurred earlier.

The sudden contraction inlet condition was experimentally investigated for the 0.57 mm test section also under adiabatic conditions. Figure 24 presents the results of this experiment. Laminar regime results show very good agreement with the Shah and London correlation, with a maximum deviation of 5%. The Blasius correlation was applied for Reynolds numbers above 2 300 and was found to over-predict the results by approximately 15%. The transition regime commenced at a Reynolds number of approximately 2 000, and the friction factor stabilised from a Reynolds number of approximately 2 300.

Comparison of the results of the 1.05 mm and 0.57 mm sudden contraction adiabatic experiments show their equivalence (refer to Figure 25). They both behave similarly over the experimental range with respect to the conventional theory. The critical Reynolds number is slightly lower for the 1.05 mm test section by approximately 200 Reynolds numbers.

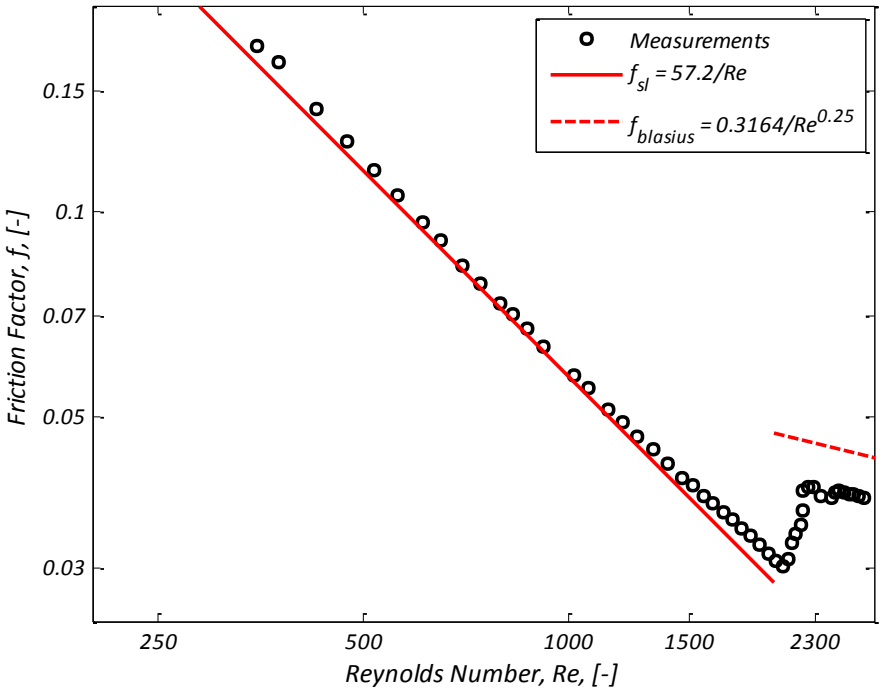

Figure 24 Adiabatic results for the 0.57 mm test section with a sudden contraction inlet

The results of the adiabatic experiments were compared with the results discussed in the literature for adiabatic experimentation. Mala and Li [3] conducted adiabatic experimentation and measured higher than theoretical friction factors and a lower value of critical Reynolds number. Jiang *et al.* [21] reported lower and equal friction factors to the theory, but did not report their critical Reynolds number. Weilin *et al.* [4] reported higher friction factors without commenting on the critical Reynolds number, while Xu *et al.* [22] and Judy *et al.* [6] reported that the theory predicted their results well and noted a critical Reynolds number of 2 300.

Wu and Cheng [23] found the critical Reynolds number to be between 1 500 and 2 000, with good agreement of the theory with their measured friction factors. Hao *et al.* [10] reported lower friction factors with respect to the theory, and found that transition commenced between a Reynolds number of 1 500 and 1 800. Steinke and Kandlikar [11] experimentally investigated laminar flow of water only, and reported lower than theoretical friction factors, while Hrnjak and Tu [12] reported good agreement with the friction factor theory and a critical Reynolds number between 2 150 and

2 290 for refrigerant R134a, with both studies conducted in the same year. Gamrat *et al.* [32] and Costaschuk *et al.* [30] both reported their friction factors were in good agreement with the theory, while their critical Reynolds numbers were reported to be 2 000 and 2 370 respectively. Barlak *et al.* [36] experimentally investigated the adiabatic friction factors for Reynolds numbers between 100 and 10 000. They found good agreement with the Poiseuille theory with the critical Reynolds number occurring between a Reynolds number of 2 000 and 2 500.

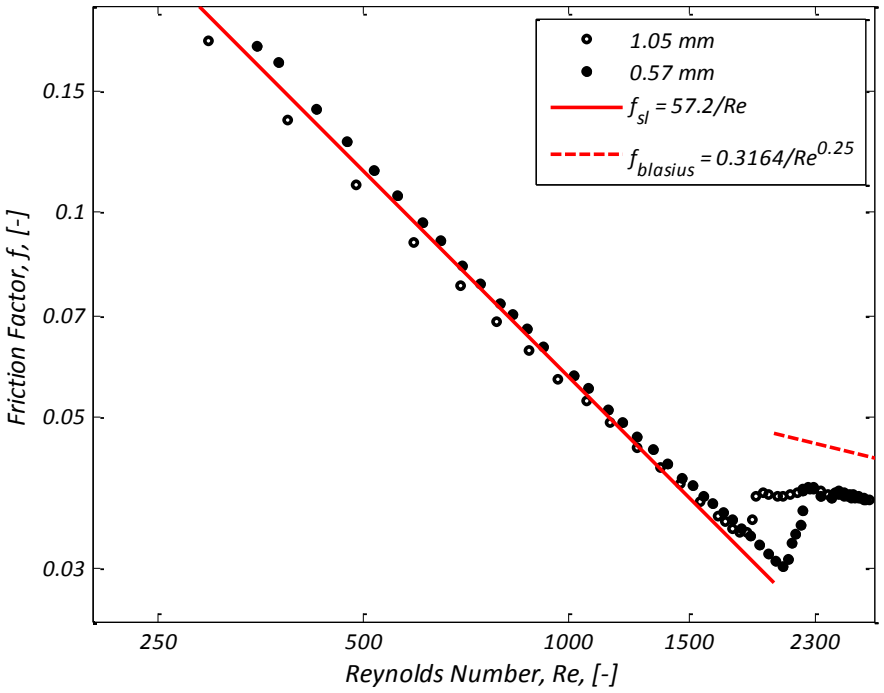

Figure 25 Comparison of the 1.05 mm and 0.57 mm sudden contraction adiabatic results

The adiabatic results of the sudden contraction 1.05 mm and 0.57 mm test sections compare well with the results of Jiang *et al*. [21], Xu *et al.* [22], Judy *et al.* [6], Wu and Cheng [23], Gamrat *et al.* [32] and Barlak *et al.* [36]. Most of the results reported in these studies were for microchannels below 500 µm in hydraulic diameter. The adiabatic results of this study expand the range of applicability of the conventional adiabatic theory to include channels of hydraulic diameters 0.57 mm and 1.05 mm.

Adiabatic experiments were conducted on the intention to validate that the test facility and the test section were working correctly. A full experiment was not run on the 0.85 mm channel, as discrete Reynolds numbers were chosen to verify correct operation. Since very few measurements were taken, the results were omitted from this study.

4.3 Diabatic results

Diabatic results formed the bulk of experimentation in this study. As discussed in Section 2.3, 21 sets of experimental scenarios were investigated for three different hydraulic diameters, three inlet conditions at three constant heat fluxes. Diabatic experimentation entailed calculating the friction factors and Nusselt numbers for each test scenario from a Reynolds number of 300 to 2 800.

Results were divided based upon the inlet condition for the three test sections. Each test section result consists of three data sets – one for each different heat flux. The results are plotted along with the relevant Shah and London [45] correlation for the given hydraulic diameter in the laminar regime, and the Blasius equation [46] in the transition regime.

4.3.1 Sudden contraction inlet section results

4.3.1.1 Sudden contraction results: 1.05 mm

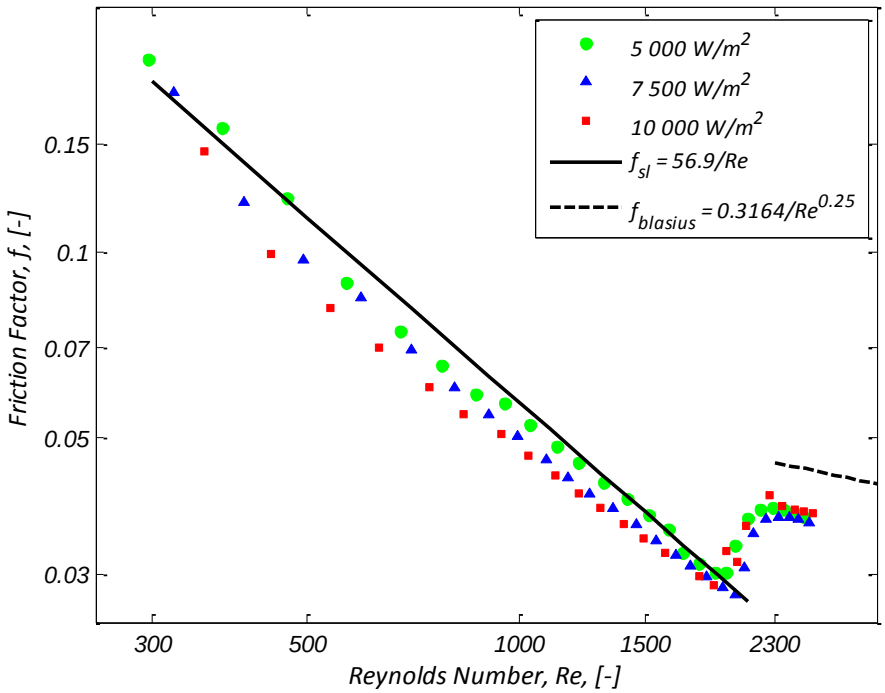

Figure 26 Diabatic friction factor results for the 1.05 mm microchannel with a sudden contraction inlet

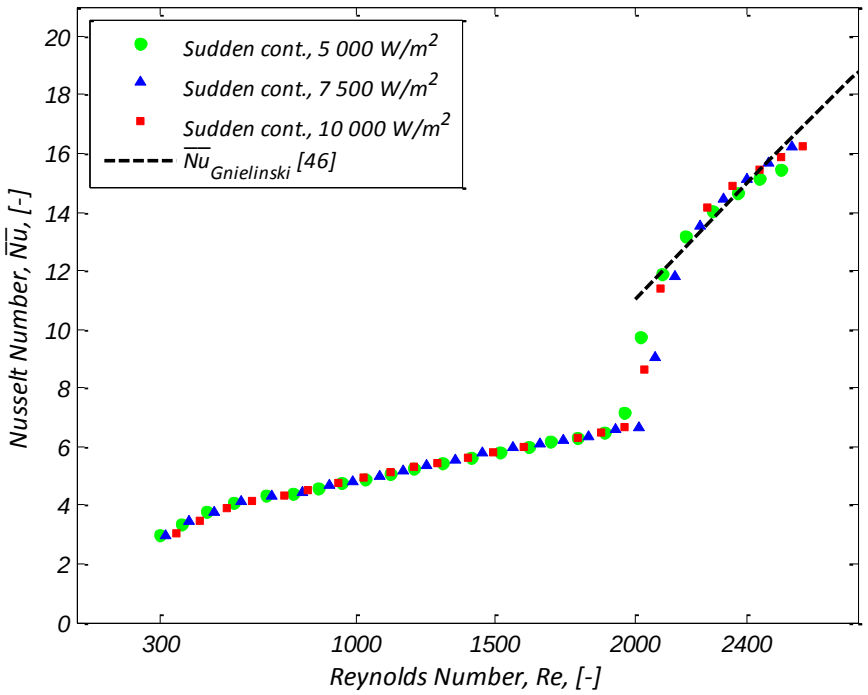

Figure 27 Nusselt number results for the 1.05 mm microchannel with a sudden contraction inlet

4.3.1.2 Sudden contraction results: 0.85 mm

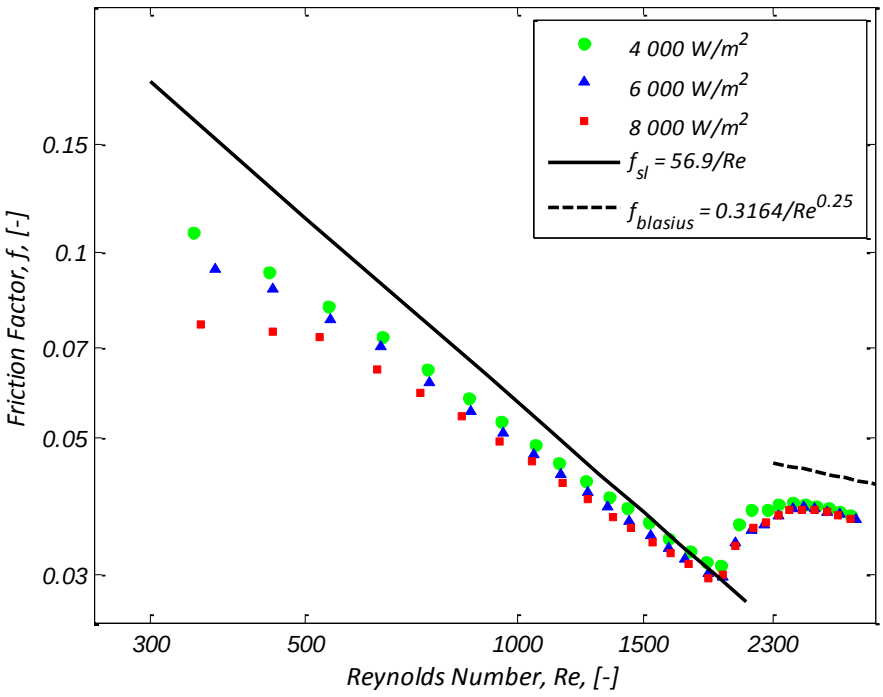

Figure 28 Diabatic friction factor results for the 0.85 mm microchannel with a sudden contraction inlet

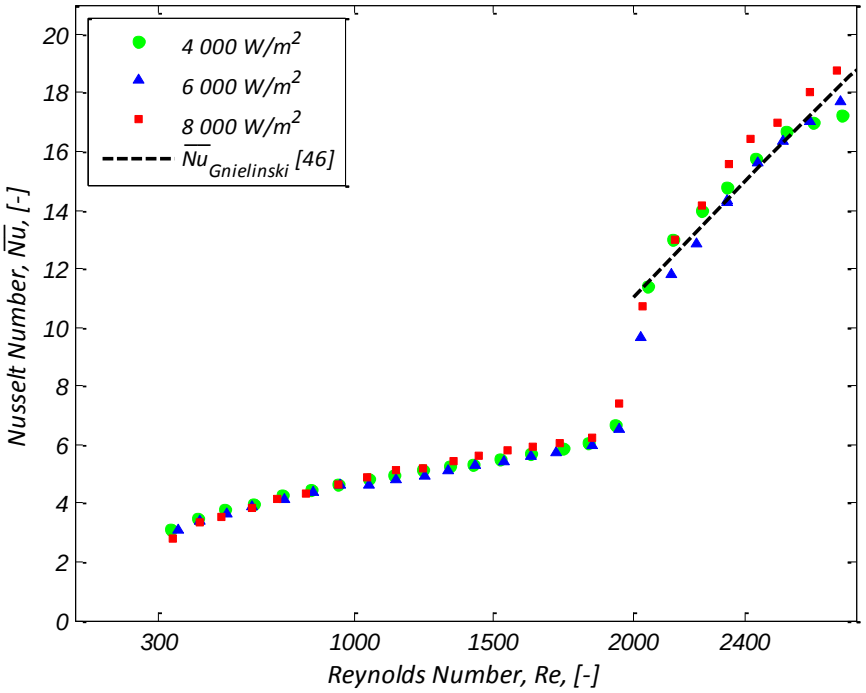

Figure 29 Nusselt number results for the 0.85 mm microchannel with a sudden contraction inlet

4.3.1.3 Sudden contraction results: 0.57 mm

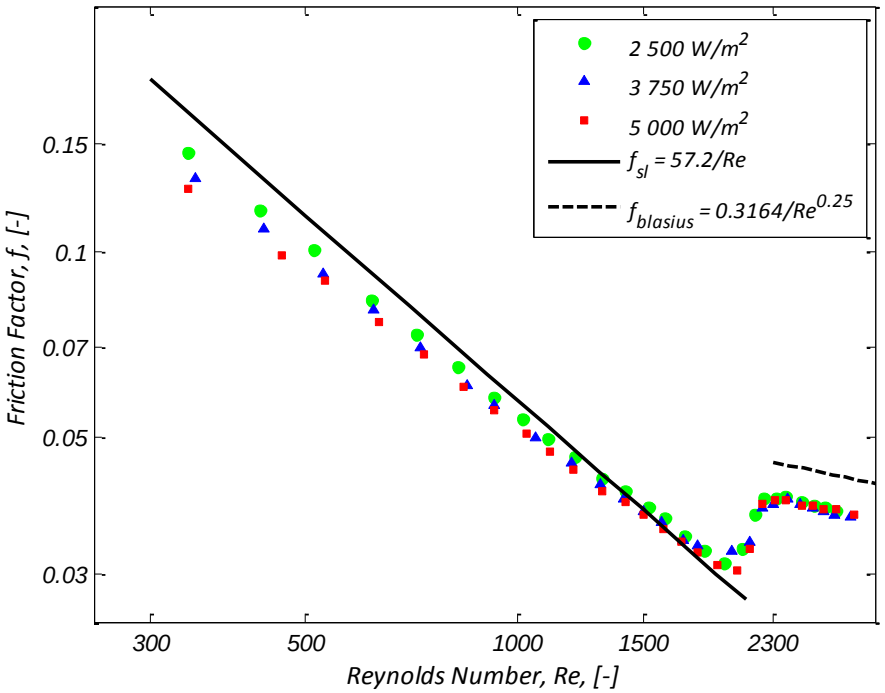

Figure 30 Diabatic friction factor results for the 0.57 mm microchannel with a sudden contraction inlet

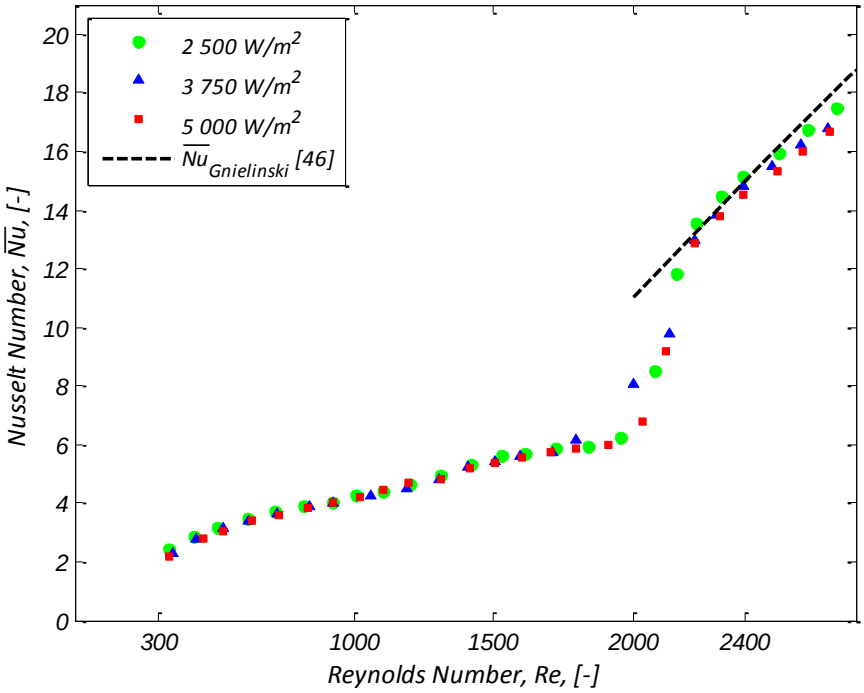

Figure 31 Nusselt number results for the 0.57 mm microchannel with a sudden contraction inlet

4.3.1.4 Summary of diabatic sudden contraction inlet results

The results of the sudden contraction inlet for the three test sections are presented for the friction factor and the Nusselt number from Figure 26 to Figure 31. Measured friction factors in the laminar regime for all three test sections were overpredicted by the Shah and London correlation [45] by up to 15% for all the test section results. The largest deviation was noticed at the lowest Reynolds numbers, especially in the case of the 0.85 mm test section, where the large deviation in results was due to the high relative uncertainty of the pressure transducer equipment. Also noticed for all three test sections in the laminar regime was the decrease in the friction factor results as the heat flux was increased. This effect can be seen in the laminar regime only, and does not affect the transition regime.

Transition regime began between Reynolds number of 1 950 and 2 000 for all three test sections. This agrees well to the literature of Céngel [46] for macro-channel flow. The transition regime lasted for a very short period of Reynolds number, and was found to stabilise at a Reynolds number of 2 300. Due to a limited experimental range, it is inconclusive whether this is a fully turbulent regime. The results where thereafter compared with the Blasius equation [46] and were found to be

approximately 14% overpredicted by the equation. This result was consistent for all three test sections, irrespective of their hydraulic diameter and heat flux inputs.

The average Nusselt number was determined in conjunction with the friction factor measurements. The heat flux input showed no influence on the results, and the Nusselt numbers in the laminar regime were noticed to be very similar with each other for each individual test section. The influence of the axial heat conduction was visible for each test section. The effect caused a reduction in the Nusselt number as predicted and occurred below the critical value determined in Section 2.3.1.1 according to equation (1). Nusselt numbers in the laminar regime were affected by the thermal and hydrodynamic entrance lengths (discussed in Section 2.3.1.2), resulting in the Nusselt number increasing in the laminar regime rather than converging to a single constant value of approximately 3.61 as documented in Céngel [46].

The transition regime commenced at a Reynolds number between 1 950 and 2 000 for the Nusselt number – the same range as with the friction factor results. The transition Nusselt numbers were short-lived as with the friction factor results and converged with the Gnielinski equation [46] at a Reynolds number of approximately 2 300. This convergence was consistent for all three test sections up to the end of the experimental range of 2 600.

Results for the sudden contraction inlet section for the three sections yielded the following conclusions:

- Laminar regime friction factor results were overpredicted by the Shah and London correlation by up to 15%.
- Late transition regime friction factor results were overpredicted by the Blasius equation by up to 15%.
- A decrease in the friction factor was observed with increasing the heat flux input.
- The measured critical Reynolds number compares well with that of the literature.
- The effect of the axial heat flux was prominent in the Nusselt number results in the laminar regime, and occurred as predicted by the literature.
- Nusselt numbers in the laminar regime do not converge to a constant value as given in the literature as the flow is not fully developed.
- Nusselt numbers in the turbulent regime converge to the Gnielinski equation.
- The friction factor and Nusselt number results both experience transition at approximately the same Reynolds number values.

- The Nusselt number was not influenced by the heat flux as was observed with the friction factor.

4.3.2 Bellmouth inlet section results

4.3.2.1 Bellmouth results: 1.05 mm

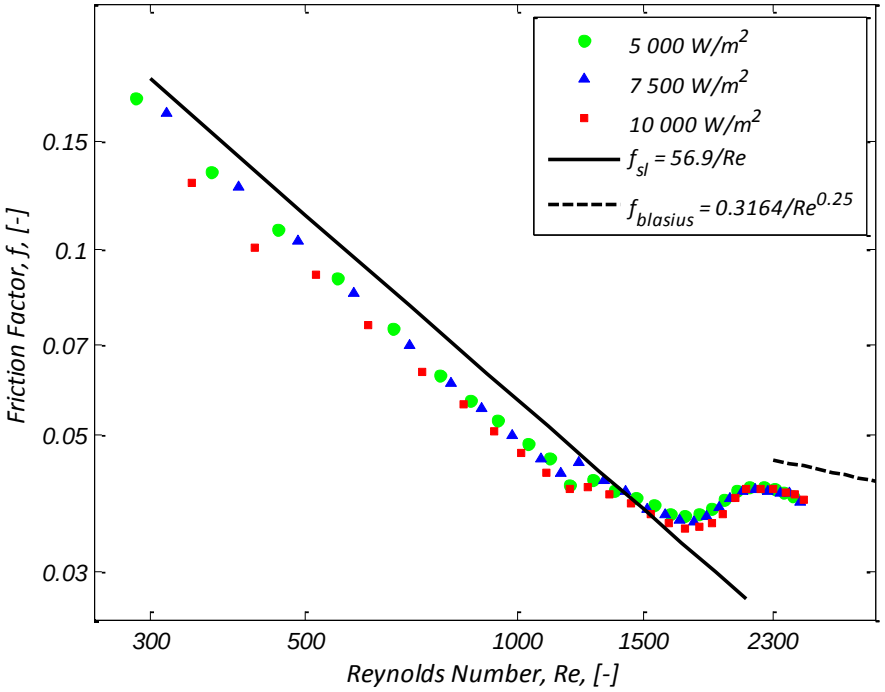

Figure 32 Diabatic friction factor results for the 1.05 mm microchannel with a bellmouth inlet

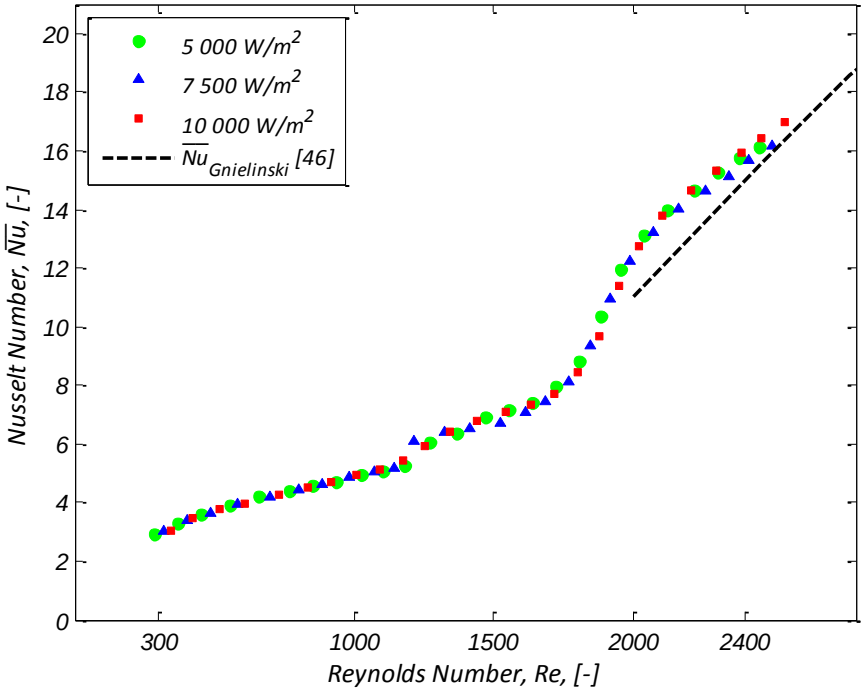

Figure 33 Nusselt number results for the 1.05 mm microchannel with a bellmouth inlet

4.3.2.2 Bellmouth results: 0.85 mm

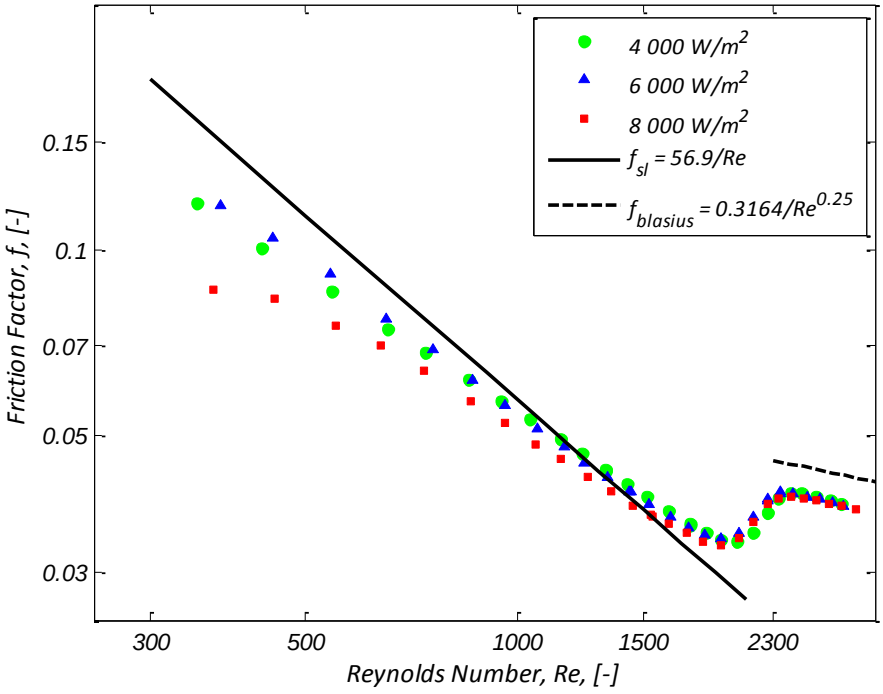

Figure 34 Diabatic friction factor results for the 0.85 mm microchannel with a bellmouth inlet

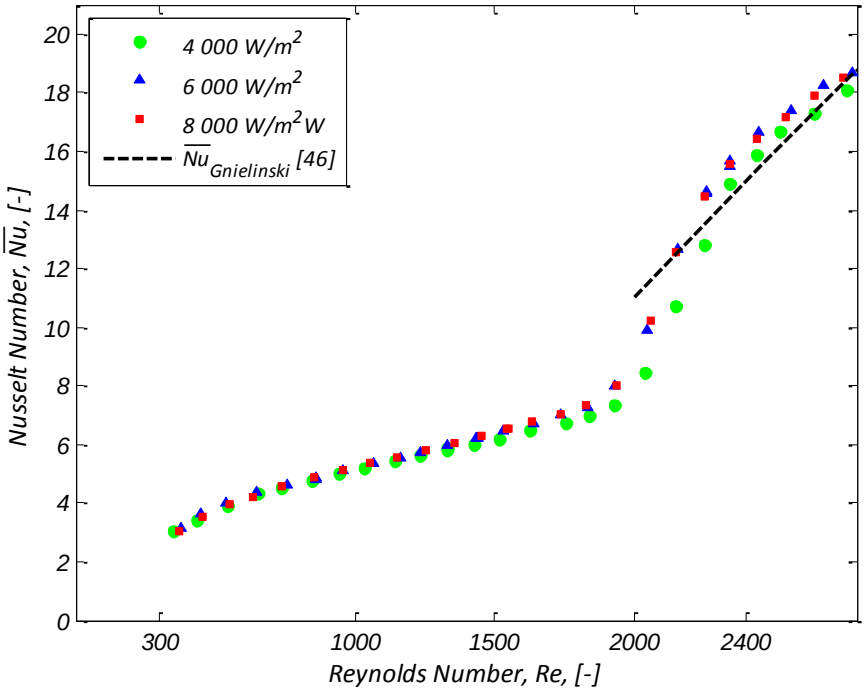

Figure 35 Nusselt number results for the 0.85 mm microchannel with a bellmouth inlet

4.3.2.3 Bellmouth results: 0.57 mm

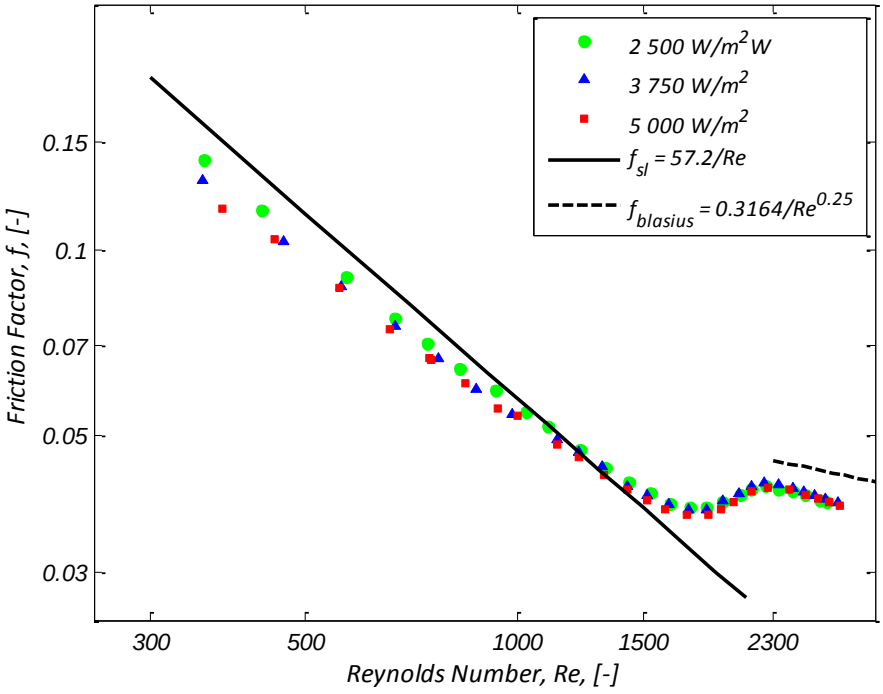

Figure 36 Diabatic friction factor results for the 0.57 mm microchannel with a bellmouth inlet

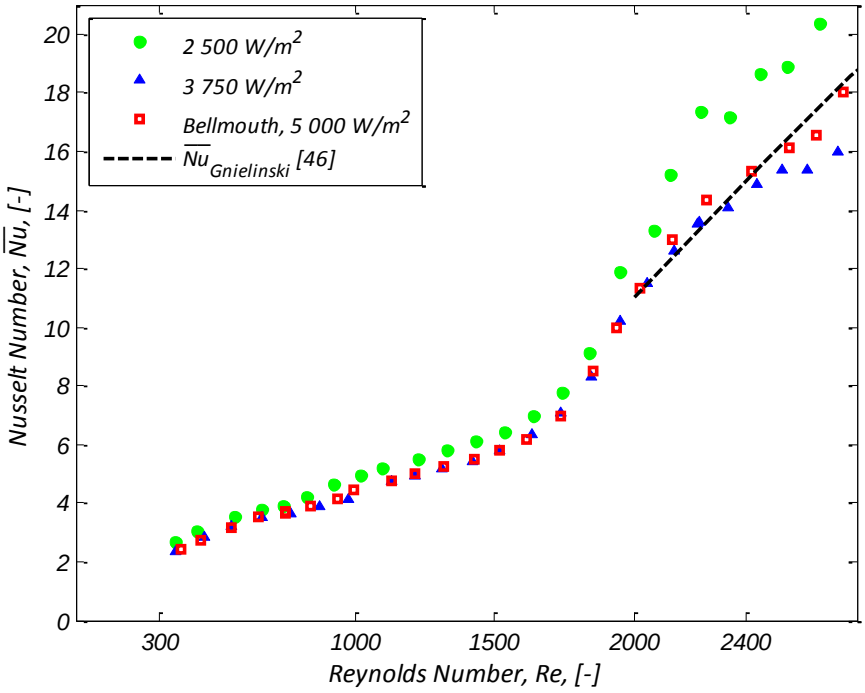

Figure 37 Nusselt number results for the 0.57 mm microchannel with a bellmouth inlet

4.3.2.4 Summary of diabatic bellmouth inlet results

The bellmouth inlet section was experimentally investigated for the three test sections to determine the effect on the friction factor and Nusselt number, and the results are given from Figure 32 to Figure 37. Friction factor results in the laminar regime were overpredicted by the Shah and London correlation [45] as with the sudden contraction inlet section. The results were up to 15% lower than the correlation. Results for the 0.85 mm test section showed a large decrease in the friction factor in the lower values of the laminar regime due to the pressure transducer uncertainty. Results also indicate a decrease in the friction factor as the heat flux input was increased. This was apparent for all three test sections.

The bellmouth inlet section showed an effect on the onset of the transition regime. Results indicated that the transition regime commenced at a Reynolds number of approximately 1 300. This early onset is consistent amongst the three test sections, and coincides with the diabatic results given in Section 4.2 where the bellmouth inlet caused a similar effect. The transition regime ended at roughly 2 300 as with the sudden contraction inlet. The profile of the transition regime is not as quick to stabilise as that of the sudden contraction inlet. The profile is more defined and smooth, with the results of the bellmouth in the turbulent regime converging with those of the sudden contraction inlet. The results were determined to be overpredicted by the Blasius equation [46] by up to 14%.

Nusselt number results were measured and determined to be similar to those of the sudden contraction inlet for the laminar regime. It can be concluded that the inlet condition has negligible effect on the axial heat conduction as its presence is still apparent in the results. The Nusselt numbers are also independent of the heat flux input as with the sudden contraction inlet results. There is an early onset of the transition regime in the Nusselt number results due to the bellmouth inlet section. Transition occurs at a Reynolds number of approximately 1 300, and enters into a much longer period of transition as with the friction factor results. The transition regime then ends at approximately 2 300 where the results converged with the Gnielinski equation [46]. The results of the 0.57 mm 2 500 W/m^2 did not show good agreement with the Gnielinski equation at the high Reynolds numbers. This was attributed to high heat losses and thermal instability of the experimentation at the low heat flux input value. Since there was no visible relationship between the heat flux and the friction factor in the transition and turbulent regimes, the results of the 0.57 mm friction factor did not show deviation at the high Reynolds numbers.

The results of both the sudden contraction and bellmouth inlets showed many similar trends in the laminar and turbulent regime for both the friction factor and Nusselt number results. The following conclusions were made for the bellmouth inlet results:

- Laminar regime friction factor results were overpredicted by the Shah and London correlation by up to 15%.
- Turbulent regime friction factor results were overpredicted by the Blasius equation by up to 15%.
- A significant increase in the transition regime results over the sudden contraction results was measured.
- A decrease in friction factor was noticed with increasing the heat flux input.
- The measured critical Reynolds number occurred earlier than the sudden contraction inlet results.
- The effect of the axial heat flux was prominent in the Nusselt number results in the laminar regime, and occurred as predicted by the literature.
- Nusselt numbers in the laminar regime do not converge to a constant value as given in the literature as the flow is not developed.
- Transition regime Nusselt numbers were higher than those measured with the sudden contraction inlet section.
- Nusselt numbers in the turbulent regime converge to the Gnielinski equation
- The friction factor and Nusselt number results both experience transition at approximately the same Reynolds number values.
- The Nusselt number was not influenced by the heat flux as was observed with the friction factor.

4.3.3 Swirl inlet section results

4.3.3.1 Swirl results: 1.05 mm

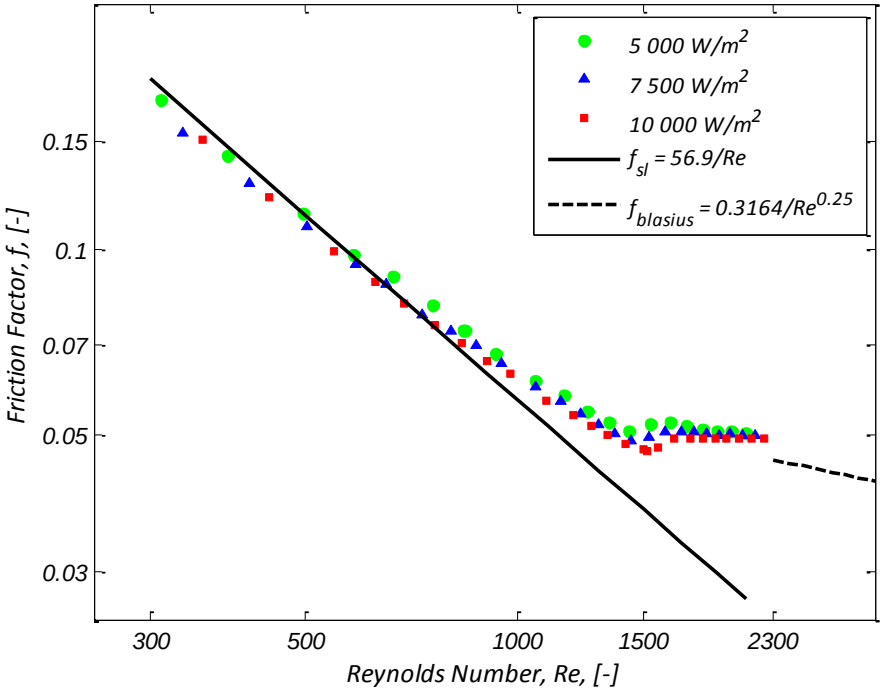

Figure 38 Diabatic friction factor results for the 1.05 mm microchannel with a swirl inlet

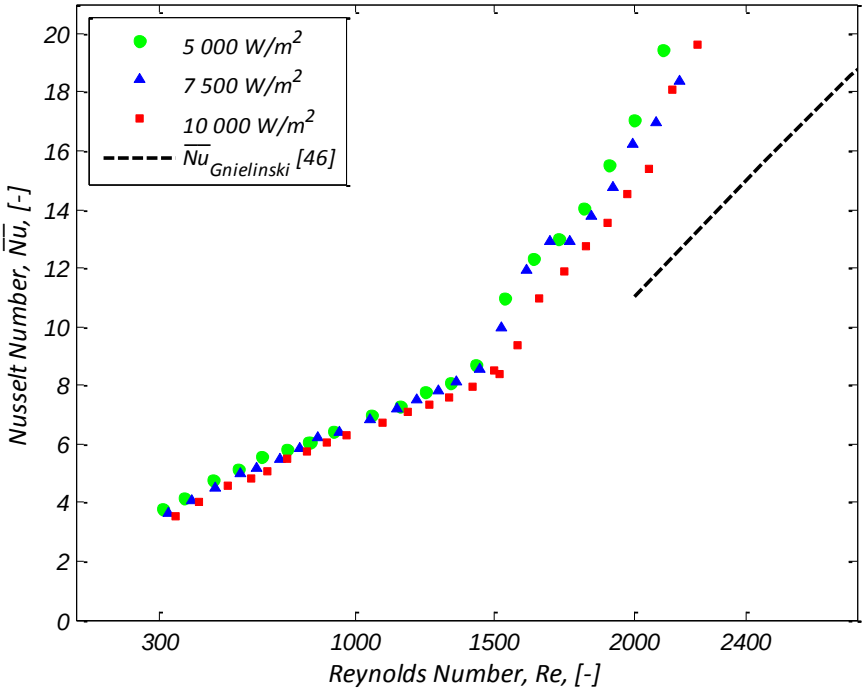

Figure 39 Nusselt number results for the 1.05 mm microchannel with a swirl inlet

4.3.3.2 Summary of diabatic swirl inlet results

The swirl inlet was a unique inlet that was fabricated for the 1.05 mm test section. Friction factor and Nusselt number results are given in Figure 38 and Figure 39. Due to the high differential pressures experienced in the channel, testing could not go further than a Reynolds number of 2 300. However, due to the nature of the flow behaviour with the swirl inlet, all three regimes were captured within this Reynolds number range.

The Shah and London correlation [45] showed good agreement to the friction factors at low values of Reynolds number. The effect of a decreasing friction factor due to an increase in the heat flux could not be established for this inlet for the measured laminar regime results. At a Reynolds number of approximately 800, the friction factor diverged significantly from this equation, resulting in a higher measured friction factor. An early transition regime began at Reynolds number of approximately 1 500 and ended shortly thereafter at 1 700. The remaining results were determined to be the turbulent regime, as no significant change was measured thereafter. Comparing the turbulent regime results to the Blasius equation shows an under-prediction of the results by approximately 15% at a Reynolds number of 2 300, though these results are inconclusive as the experimental range did not reach higher values.

The average Nusselt number results were higher than the results of the 1.05 mm sudden contraction inlet and bellmouth inlet diabatic results. The Nusselt number increased steadily until the transition regime began at a Reynolds number of approximately 1 500 (as with the friction factor results). Due to overall much higher results, the axial conduction effect could not be determined in the laminar regime. The transition regime increased quickly to the turbulent regime as deduced by Figure 39. The turbulent regime continued to rise, and was underpredicted by the Gnielinski equation [46] by approximately 50%.

The swirl inlet resulted in significantly different results than those of the sudden contraction and bellmouth inlets. The following conclusions were made for the inlet:

- Laminar regime friction factors agree well with the Shah and London correlation up to a Reynolds number of 800, thereafter increasing significantly.
- An early transition regime occurred for the friction factor.
- Turbulent regime friction factor results were inconclusive.
- Higher Nusselt numbers were measured in the laminar regime.

- Turbulent regime results were up to 50% larger than the conventional theory and the other inlet sections.
- The effect of the axial heat conduction could not be established.
- The Nusselt number was not influenced by the heat flux as was observed with the friction factor.

4.4 Summary of results

The sudden contraction, bellmouth and swirl inlets were experimentally investigated for three microchannel hydraulic diameters of 1.05 mm, 0.85 mm and 0.57 mm. Friction factors and Nusselt numbers were determined, and there was a noticeable difference in results attributed to the addition of the inlet sections to the test sections.

The sudden contraction inlet results were showed good agreement to the conventional theory. The bellmouth inlet section enhanced the transition regime significantly, while the swirl inlet produced both higher friction factor and Nusselt number results.

The research into heat transfer and pressure drop in microchannels has resulted in very mixed results. The results of this study agree with the work of some of the researchers, such as Jiang *et al.* [18], and similarly with the works of Natrajan and Christensen [13], and Moharana *et al*. [37]. The effect of inlet conditions has not specifically been investigated according to the literature study conducted, and the sudden contraction inlet results were used to compare the results of the literature with this study. The transition regime results also provide new data for microchannel flow. Most of the research conducted in the literature study only focuses on the laminar and/or turbulent regimes, but authors such as Morini *et al.* [14] have started investigating the transition regime.

5 Results: Analysis and comparison

5.1 Introduction

The results of the friction factors and Nusselt numbers in Chapter 4 show consistent trends with respect to the inlet conditions. Comparisons were made for this study with the literature, and further knowledge into the effects of inlet conditions on the friction factor and Nusselt number is required to validate this study. The results were compared with each other, and the effects of the inlet conditions were quantified.

5.2 Friction factor analysis

The diabatic friction factors for the 1.05 mm test section for all three inlet conditions are presented in Figure 40. The results compare the effect of the inlet sections for the entire experimental range for the 1.05 mm test section. The results of the bellmouth and swirl inlets, when compared to the sudden contraction inlet, show a large result variance, especially for the swirl inlet results. Bellmouth results were equivalent to the sudden contraction results in the laminar regime but increased up to 30% in the transition regime. The swirl laminar friction factors increased between 15% and 30% over the laminar sudden contraction results until the transition regime was reached at a Reynolds number of approximately 1 500, where results increased up to 72%.

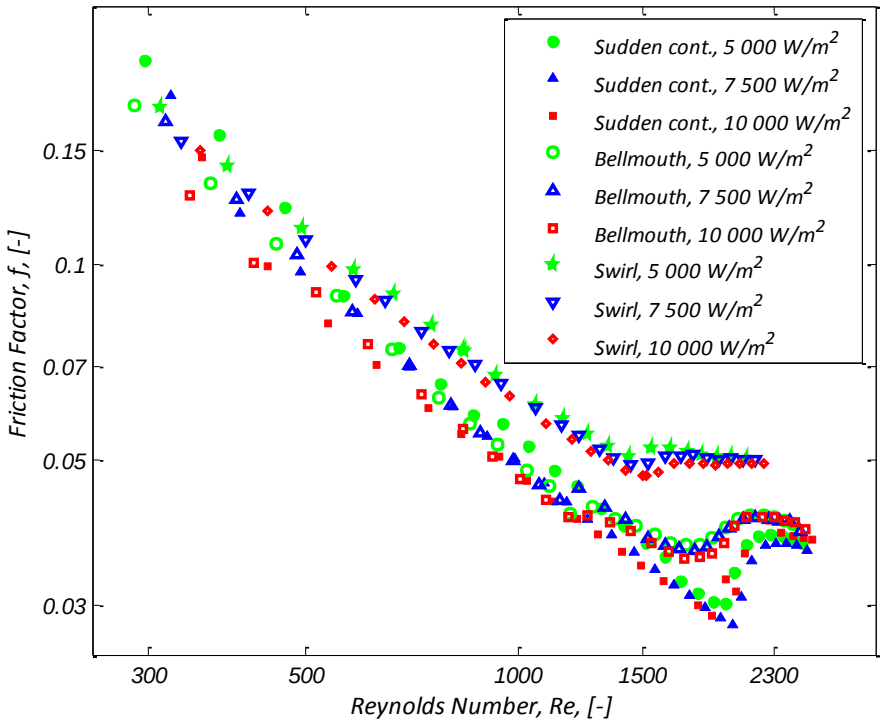

Figure 40 Diabatic friction factor results for the 1.05 mm microchannel for all three inlet conditions and heat fluxes

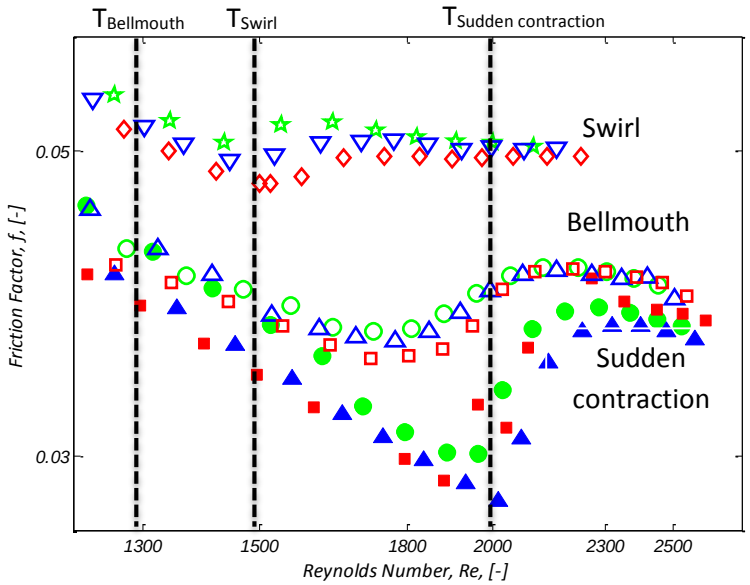

Figure 41 Magnified view of transition regime in 1.05 mm microchannel for all three inlet conditions and heat fluxes. Legends of Figure 40 to be used. The "T" symbols indicates the beginning of transition.

The Reynolds number at which transition occurs is shown in Figure 41. The point of transition the sudden contraction inlet shows good agreement to the conventional theory, where transition occurs at a Reynolds number of approximately 2 000. The bellmouth transition point occurs at

approximately 1 300, with an increase in friction factors of between 5% and 30%. The bellmouth results then converge to the sudden contraction results at a Reynolds number of 2 500. The swirl inlet transition regime began at a Reynolds number of approximately 1 500 with up to 72% higher results. Friction factors did not converge to the sudden contraction results thereafter.

As discussed in Section 4.3.1.4, there was no sign of an increase or decrease in friction factors in the transition and turbulent regimes with a change in heat flux. This is apparent in Figure 40 for the sudden contraction inlet condition. There was a sign of a friction factor decrease in the bellmouth inlet transition results, but this converged into an almost equal value in the turbulent regime. Similar results were found for the remaining two test sections. Figure 42 gives the plot of the comparison of the inlet conditions for the 0.85 mm test section. The results show fewer enhancements of the friction factors with the addition of the bellmouth inlet.

Figure 43 represents the results of the 0.57 mm diabatic friction factors. Results showed an early onset of the transition regime as with the 1.05 mm test section. The results in the laminar regime showed very good agreement with each other until a Reynolds number of approximately 1 300, where a noticeable increase in the bellmouth inlet results (as was found with the 1.05 mm bellmouth inlet results). The flow entered the turbulent regime for both inlets at a Reynolds number value of 2 300, where the results converged to a similar value.

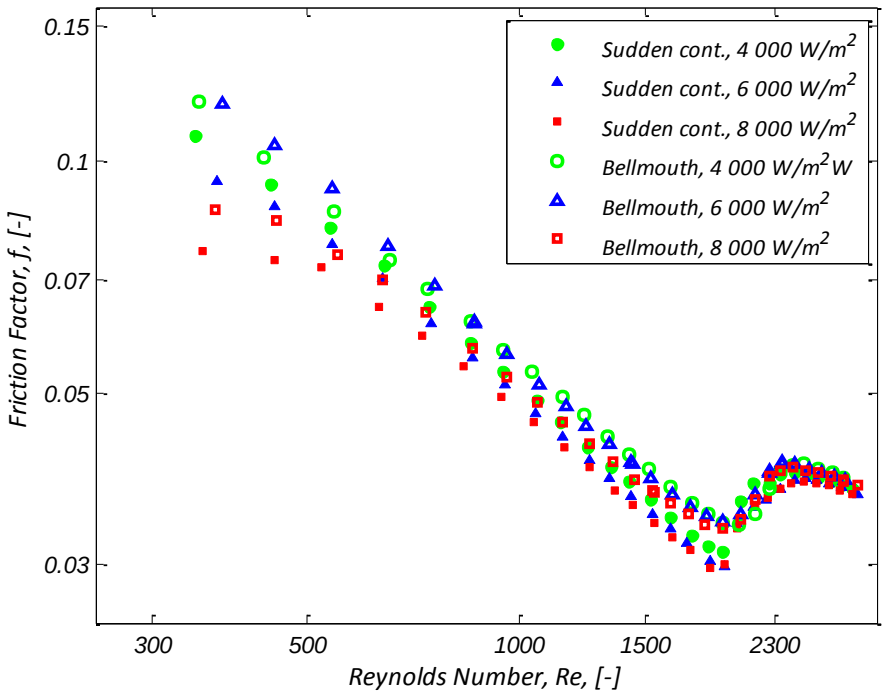

Figure 42 Diabatic friction factor results for the 0.85 mm microchannel for two inlet conditions and three heat fluxes

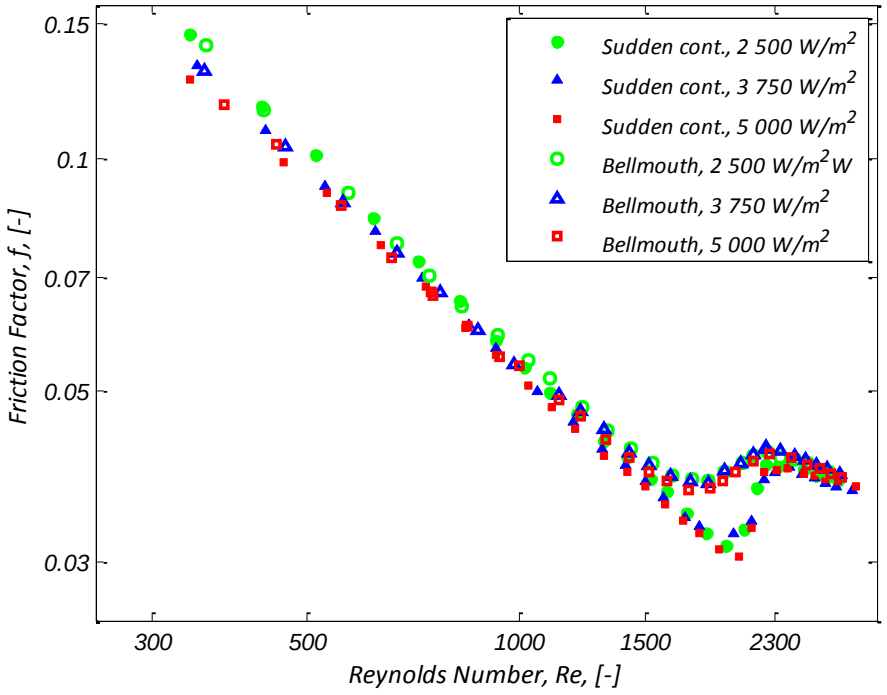

Figure 43 Diabatic friction factor results for the 0.57 mm microchannel for two inlet conditions and three heat fluxes

The friction factors for the inlet conditions for each test section were compared, and the increase of the friction factor due to the inlet conditions is given in Table 15. A conclusion can be made that inlet conditions affect the flow significantly and its effects cannot be discarded during experimental studies. The increase in the friction factor can be seen as a negative effect, as a greater pumping power is required to overcome the pressure drop in the channel.

Hydraulic diameter	***Inlet***	***Increase***	***Region***
1.05mm	Bellmouth	5% - 30%	Transition
	Swirl	15% - 72%	All
0.85mm	Bellmouth	7% - 15%	All
0.57mm	Bellmouth	5% - 30%	Transition

Table 15 Comparison of the increase in friction factor results for the different inlet conditions over the sudden contraction inlet

5.3 Nusselt number comparison

As with the friction factor, significant differences were noted in the results of the average Nusselt numbers. The inlet sections increased the pressure drop along the length of the channel, but also increased its heat transfer. Figure 44 represents the results of the 1.05 mm diabatic test results for the three inlet conditions. The results of the sudden contraction and bellmouth inlet were equal up to a Reynolds number of approximately 1 300. The bellmouth inlet results then deviated from the trends of the sudden contraction and entered into an early enhanced transition regime. At a Reynolds number of approximately 2 300, the Nusselt numbers began converging into each other. The Gnielinski equation predicted the Nusselt number in turbulent regime very accurately above a Reynolds number of 2 300.

The swirl inlet results were higher from the lowest value of Reynolds number. Due to the swirl effect, as can be expected, a higher heat transfer coefficient was measured through its experimental range. The results showed an increase in heat transfer between 15% and 120% throughout the entire experimental range when compared with the results of the sudden contraction inlet. The bellmouth inlet results showed an increase of between 10% and 70% only in the transition regime. The swirl turbulent regime results are underpredicted by the Gnielinski equation by approximately 50%, and compared with the sudden contraction and bellmouth inlets, the turbulent regime commences at a Reynolds number of approximately 1 700.

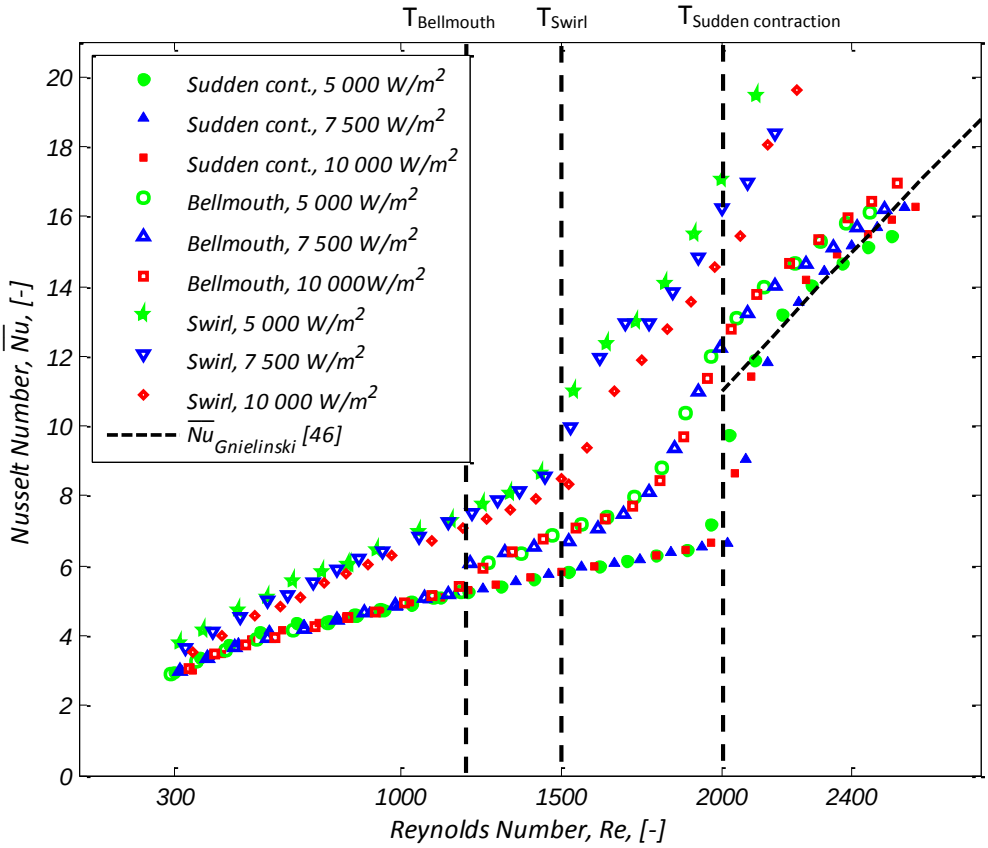

Figure 44 Nusselt number results for the 1.05 mm microchannel for all three inlet conditions and heat fluxes. The "T" symbol indicates transition

Similar experimental comparisons were done for the 0.85 mm and 0.57 mm test sections. Figure 45 represents the results of the 0.85 mm Nusselt number. As with the results of the 1.05 mm test section, the average Nusselt number is approximately the same in the laminar regime below a Reynolds number of 1 000. Thereafter, an increase of approximately 15% occurred until the onset of transition. There was no evident enhancement of the transition regime, which contradicts the effect this inlet section has with the 1.05 mm test section results. This point is noted, and will be taken into consideration. The results converge into the Gnielinski equation in the turbulent regime, as with the 1.05 mm turbulent Nusselt numbers using similar inlets.

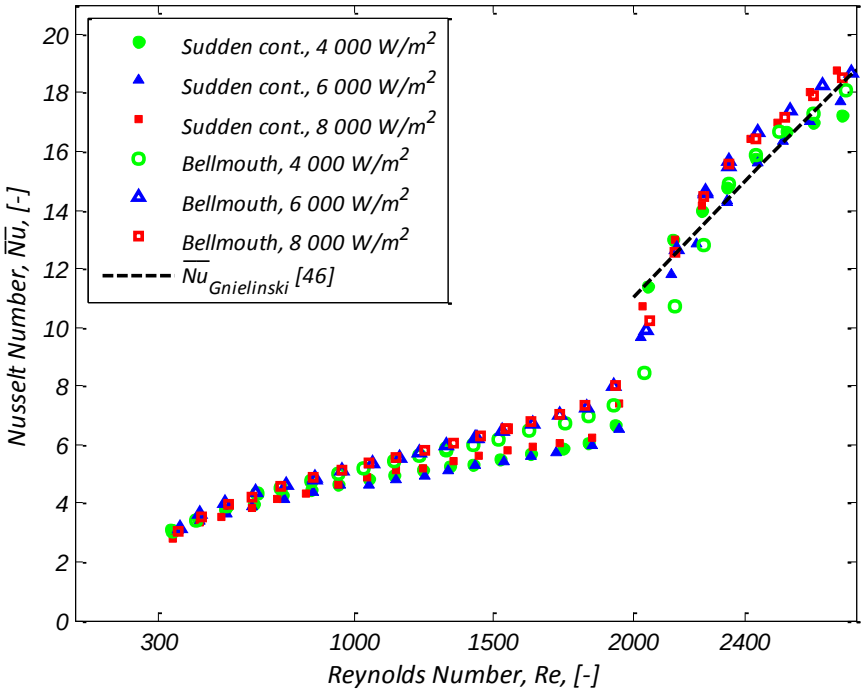

Figure 45 Nusselt number results for the 0.85 mm microchannel for the two inlet conditions and three heat fluxes

The average Nusselt number results for the 0.57 mm test section showed good resemblance to the 1.05 mm test section. Figure 46 gives the values of the Nusselt numbers for 0.57 mm results for the two inlets. The data showed very similar results to the 1.05 mm test section with respect to both inlets. There was an enhancement of the transition regime Nusselt number with the bellmouth inlet in comparison with the sudden contraction results. The transition regime commenced earlier at a Reynolds number of approximately 1 500.

Results below a Reynolds number of 1 000 had a visible axial heat conduction effect as with the other test sections. The laminar results continued to increase thereafter until the commencement of the transition regime for both inlets. The turbulent results, which began at a Reynolds number of approximately 2 300, were well predicted by the Gnielinski equation. The results of the 10 W bellmouth inlet showed high Nusselt number instability, particularly in the turbulent regime. This instability was caused by a low wall to bulk fluid temperature difference accuracy.

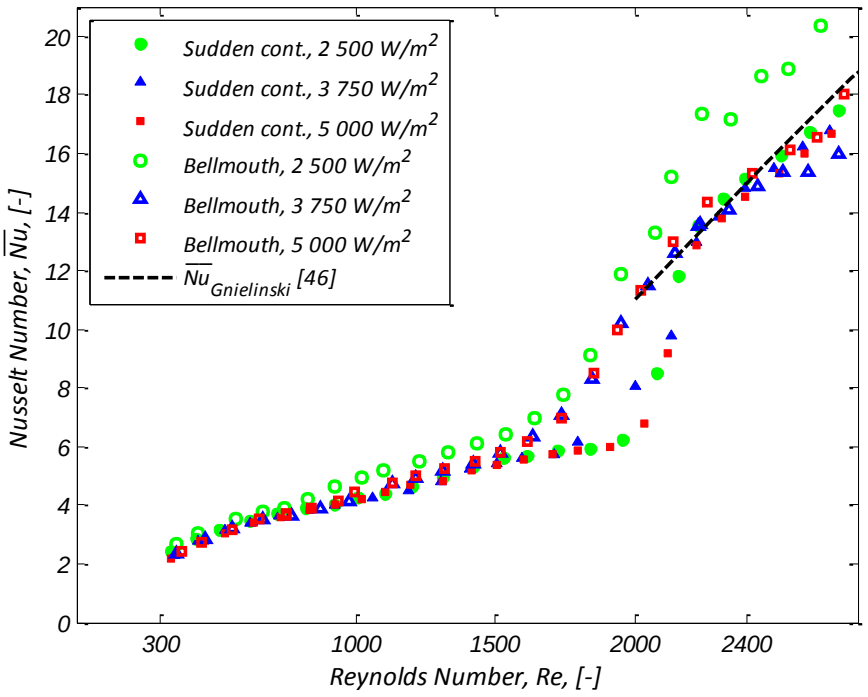

Figure 46 Nusselt number results for the 0.57 mm microchannel for the two inlet conditions and three heat fluxes

The results of the average Nusselt number showed good consistency with each other in all three regimes. The 0.85 mm bellmouth results do not show as great an enhancement of the Nusselt number in the transition regime as the 1.05 mm and 0.57 mm diameters in the transition regime. The cause may be due to an alignment problem or an inlet design problem. Since there was a noted enhancement of the 1.05 mm and 0.57 mm bellmouth results, the results of hydraulic diameter experiments bound by these dimensions should theoretically conform. Further investigation of the effects of inlet condition in microchannels will assist in this matter.

The effect of the axial heat conduction was observed for all three test sections as predicted by Maranzana *et al.* [38]. Using equation (1), the significant range of its effect was accurately predicted. The axial conduction effect cannot be overlooked, and it is proposed to use the equation as a design criterion for future studies.

The results in the laminar regime increased steadily until the commencement of the transition regime. Similar higher values of the Nusselt number were reported in the works by Natrajan and Christensen [13], Li *et al.* [16] and Garimella and Singhal [9]. The effect of entry length in both the hydrodynamic and thermal conditions must be investigated to account for developing flow. Due to the small diameters of microchannels, the entry lengths can be much longer than the length of the

channel (as discussed in Section 2.3.1.2). This effect must be compensated for to allow accurate prediction of the heat transfer in microchannels for developing flow.

The quantity of the enhancement over the sudden contraction for the three test sections is given in Table 16. The results showed the improvement of heat transfer with the addition of inlet conditions. Most notably, the swirl inlet heat transfer is enhanced by up to 120% over that of the sudden contraction.

Hydraulic diameter	***Inlet***	***Enhancement***	***Region***
1.05mm	Bellmouth	10% - 70%	Transition
	Swirl	15% - 120%	All
0.85mm	Bellmouth	10% - 20%	Transition
0.57mm	Bellmouth	10% - 66%	Transition

Table 16 Comparison of enhancement of Nusselt number results for the different inlet conditions over the sudden contraction inlet

5.4 The Colburn *j*-factor

The Colburn *j*-factor provides a way of representing the Nusselt number taking into account the varying Prandtl number. Results for the *j*-factor were determined to represent the Nusselt number in a form that could be well compared with the friction factor. By relating the *j*-factor and friction factor, it is possible to link them to each other. The *j*-factor was calculated using equation (20).

5.4.1 Comparison of *j*-factor of the different inlet conditions

The *j*-factor is plotted against the Reynolds number on a logarithmic scale to compare with the results of the friction factor. Figure 47 represents the results of the *j*-factor for all the inlet conditions of the 1.05 mm test section.

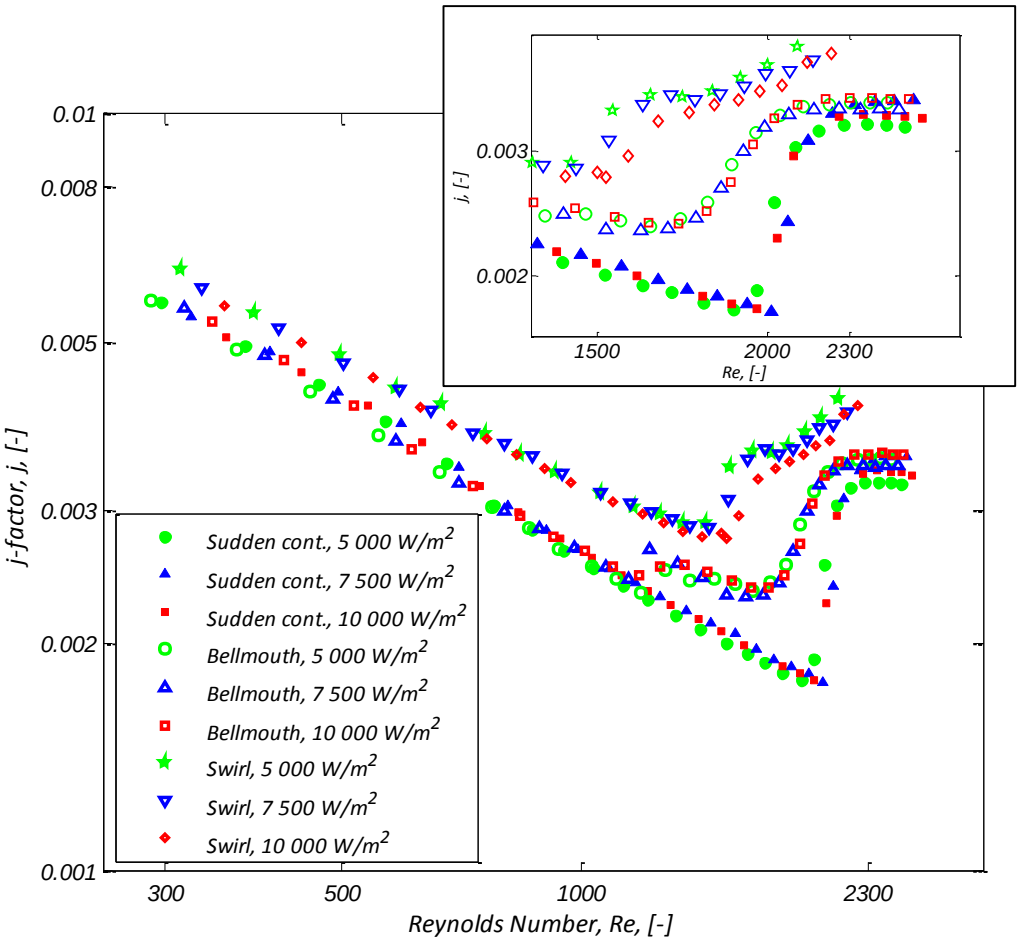

Figure 47 Colburn j-factor results for the 1.05 mm microchannel for the three inlet conditions and heat fluxes

Figure 48 and Figure 49 represent the results of the Colburn *j*-factor for the 0.85 mm and 0.57 mm test sections respectively.

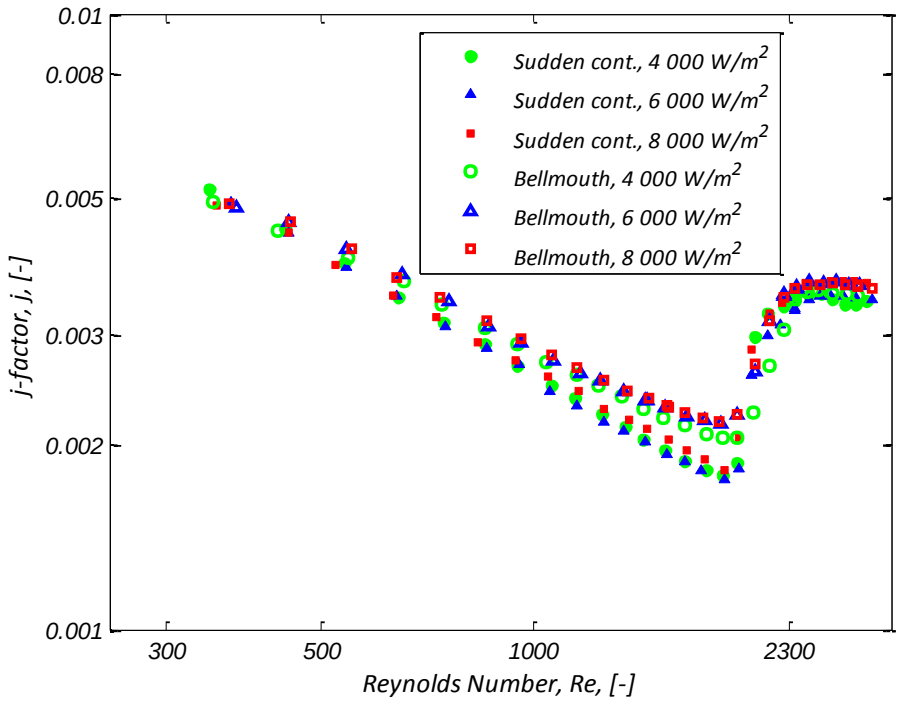

Figure 48 Colburn *j*-factor results for the 0.85 mm microchannel for the two inlet conditions and three heat fluxes

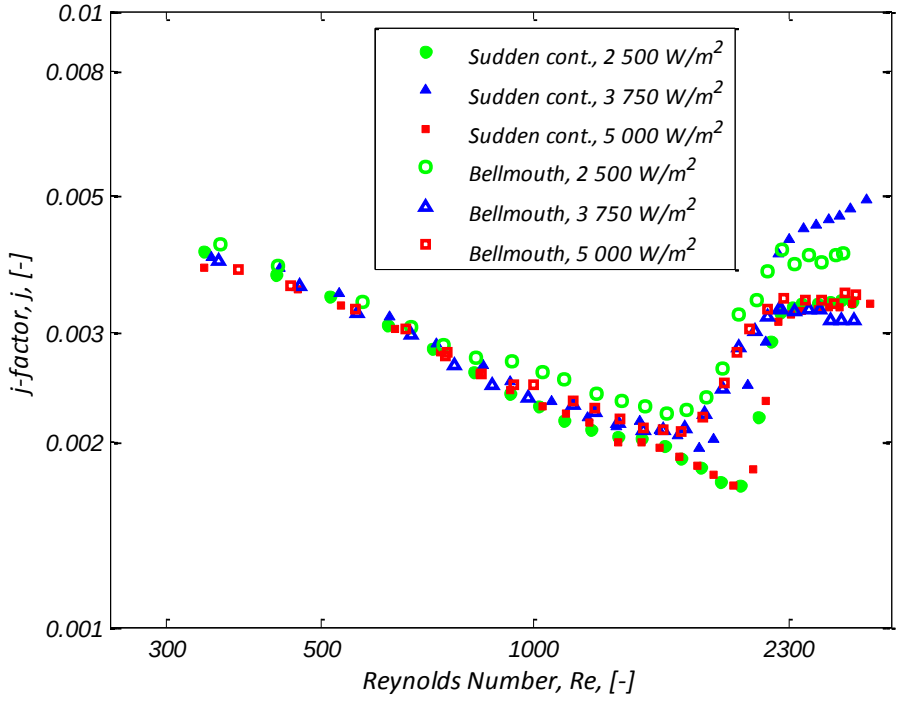

Figure 49 Colburn *j*-factor results for the 0.57 mm microchannel for the two inlet conditions and three heat fluxes

The results of the Colburn *j*-factor showed the effects of the inlet conditions on the heat transfer. As with the friction factor and Nusselt number results, the *j*-factor captures the bellmouth inlet

enhancement of the transition regime for the three test sections. The swirl inlet results are much higher throughout the experimental range than reported before. The turbulent regime results do not converge into a constant value for all the test cases.

5.4.2 Relationship between the friction factor and the *j*-factor

The friction factor and Colburn *j*-factor results can be linked together due to their profile shape similarities as can be seen in Figure 50. This figure represents the 1.05 mm sudden contraction results for the three constant surface heat flux boundary conditions. The critical Reynolds number is the same in both sets of results, and all three flow regimes can be depicted very easily. The effect of the decreasing friction factor with respect to increasing the heat input is not visible in the *j*-factor results. A change in gradient in the *j*-factor results below a Reynolds number of 500 is present, and this represents the axial heat conduction effect, which occurred during experimentation. Figure 52 to Figure 57 compare the *j*-factor and friction factor results of the remaining test sections and their respective inlet sections. Figure 51 compares the results of the equation to measurement results.

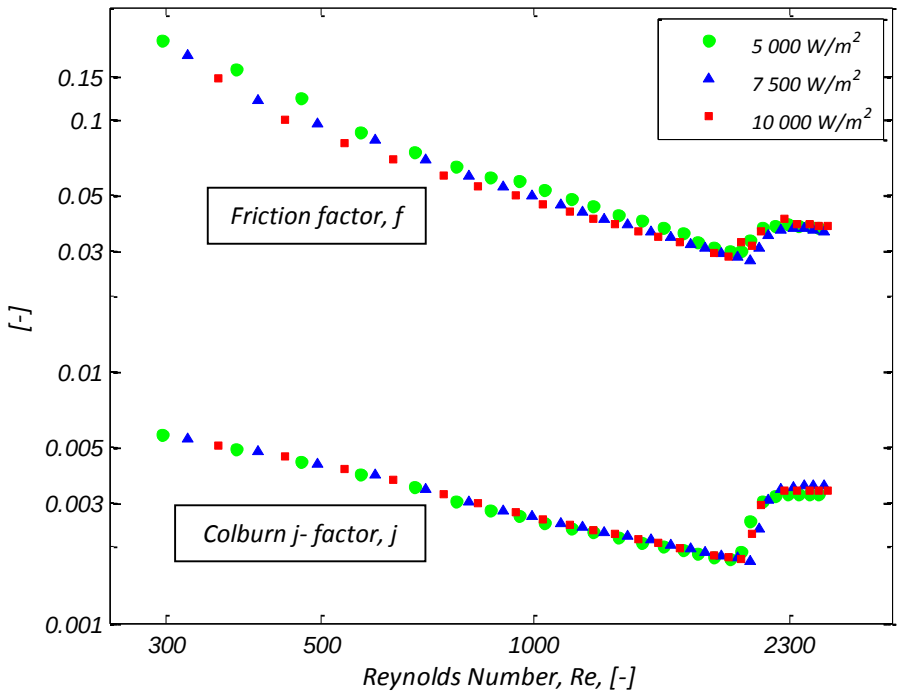

Figure 50 Comparison of 1.05 mm sudden contraction inlet friction factor and Colburn *j*-factor results

Using the friction factor and *j*-factor results for the sudden contraction inlet sections, the data was compared on a logarithmic scale to determine any relationships between the two. Comparing the results revealed that there is a strong correlation between the friction factor and *j*-factor. Sudden contraction results were used to remove the effect of inlet conditions from the relationship, thereby resulting in a generic correlation. The relationship was derived with the intention to create a method of predicting the friction factor without the need for a differential pressure measurement. The relationship can alternatively be used for prediction of the Nusselt number and the heat transfer coefficient without the use of wall or bulk fluid temperature measurements. The relationship is given by equation (21).

$$f_{pred} = \exp\left(\ln(j)\left(\ln\left(\frac{\ln(Re)}{6} + 0.5\right)\right)\right) \quad \textbf{(21)}$$

Reorganising equation (21) and substituting equation (20) for the *j*-factor, a relationship for predicting the Nusselt number in terms of the friction factor, Reynolds number and Prandtl number was formed, given by equation (22).

$$\overline{Nu}_{pred} = RePr^{\frac{1}{3}} \exp\left(\frac{\ln(f)}{\ln\left(\frac{\ln(Re)}{6} + 0.5\right)}\right) \quad \textbf{(22)}$$

Both equations are valid for the full Reynolds number range. Figure 51 plots the results for a 1.05 mm bellmouth experiment and the *j*-factor relationship equation (21). The relation captures the results of the spike (point A – described in Section 4.2) in the laminar regime results where the bellmouth inlet condition caused a sudden change to the transition regime.

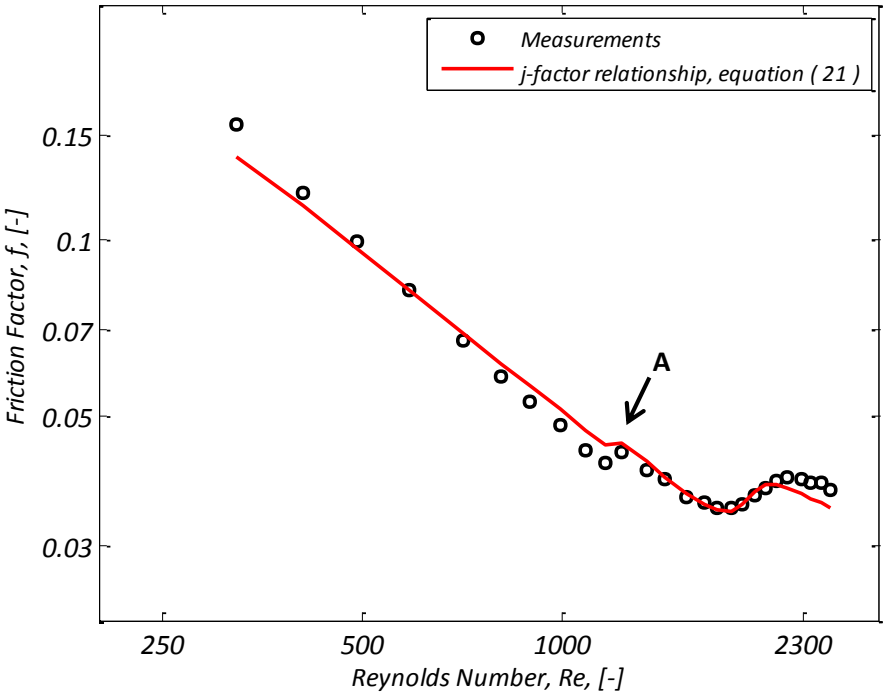

Figure 51 Colburn *j*-factor relationship comparison with the friction factor results for the 1.05 mm microchannel with a bellmouth inlet at 7 500 W/m²

The comparison of the friction factor and *j*-factors for the bellmouth and swirl inlets for the 1.05 mm test section is given below in Figure 52 and Figure 53.

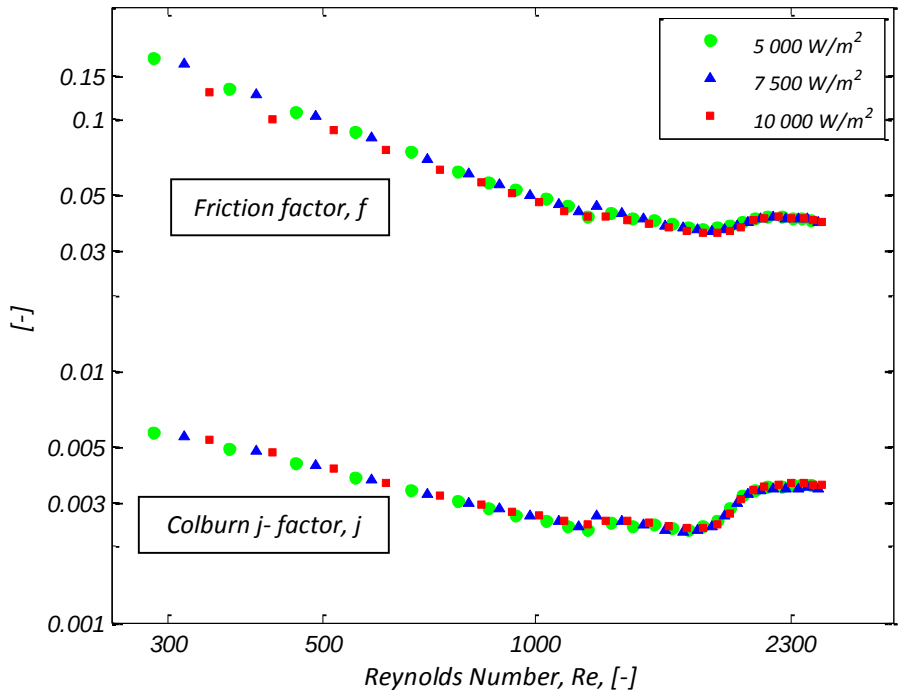

Figure 52 Comparison of 1.05 mm bellmouth inlet friction factor and Colburn *j*-factor results

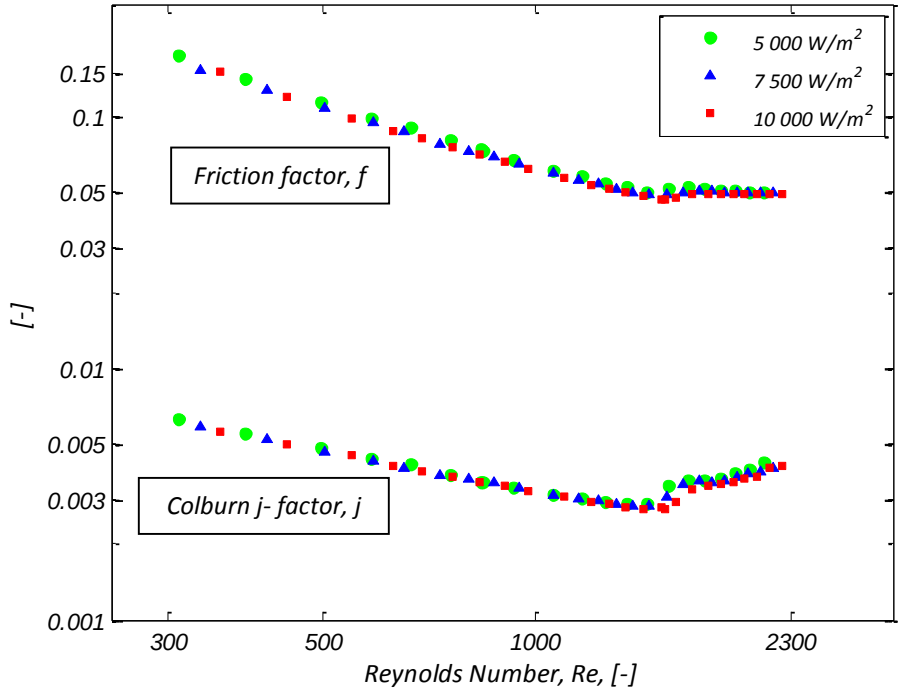

Figure 53 Comparison of 1.05 mm swirl inlet friction factor and Colburn *j*-factor results

The results of the 0.85 mm microchannel with the sudden contraction and bellmouth inlets are given in Figure 54 and Figure 55.

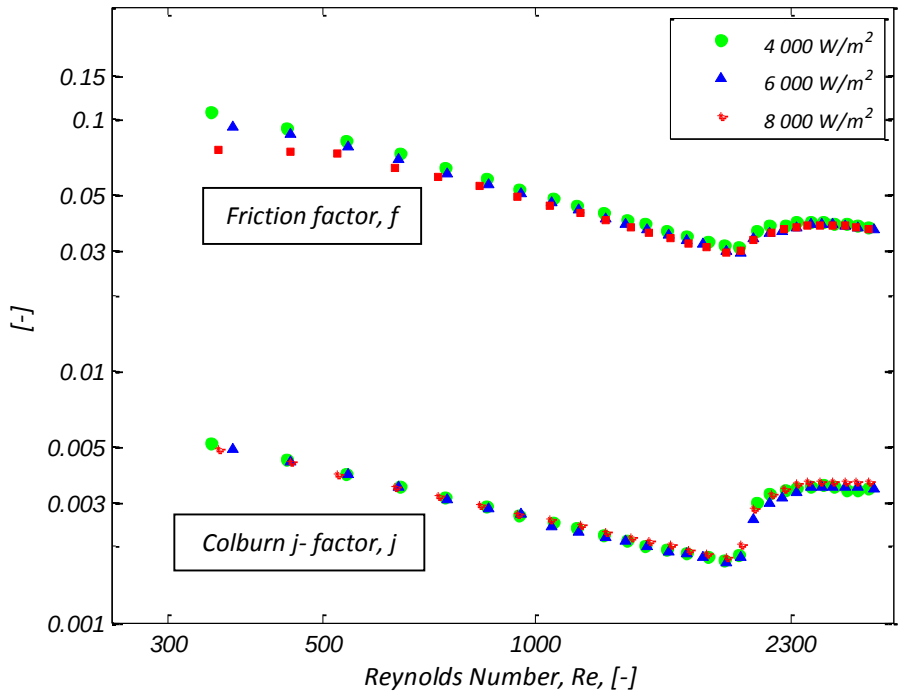

Figure 54 Comparison of 0.85 mm sudden contraction inlet friction factor and Colburn *j*-factor results

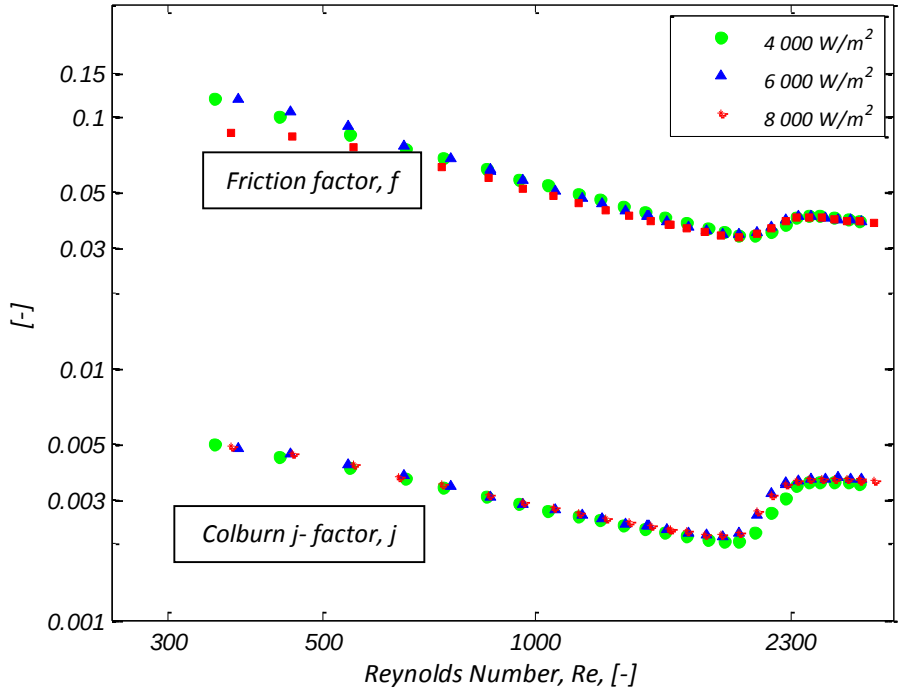

Figure 55 Comparison of 0.85 mm bellmouth inlet friction factor and Colburn *j*-factor results

The results of the 0.57 mm microchannel with the sudden contraction and bellmouth inlets are given in Figure 56 and Figure 57.

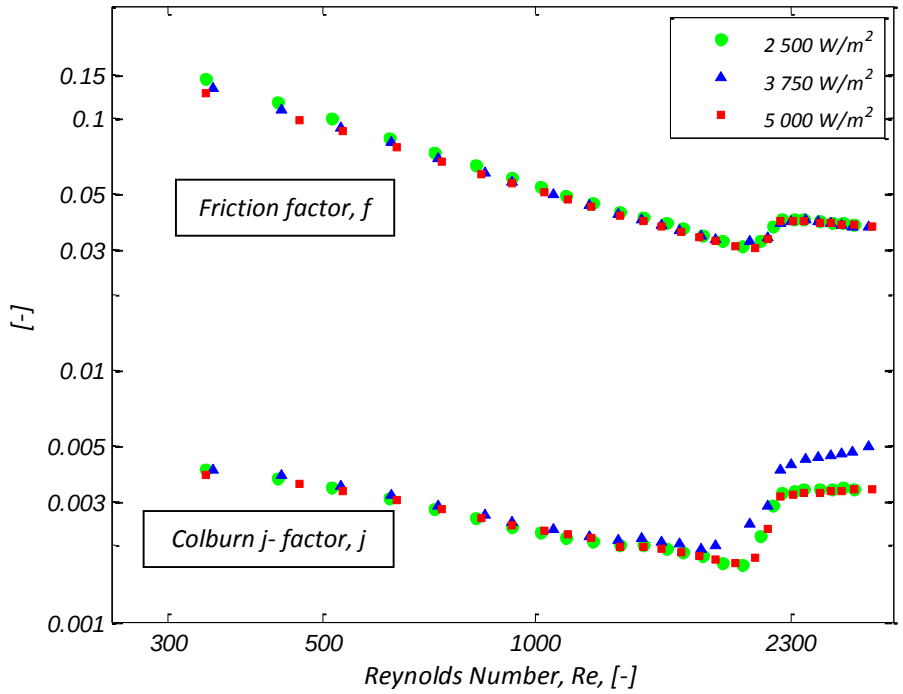

Figure 56 Comparison of 0.57 mm sudden contraction inlet friction factor and Colburn *j*-factor results

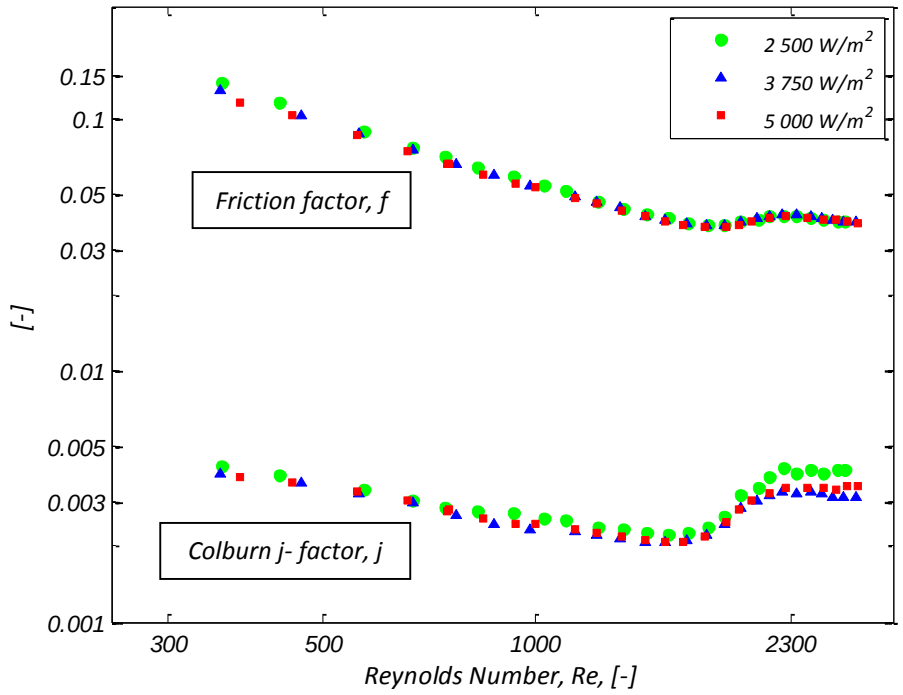

Figure 57 Comparison of 0.57 mm bellmouth inlet friction factor and Colburn *j*-factor results

Figure 58 plots the deviation of the relationship from the 1.05 mm test section results over the entire experimental range. Equation (21) underpredicts the low Reynolds number value results due to the low pressure drop measurements at Reynolds numbers below 500 and the inaccuracy of the mass flow meter reading at low flow rates. As noted in Chapter 4.3, friction factor results were found to be higher for higher heat fluxes. Looking at the trends of Figure 58, the higher heat flux results deviation values' are found to show a similar relationship, with Equation (21) therefore overpredicting more of the results. The relationship showed good agreement with the measured friction factors up till a Reynolds number of 2 400, where a few of the results started to dip slightly below the -10% marker. This is due to the very small wall to bulk fluid temperature difference, which dominates the turbulent Nusselt number, underpredicting the turbulent regime results. Due to the relatively high pressure transducer uncertainty at the low values of Reynolds number, there was less agreement of the relationship with the results below a Reynolds number of 500.

Figure 59 to Figure 61 plot the remainder of the predicted deviation from the measured results. The results indicated a good agreement with the 1.05 mm bellmouth test data, with relationship under-predicting the swirl inlet results by 5% to 15%. The 0.85 mm experimental measurements showed good agreement for predictions above a Reynolds number of 750. This was due to the high relative uncertainty of the pressure drop measurements at the low flow rates experienced in the 0.85 mm test section. The 0.57 mm results also showed underprediction using the relationship. Low mass flow rate measurement accuracy associated with the 0.57 mm test section experimentation was determined as the cause of the underprediction of the results. It must be noted that equation (21) was formed using the 1.05 mm test section data, and its applicability to the other test sections may require the manipulation of the constants used in the equation. Rather basing equation (21) on the full data set may allow for better prediction of the 0.85 mm and 0.57 mm results, but at the cost of a less accurate prediction of the 1.05 mm test section results.

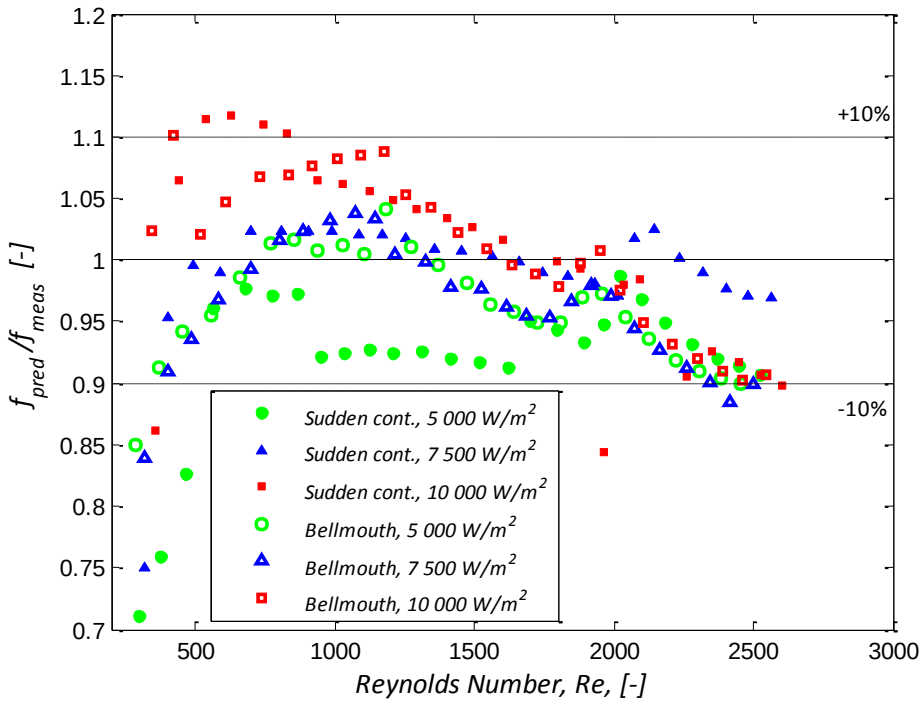

Figure 58 Deviation of the *j*-factor relationship to the measured friction factor results for the 1.05 mm microchannel with the sudden contraction and bellmouth inlets

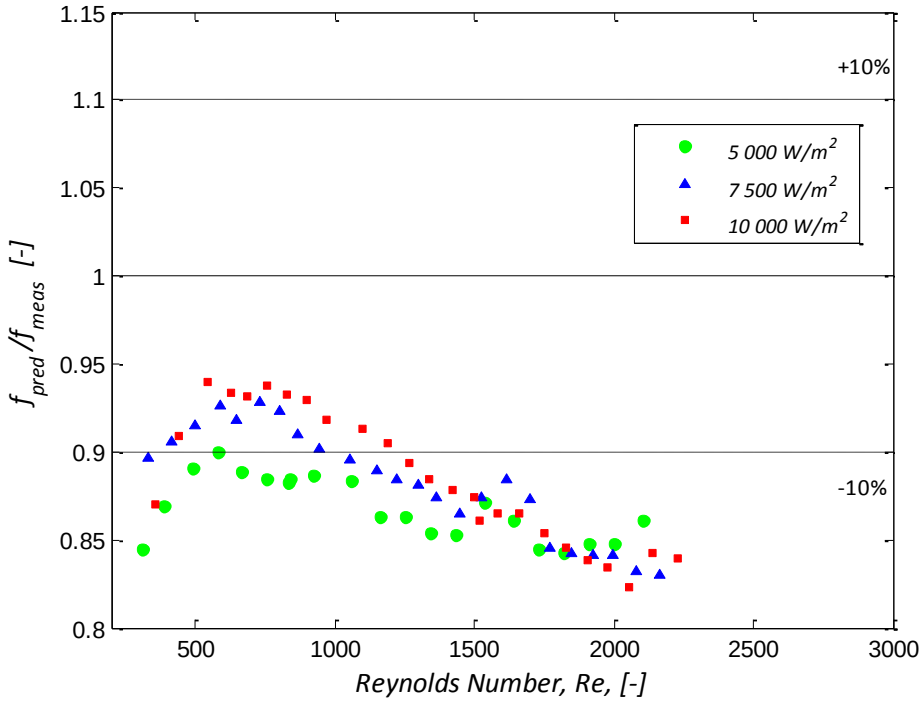

Figure 59 Deviation of the *j*-factor relationship to the measured friction factor results for the 1.05 mm microchannel with the swirl inlet

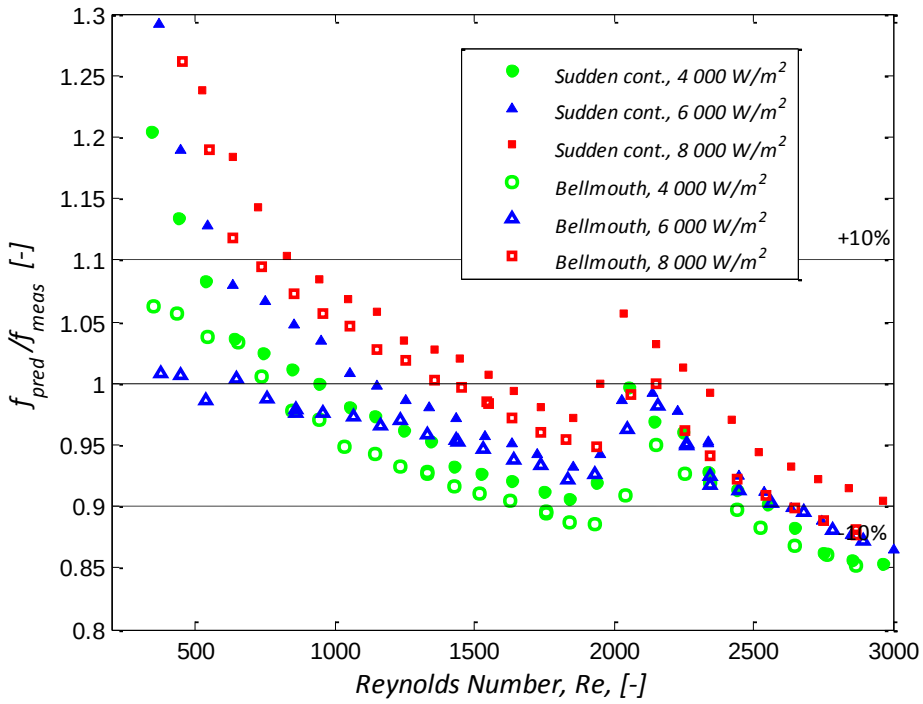

Figure 60 Deviation of the *j*-factor relationship to the measured friction factor results for the 0.85 mm microchannel with the sudden contraction and bellmouth inlets

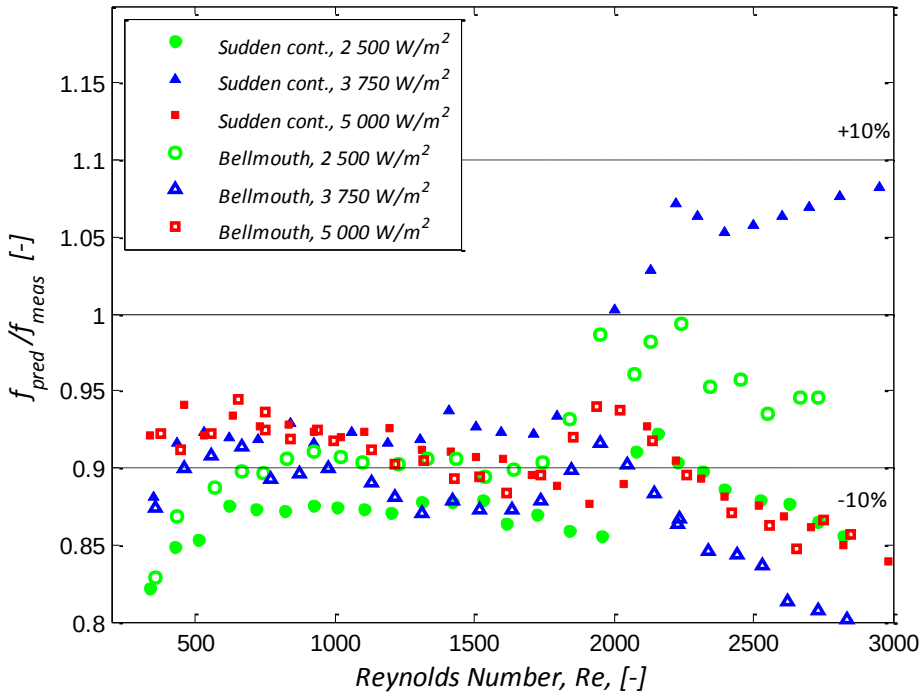

Figure 61 Deviation of the *j*-factor relationship to the measured friction factor results for the 0.57 mm microchannel with the sudden contraction and bellmouth inlets

The results show consistency with the 1.05 mm and 0.85 mm outcomes, with very good agreement of the relationship with the measured friction factor. The comparison of the relationship with the measured results is given from Figure 58 to Figure 61. The 1.05 mm and 0.85 mm test section results were predicted well for the sudden contraction and bellmouth inlets, while the 1.05 mm swirl inlet experiments were underpredicted by the relationship. The 0.57 mm test section results showed scattered agreement, with the majority of predictions falling at around 10% below the measured values.

Similar comparisons were done for the prediction of the measured Nusselt number using equation (22). The deviation of the results for the different test sections and their respective inlet conditions is given from Figure 62 to Figure 65. The results showed that the predictive model had good agreement with the 1.05 mm sudden contraction and bellmouth inlet data. This is due to the relationship being based on this data. The relationship overpredicts the results of the 1.05 mm swirl inlet. There is good data prediction for the 0.85 mm microchannel data for both the sudden contraction and bellmouth data, while most of the 0.57 mm results are overpredicted by 30% to 40%. The reasons for the deviations are the same for those made for the friction factor result deviation associated with equation (21). Where improvement is concerned, manipulation of the equation constants by using the entire data set can provide better case-specific results.

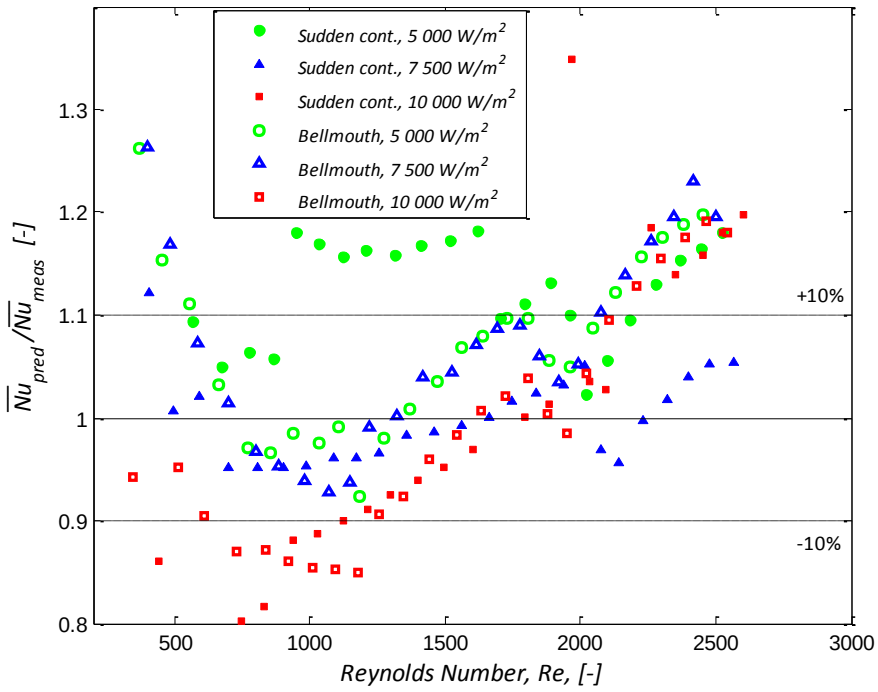

Figure 62 Deviation of the *j*-factor relationship to the measured Nusselt number results for the 1.05 mm microchannel with the sudden contraction and bellmouth inlets

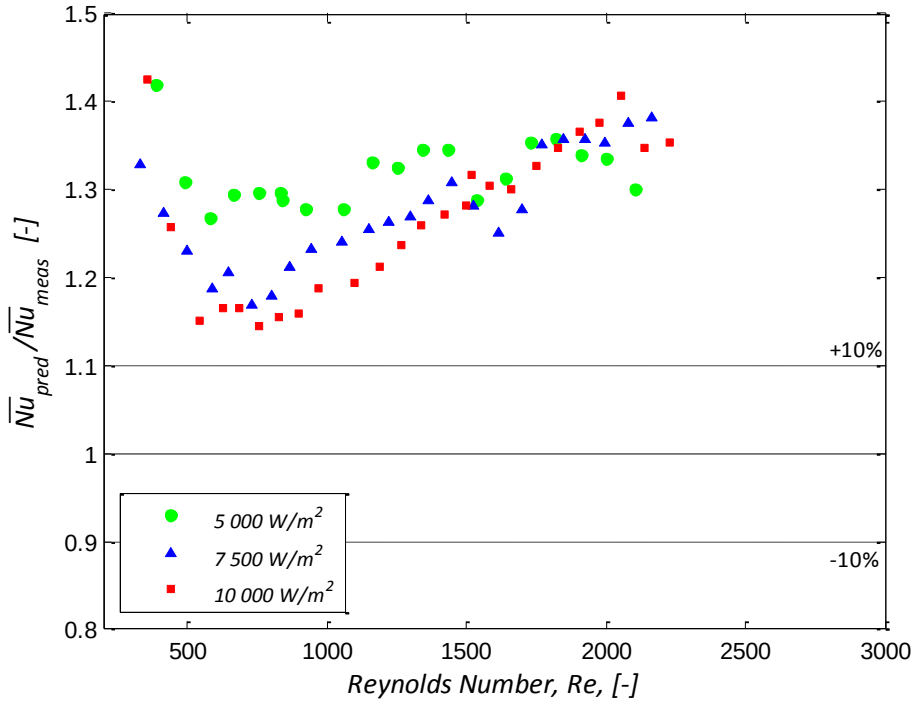

Figure 63 Deviation of the *j*-factor relationship to the measured Nusselt number results for the 1.05 mm microchannel with the swirl inlet

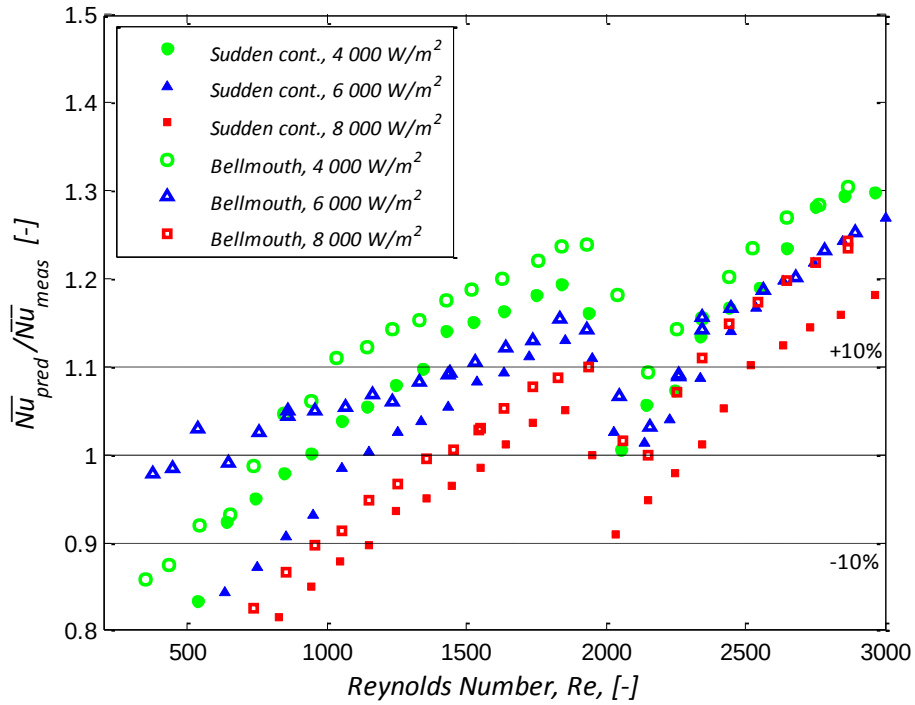

Figure 64 Deviation of the *j*-factor relationship to the measured Nusselt number results for the 0.85 mm microchannel with the sudden contraction and bellmouth inlets

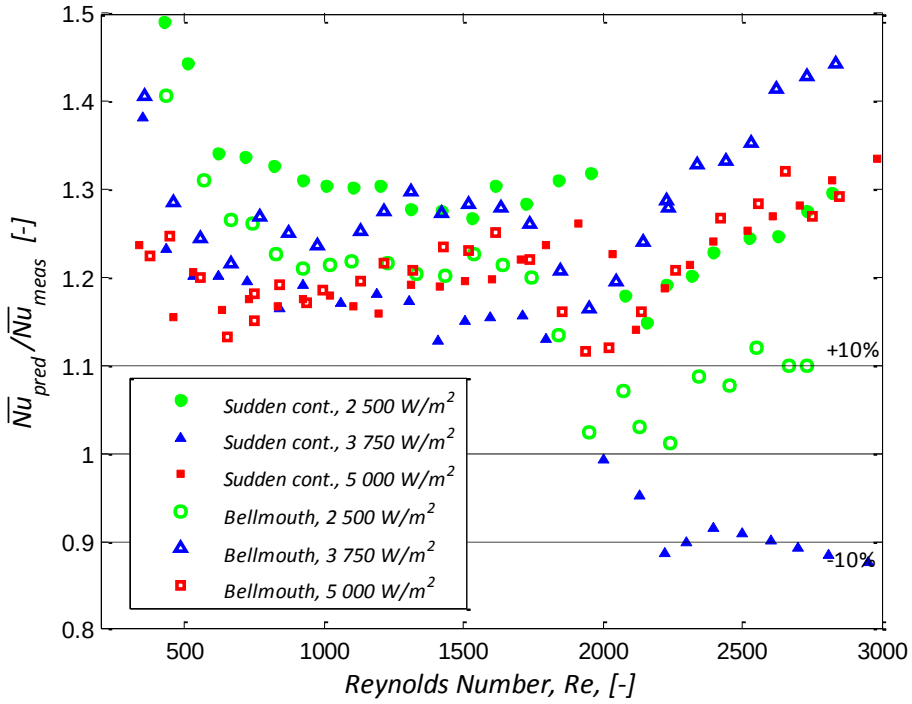

Figure 65 Deviation of the *j*-factor relationship to the measured Nusselt number results for the 0.57 mm microchannel with the sudden contraction and bellmouth inlets

The results of the relationship, equation (21), were compared to the measurement results directly. The results for the friction factor comparison are given from Figure 66 to Figure 68.

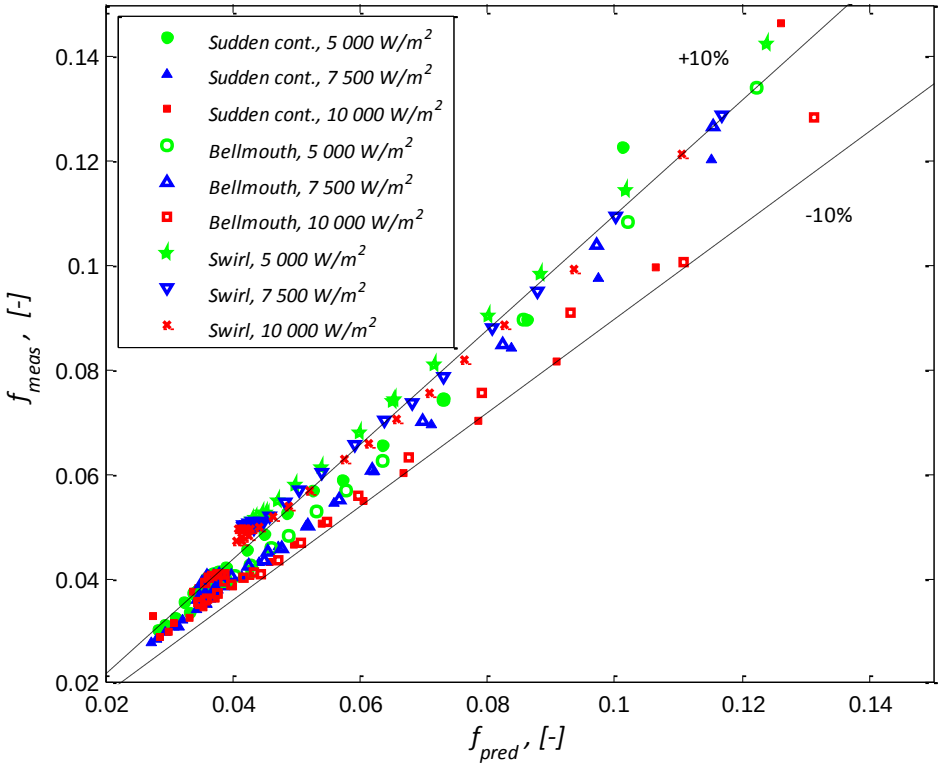

Figure 66 Comparison of the predicted and measured friction factors for 1.05 mm test section

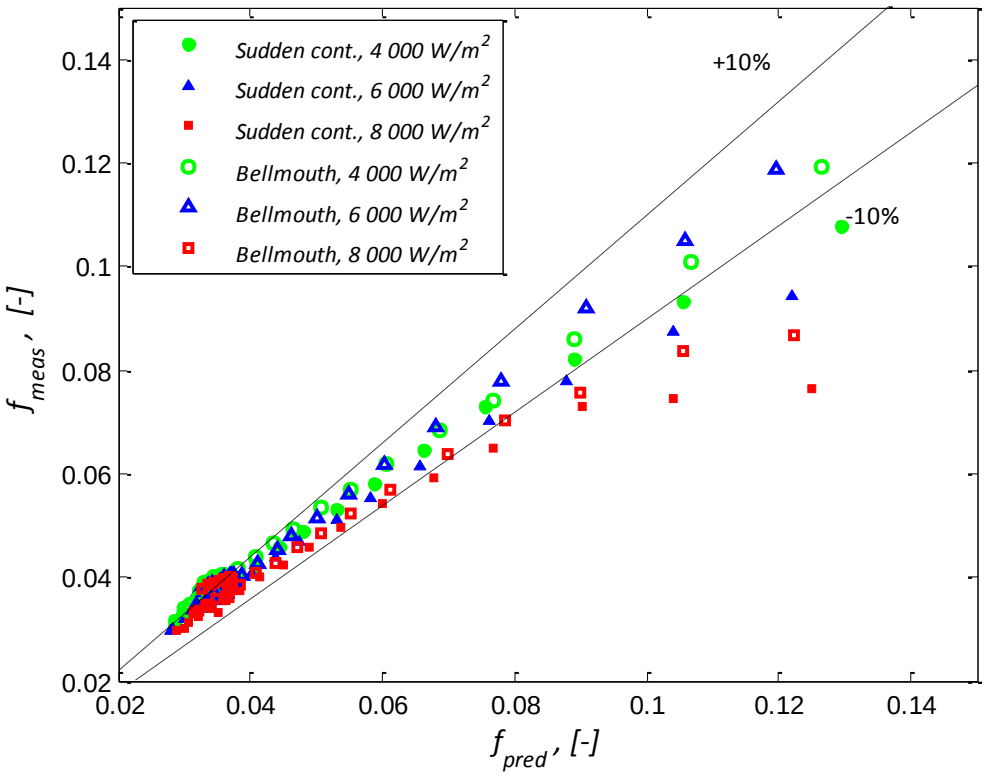

Figure 67 Comparison of the predicted and measured friction factors for 0.85 mm test section

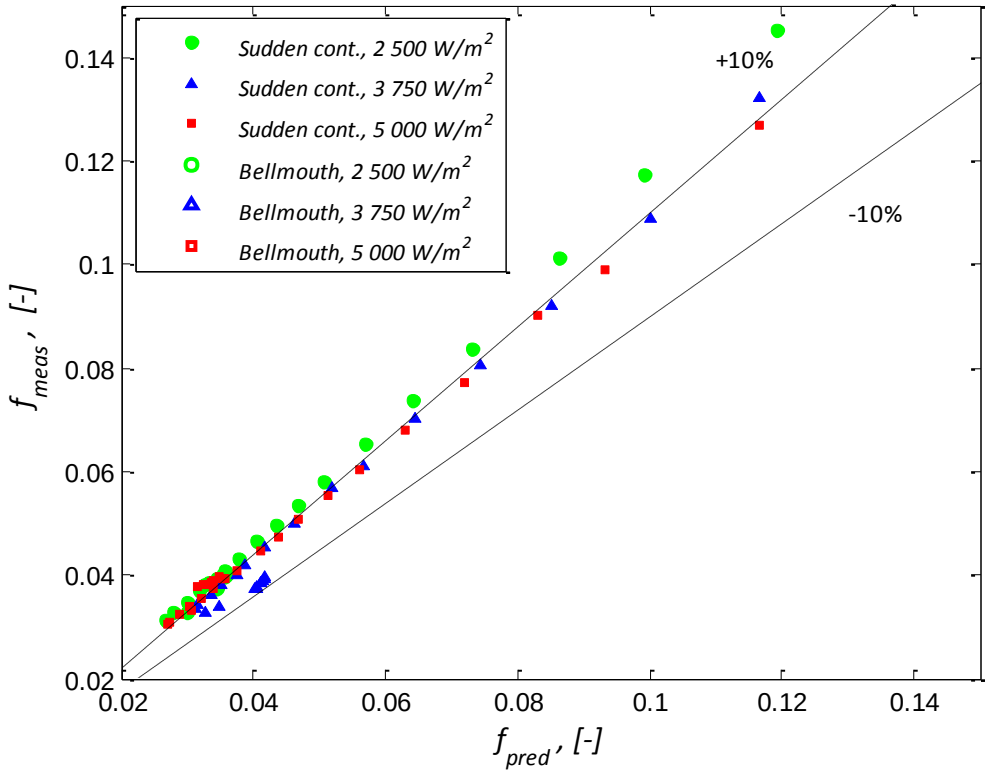

Figure 68 Comparison of the predicted and measured friction factors for 0.57 mm test section

The friction factor results show good agreement with the relationship. The Nusselt number results were also compared to the relationship given by equation (22). The direct comparison, given from Figure 69 to Figure 71 shows the accuracy of the relationship when compared to the measured the results.

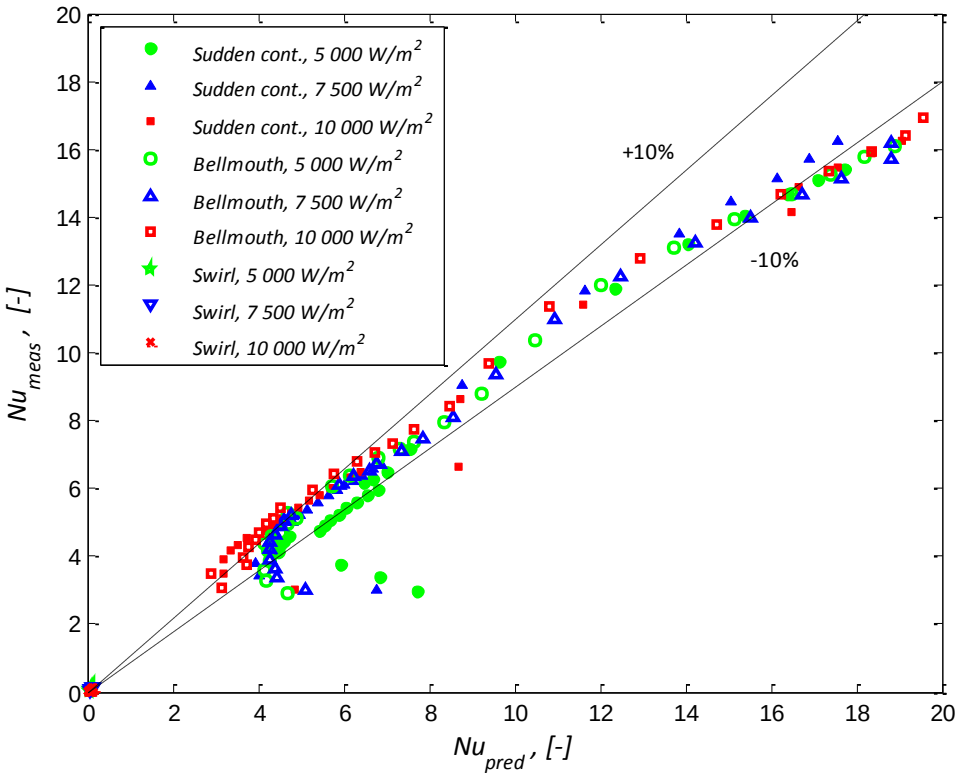

Figure 69 Comparison of the predicted and measured Nusselt numbers 1.05 mm test section

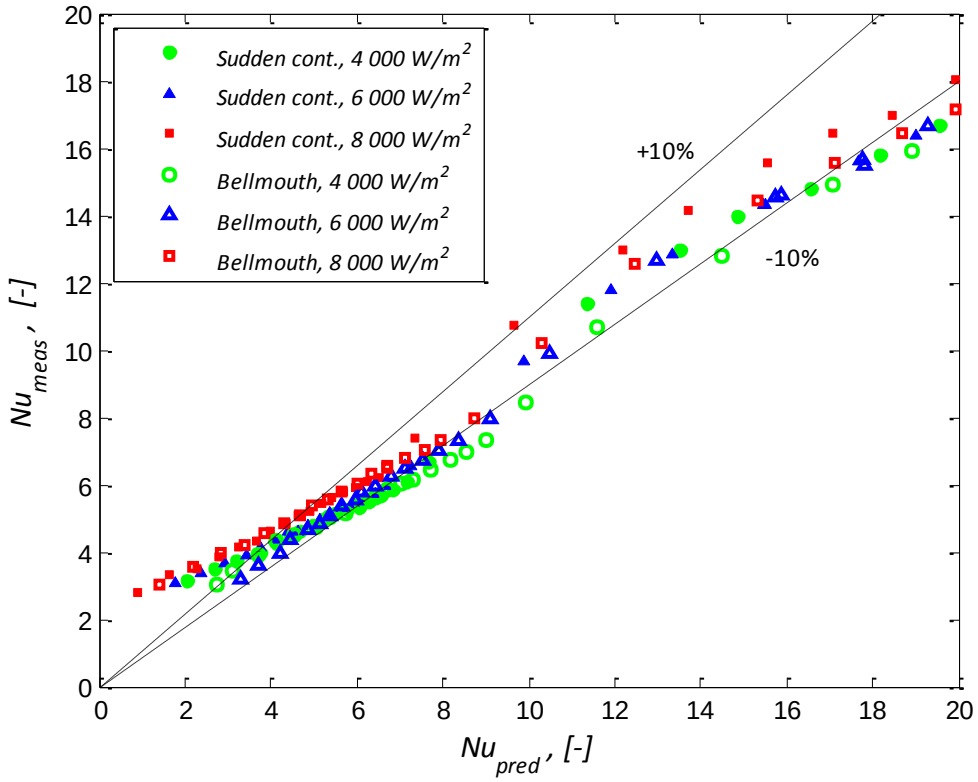

Figure 70 Comparison of the predicted and measured Nusselt numbers 0.85 mm test section

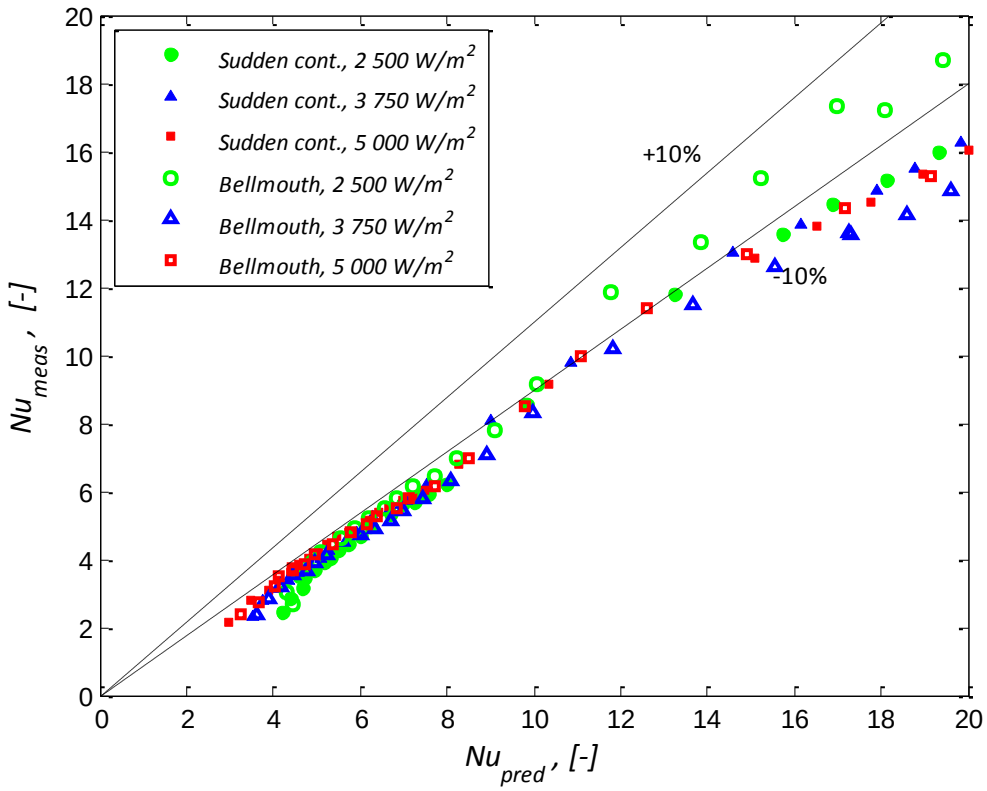

Figure 71 Comparison of the predicted and measured Nusselt numbers 0.57 mm test section

5.5 Summary of result analysis and comparison

The friction factor, Nusselt number and Colburn *j*-factor results for each of the test sections were compared with each other. The results show the effect that inlet conditions have on microchannel flow. Significant friction factor increases were noticed in the transition regime for both the sudden contraction and bellmouth inlet sections. The swirl inlet condition yielded the highest friction factor increases. Similarly, the heat transfer rate, represented by the Nusselt number, increased with the addition of the bellmouth and swirl inlets over the sudden contraction inlet. The results show that there is significant improvement in the heat transfer rate in conjunction with a rise in friction factor. Comparing the two results in the transition regime, an inlet condition such as the bellmouth has a higher increase of the heat transfer rate than of the friction factor. This has a positive impact on heat transfer applications, where the effects of inlet conditions can play a major role.

The results of the friction factor were compared with the *j*-factor, and a relationship between the two parameters was determined. The relationship provides a means of calculating the friction factor

using the Nusselt number (or effectively, the heat transfer coefficient) and vice versa. The results of the prediction show good agreement with the 1.05 mm and 0.85 mm microchannel sudden contraction and bellmouth results, but diverge from the 0.57 mm results and the 1.05 mm swirl inlet results. The relationship should be further investigated for the effect of inlet conditions, which, as shown, has a large influence on the accuracy of the relationship to the results.

6 Summary, conclusions and future work

6.1 Summary

The purpose of this study was to experimentally determine the effect of inlet conditions on the friction factor and heat transfer characteristics associated with microchannels. Past and recent studies have placed emphasis on the deviation of results due to unconsidered entry conditions to the test section. Literature was explored in the field on single-phase laminar flow in microchannels to determine the necessary outcomes for the study.

A test facility was designed, built and commissioned in order to achieve the outcomes, along with three copper test sections of different hydraulic diameters. Each test section consisted of a single rectangular channel milled away from the material. The resulting hydraulic diameters were measured to be 1.05 mm, 0.85 mm and 0.57 mm. Each test section consisted of slots for thermocouples to measure near-wall temperatures of the microchannel. Three inlet conditions were manufactured for experimental purposes. These were the sudden contraction inlet, the bellmouth inlet, and the swirl inlet. The sudden contraction and bellmouth inlet were investigated with all three test sections, while the swirl was only investigated with the 1.05 mm test section. In-channel pressure ports were placed in the microchannel to measure the pressure drop along the length of the channel, while inlet and outlet thermocouples were placed before and after the test section respectively to determine the heat transferred to the fluid water.

Experimental work consisted of measuring the friction factors and Nusselt numbers associated with both the laminar and transitional flow regimes. Three constant surface heat flux boundary conditions were applied to each test section. The power was supplied to a heater element located at the bottom of the channel material only. An energy balance was used to determine steady-state conditions prior to the logging of measurements. Thermocouples and pressure transducers were calibrated in the laboratory, while the mass flow meter was accurately pre-calibrated.

Experimental work consisted of measuring temperatures, differential pressures and mass flow rates for the different test scenarios. The data was analysed to determine the friction factor of the channel and the heat transfer rate, represented in this study by the Nusselt number. Comparison of these results with the conventional theory used in macrochannel design was done. The results of the inlet sections for each test section were then approached. Comparisons of the inlets were done, and

the effect of inlet conditions on pressure drop and heat transfer was determined. Further data processing resulted in the formation of a relationship between the Colburn *j*-factor (related to the Nusselt number) and the friction factor. This relationship was adapted to each test scenario to determine its accuracy among various test sections and inlet conditions.

The effect of inlet conditions in single-phase laminar and transitional flow of water in rectangular microchannels was experimentally investigated for a constant surface heat flux boundary condition. Results were compared with the theory used for the design of macrochannel systems.

6.2 Conclusions

Adiabatic friction factor results were determined initially and it was found that the results showed very good agreement with the Shah and London correlation in the laminar regime. The critical Reynolds number occurred between 1 800 and 2 000, showing good agreement with the conventional theory used for macrochannel theory. The addition of the bellmouth inlet resulted in an enhanced transition regime, with increased friction factors, an early onset of transition and a smoother transition profile than that of the sudden contraction inlet.

The diabatic friction factor results show a lower than predicted value than that of the Shah and London correlation for all three test sections and inlet conditions. Sudden contraction results showed good agreement with the traditional critical Reynolds number value, with transition commencing at a Reynolds number of 1 950 and ending at a Reynolds number of 2 300. The bellmouth inlet condition results showed a divergence from the laminar theory at a Reynolds number of approximately 1 500 and reached turbulence at a Reynolds number to 2 300. There was a sudden rise in the friction factor results in the laminar regime at a Reynolds number of 1 300, where the friction factors suddenly shifted to a higher value but remained in the laminar regime. There was also a decrease in friction factor with an increase in heat input with the sudden contraction inlet condition.

The swirl inlet condition measured higher friction factors than its sudden contraction and bellmouth counterparts. The transition regime began at a Reynolds number of 1 500 and ended at 1 700. The flow then entered a turbulent swirl regime with much higher friction factors than the other inlet conditions.

The Blasius equation overpredicted the results for the sudden contraction and bellmouth inlet conditions for all three test sections in the turbulent regime by approximately 14%. The consistency among the test sections with respect to the critical Reynolds number and the conformity of the friction factors show no significant deviation from conventional theory for pressure drop prediction.

The average Nusselt number results were affected by the axial conduction effect in the laminar regime. This effect reduced values of Nusselt number below a Reynolds number of 1 000, resulting in a lower measured convective heat transfer coefficient. The laminar regime Nusselt number did not converge into a single value as the theory predicted due to the flow not being fully hydrodynamically and thermally developed. This resulted in a constantly increasing value of Nusselt number in the laminar regime until transition began. The results of the sudden contraction inlet condition showed good agreement in the turbulent regime with the Gnielinski equation. There are very few logged points in the transition regime due to its rapid development and high pressure drop values. The bellmouth results showed an increasing trend in Nusselt numbers in the laminar regime, with a sudden rise occurring at a Reynolds number of 1 300, similar to the friction factor results. The flow then entered the transition regime, which lasted much longer than the sudden contraction transition regime. The Nusselt number converged into the Gnielinski equation in the turbulent regime for the bellmouth inlet results. Research into the effects of the bellmouth inlet could not be validated by comparing it with the work of Olivier and Meyer [40], and Tam and Ghajar [39].

The swirl inlet results showed a higher Nusselt number throughout the experimental range. The Nusselt numbers rose with a steeper gradient in the laminar regime compared with the other inlet conditions, while the turbulent regime values showed a much higher value at much lower Reynolds numbers. The increased friction factor and Nusselt number values for the bellmouth inlet and swirl inlet over the sudden contraction inlet are compared below in Table 17. The results showed that though the inlet condition increases the friction factor in the channel significantly, there is a positive trade-off with a higher improvement in the heat transfer. This heat transfer enhancement in the transitional regime shows great potential in heat transfer applications for microchannels.

Hydraulic diameter	*Inlet*	*Friction factor increase*	*Nusselt number enhancement*	*Regime*
1.05 mm	Bellmouth	5% - 30%	10% - 70%	Transition
	Swirl	15% - 72%	15% - 120%	All
0.85 mm	Bellmouth	7% - 15%	10% - 20%	All
0.57 mm	Bellmouth	5% - 30%	10% - 66%	Transition

Table 17 Friction factor and Nusselt number increase over the sudden contraction inlet section due to the attachment of the bellmouth and swirl inlet sections

The comparison shows a large difference in the effects of the inlet condition on both the pressure drop and heat transfer. Given that the studies are in two different categories of flow, the applicability of direct comparison is in question. For this reason, improving on the bellmouth result database for microchannels is necessary.

The results of the Nusselt number were represented in terms of the Colburn *j*-factor to compare it with the friction factor. This representation not only shows the effect of the inlet conditions, but can also be related directly to the friction factor. A relationship was observed between the *j*-factor and the friction factor in order to provide a means of calculation of the friction factor by using temperature and flow rate measurements only. The relationship can be manipulated to calculate the Nusselt number, and effectively the heat transfer coefficient, from flow rate and pressure drop measurements.

6.3 Future work

Future work is required to improve on the current database of results. It is therefore recommended to focus on the following aspects in future related work:

- The effect of the axial heat conduction should be considered for low flow rate experimentation. By reducing/removing this effect, a better trend of the laminar regime Nusselt number can be made, and the effect of the developing length can be considered in the development of a Nusselt number correlation for microchannel flow of water in hydrodynamic developing flow.
- The bellmouth inlet condition affects the flow in the transition regime, leading to an early onset of transition. This effect should be studied further to determine the best contraction ratio and profile shape to yield a higher heat transfer rate for a lower pressure drop.
- Testing of different channel materials will improve the current study's database. By manufacturing test sections of similar dimensions, and using the same inlet conditions, the current study can be extended to determine the effect of the channel material on both the heat transfer and pressure drop.
- A reduction in the friction factor was noticed when the heat input was increased. This effect was noticed for all the experimental scenarios, but was more prominent with the 1.05 mm and 0.85 mm test sections. The effect of an increasing heat input should be investigated to determine its effect on the friction factor.

7 References

[1] D. Tuckerman and F. Pease, “High-performance heat sinking for VLSI,” *IEEE Electron Device Letters,* Vols. EDL-2, no. 5, pp. 126-129, 1981.

[2] X. Peng and G. Peterson, “Convective heat transfer and flow friction for water flow in microchannel structures,” *International Journal of Heat and Mass Transfer,* vol. 39, no. 12, pp. 2599-2608, 1996.

[3] G. Mala and D. Li, “Flow characteristics of water in microtubes,” *International Journal of Heat and Fluid Flow,* vol. 20, pp. 142-148, 1999.

[4] Q. Weilin, G. Mala and L. Dongqing, “Pressure-driven water flows in trapezoidal silicon microchannels,” *International Journal of Heat and Mass Transfer,* vol. 43, pp. 353-364, 2000.

[5] T. Harms, M. Kazmierczak and F. Gerner, “Developing convective heat transfer in deep rectangular microchannels,” *International Journal of Heat and Fluid Flow,* vol. 20, pp. 149-157, 1999.

[6] J. Judy, D. Maynes and B. Webb, “Characterization of frictional pressure drop for liquid flows through microchannels,” *International Journal of Heat and Mass Transfer,* vol. 45, pp. 3477-3489, 2002.

[7] H. Hegab, A. Bari and T. Ameel, “Friction and convection studies of R-134a in microchannels within the transition and turbulent flow regimes,” *Journal of Experimental Heat Transfer,* vol. 15, pp. 245-259, 2002.

[8] G. Celata, M. Cumo and G. Zummo, “Thermal-hydraulic characterisatics of single-phase flow in capillary tubes,” *Experimental Thermal and Fluid Science,* vol. 28, pp. 87-95, 2004.

[9] S. Garimella and V. Singhal, “Single-phase flow and heat transport and pumping considerations in microchannel heat sinks,” *Heat Transfer Engineering,* vol. 25, no. 1, pp. 15-25, 2004.

[10] P. Hao, F. He and K. Zhu, “Flow characteristics in a trapezoidal silicon microchannel,” *Journal of Micromechanics and Microengineering,* vol. 15, pp. 1362-1368, 2005.

[11] M. Steinke and S. Kandlikar, “Single-phase liquid friction factors in microchannels,” *International Journal of Thermal Sciences,* vol. 45, pp. 1073-1083, 2006.

[12] P. Hrnjak and X. Tu, “Single-phase pressure drop in microchannels,” *International Journal of Heat and Fluid Flow,* vol. 28, pp. 2-14, 2007.

[13] V. Natrajan and K. Christensen, “Non-intrusive measurements of convective heat transfer in smooth- and rough-wall microchannels: laminar flow,” *Journal of Experimental Fluids,* 2010.

[14] G. Morini, M. Lorenzini, S. Salvigni and G. Celata, “Experimental analysis of microconvective heat transfer in the laminar and transitional regions,” *Experimental Heat Transfer,* vol. 23, no. 1, pp. 73-93, 2010.

[15] E. Sieder and G. Tate, “Heat transfer and pressure drop of liquids in tubes,” *Industrial Engineering Chemistry,* vol. 28, pp. 1429-1435, 1936.

[16] Z. Li, Y. He, G. Tang and W. Tao, “Experimental and numerical studies of liquid flow and heat transfer in microtubes,” *International Journal of Heat and Mass Transfer,* vol. 50, pp. 3447-3460, 2007.

[17] H. Park and J. Punch, “Friction factor and heat transfer in multiple microchannels with uniform flow distribution,” *International Journal of Heat and Mass Transfer,* vol. 51, pp. 4535-4543, 2008.

[18] J. Jiang, Y. Hao and M. Shi, “Fluid flow and heat transfer characteristics in rectangular microchannels,” *Heat Transfer - Asian Research,* vol. 37, no. 4, pp. 197-207, 2008.

[19] G. Gamrat, M. Favre-Marinet and D. Asendrych, “Conduction and entrance effects on laminar liquid flow and heat transfer in rectangular microchannels,” *International Journal of Heat and Mass Transfer,* vol. 48, pp. 2943-2954, 2005.

[20] G. Morini, “Single-phase convective heat transfer in microchannels: a review of experimental work,” *International Journal of Thermal Sciences,* vol. 43, pp. 631-651, 2004.

[21] X. Jiang, Z. Zhou, X. Huang and C. Liu, “Laminar flow through microchannels used for microscale cooling systems,” in *IEEE/CPMT Electronic Packaging Technology Conference*, 1997.

[22] B. Xu, K. Ooi, N. Wong and W. Choi, “Experimental investigation of flow friction for liquid flow in microchannels,” *International Communications in Heat and Mass Transfer,* vol. 27, no. 8, pp. 1165-1176, 2000.

[23] H. Wu and P. Cheng, “An experimental study of convective heat transfer in silicon microchannels with different surface conditions,” *International Journal of Heat and Mass Transfer,* vol. 46, pp. 2547-2556, 2003.

[24] D. Lelea, S. Nishio and K. Takano, “The experimental research on microtube heat transfer and fluid flow of distilled water,” *International Journal of Heat and Mass Transfer,* vol. 47, pp. 2817-2830, 2004.

[25] Y. Chen, S. Kang, W. Tuh and T. Hsiao, “Experimental investigation of fluid flow and heat transfer in microchannels,” *Tamakang Journal of Science and Engineering,* vol. 7, no. 1, pp. 11-16, 2004.

[26] W. Owhaib and B. Palm, “Experimental investigation of single-phase convective heat transfer in circular microchannels,” *Experimental Thermal and Fluid Sciences,* vol. 28, pp. 105-110, 2004.

[27] H. Zhang, D. Pinjala, T. Wong, K. Toh and Y. Joshi, “Single-phase liquid cooled microchannel heat sink for electronic packages,” *Applied Thermal Engineering,* vol. 25, pp. 1472-1487, 2005.

[28] M. Kang, J. Shin, H. Lee and K. Chun, “Analysis of laminar convective heat transfer in micro heat exchanger for stacked chip module,” *Microsystem Technologies,* vol. 11, pp. 1176-1186, 2005.

[29] E. Colgan, B. Furman, M. Gaynes, W. Graham, N. LaBianca, J. Magerlein, R. Polastre, M. Rothwell, R. Bezama, R. Choudhary, K. Marston, H. Troy, J. Wakil, J. Zitz and R. Schimdt, “A practical implementation of silicon microchannel coolers for high power chips,” in *21st IEEE SEMI-THERM Symposium*, 2005.

[30] D. Costaschuk, J. Elsnab, S. Peterson, J. Klewicki and T. Ameel, “Axial static pressure measurements of water flow in a rectangular microchannel,” *Experiments in Fluids,* vol. 43, pp. 907-916, 2007.

[31] Y. Mishan, A. Mosyak, E. Pogrebnyak and G. Hetsroni, “Effect of developing flow and thermal regime on momentum and heat transfer in micoscale heat transfer,” *International Journal of Heat and Mass transfer,* vol. 50, pp. 3100-3114, 2007.

[32] G. Gamrat, M. Favre-Marinet, S. Le Person, R. Baviere and F. Ayela, “An experimental study and modelling of roughness effects on laminar flow in microchannels,” *Journal of Fluid Mechanics,* vol. 594, pp. 399-423, 2008.

[33] J. Jung and H. Kwak, “Fluid flow and heat transfer in microchannels with rectangular cross section,” *Heat and Mass Transfer,* vol. 44, pp. 1041-1049, 2008.

[34] G. Wang, L. Hao and P. Cheng, “An experimental and numerical study of forced convection in a microchannel with negligible axial heat conduction,” *International Journal of Heat and Mass Transfer,* vol. 52, pp. 1070-1074, 2009.

[35] W. Wibel and P. Ehrhard, “Experiments on the laminar/turbulent transition of liquid flows in rectangular microchannels,” *Heat Transfer Engineering,* vol. 30, no. 1, pp. 70-77, 2009.

[36] S. Barlak, S. Yapici and O. Sara, “Experimental investigation of pressure drop and friction factor for water flow in microtubes,” *International Journal of Thermal Sciences,* vol. 50, no. 3, pp. 361 - 368, 2011.

[37] M. Moharana, G. Agarwal and S. Khandekar, “Axial conduction in single-phase simultaneously developing flow in a rectangular mini-channel array,” *International Journal of Thermal Sciences,* vol. 50, no. 6, pp. 1001-1012, 2011.

[38] G. Maranzana, I. Perry and D. Maillet, “Mini- and micro-channels: influence of axial conduction in the walls,” *International Journal of Heat and Mass Transfer,* vol. 47, pp. 3993 - 4004, 2004.

[39] L. Tam and A. Ghajar, “Effect of inlet geometry and heating on the fully developed friction factor in the transition regime of a horizontal tube,” *Experimental Thermal and Fluid Science,* vol. 15,

no. 1, pp. 52-64, 1997.

[40] J. Olivier and J. Meyer, “Single-phase heat transfer and pressure drop of the cooling of water inside smooth tubes for transitional flow with different inlet geometries (RP-1280),” *HVAC&R Research,* vol. 16, no. 4, pp. 471-496, 2010.

[41] T. Morel, “Comprehensive design of axisymmetric wind tunnel contractions,” *Journal of Fluids Engineering,* vol. 97, pp. 225-233, 1975.

[42] O. Aydin and M. Baki, “An experimental study on the design parameters of a counterflow vortex tube,” *Energy,* pp. 2763-2772, 2006.

[43] S. Kline and F. McClintock, “Describing uncertainties in single-sample experiments,” *Mechanical Engineering,* vol. 75, pp. 2-8, 1953.

[44] C. Popiel and J. Wojtkowiak, “Simple formulas for thermophysical properties of liquid water for heat transfer calculations (from 0°C to 150°C),” *Heat Transfer Engineering,* vol. 19, no. 3, pp. 87-101, 1998.

[45] R. Shah and A. London, Laminar flow forced convection in ducts, New York: Academic Press, 1978, pp. 196-222.

[46] Y. Céngel, “Chapter 8: Internal Forced Convection,” in *Heat Transfer: A Practical Approach 2nd Edition*, 2nd (SI) ed., New York, The McGraw-Hill Companies Inc., 2004, pp. 419-458.

[47] R. Moffat, “Describing the uncertainties in experimental results,” *Experimental Thermal and Fluid Science,* vol. 1, pp. 3-17, 1988.

Appendix A Calculation of the thermophysical properties of water for use in data analysis

Nomenclature

$c_{0,1,2,3,4}$	Coefficients of thermophysical properties of water as given in Table A.1	–
C_p	Specific heat	J/kgK
k	Thermal conductivity	W/m^2K
Pr	Prandtl number	–
T	Fluid temperature	K

Greek letters

ρ	Density	kg/m^3
μ	Dynamic viscosity	kg/ms

A.1 Introduction

It was required to accurately calculate the properties of water to determine the outcomes of the experiments. The water properties were calculated using the equations proposed by Popiel and Wojtkowiak [A.1]. The equations were developed for temperatures ranging between 0°C and 150°C. The properties required for the data analysis were the fluid density (ρ), dynamic viscosity (μ), specific heat (C_p), thermal conductivity (k) and Prandtl number (Pr). They proposed equations (A.1) to (A.5) to determine the fluid properties based on temperature only with coefficients c_0, c_1, c_2, c_3 and c_4 for each respective equation, given in Table A.1.

$$\rho = c_0 + c_1 T + c_2 T^2 + c_3 T^{2.5} + c_4 T^3 \quad \text{(A.1)}$$

$$C_p = c_0 + c_1 T + c_2 T^{1.5} + c_3 T^2 + c_4 T^{2.5} \quad \text{(A.2)}$$

$$k = c_0 + c_1 T + c_2 T^{1.5} + c_3 T^2 + c_4 T^{0.5} \quad \text{(A.3)}$$

$$\mu = \frac{1}{c_0 + c_1 T + c_2 T^2 + c_3 T^3} \quad \text{(A.4)}$$

$$Pr = \frac{1}{c_0 + c_1 T + c_2 T^2 + c_3 T^3} \quad \text{(A.5)}$$

Constants	$\boldsymbol{\rho}$	$\boldsymbol{C_p}$	$\boldsymbol{k}$	$\boldsymbol{\mu}$	$\boldsymbol{Pr}$
$\boldsymbol{c_0}$	999.79684	4.2174356	0.5650285	557.82468	0.074763403
$\boldsymbol{c_1}$	0.068317355	-0.0056181625	0.0026363895	19.408782	0.002902098
$\boldsymbol{c_2}$	-0.010740248	0.001299253	-0.00012516934	0.1360459	2.8606181E-05
$\boldsymbol{c_3}$	8.21409E-04	-1.15354E-04	-1.5154915E-06	-3.1160832E-04	-8.1395537E-08
$\boldsymbol{c_4}$	-2.3031E-05	4.15E-06	-0.000941295	-	-

Table A.1 List of coefficients for equations A.1 to A.5

The water properties were calculated using the bulk fluid temperature measurement. Graphical representations of these equations are given in Appendix A.2 for a temperature range of 0°C to 100°C. Each equation had its own associated uncertainty, and can be found in Appendix D.

A.2 Graphs of water properties

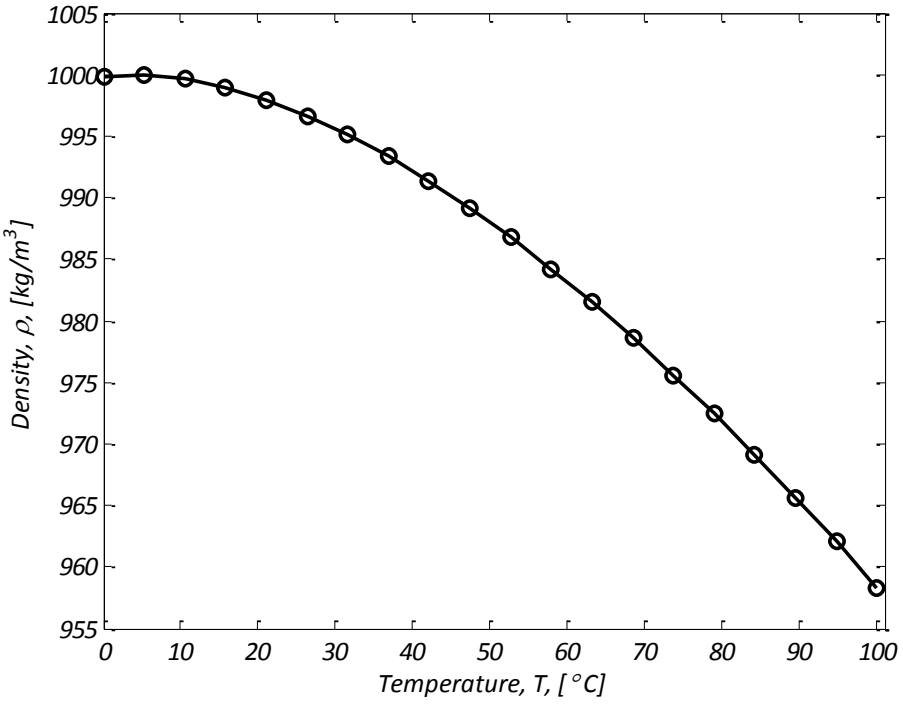

Figure A.1 Liquid water density variation from 0°C to 100°C using equation A.1

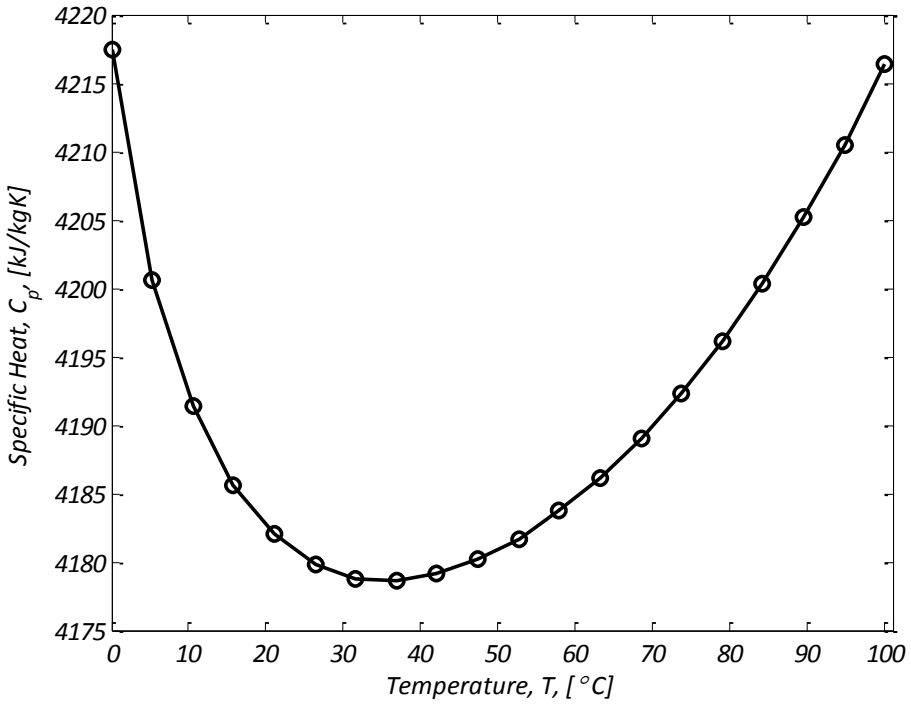

Figure A.2 Liquid water specific heat variation from 0°C to 100°C using equation A.2

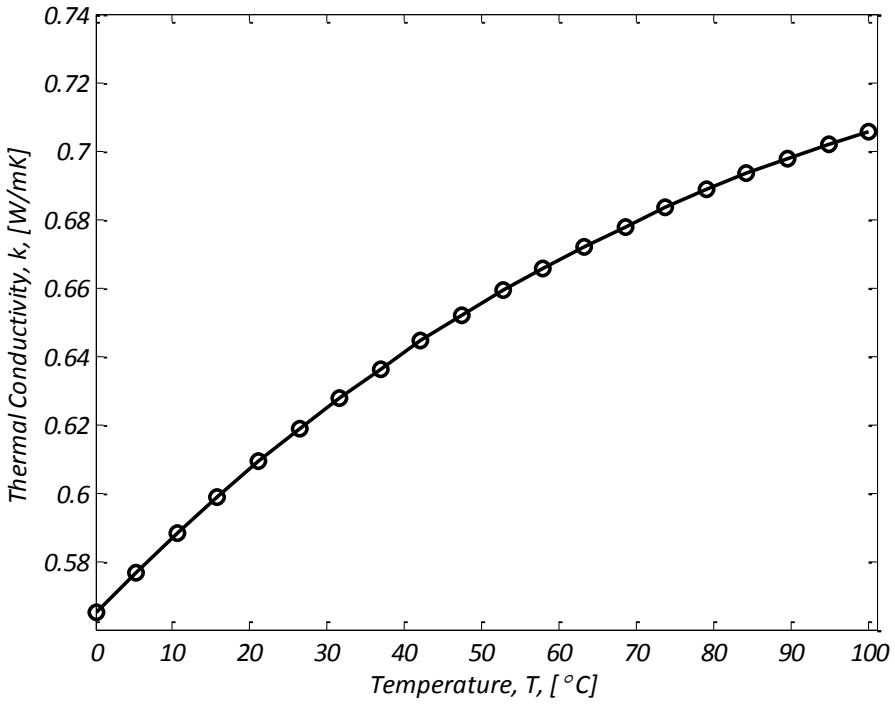

Figure A.3 Liquid water thermal conductivity variation from 0°C to 100°C using equation A.3

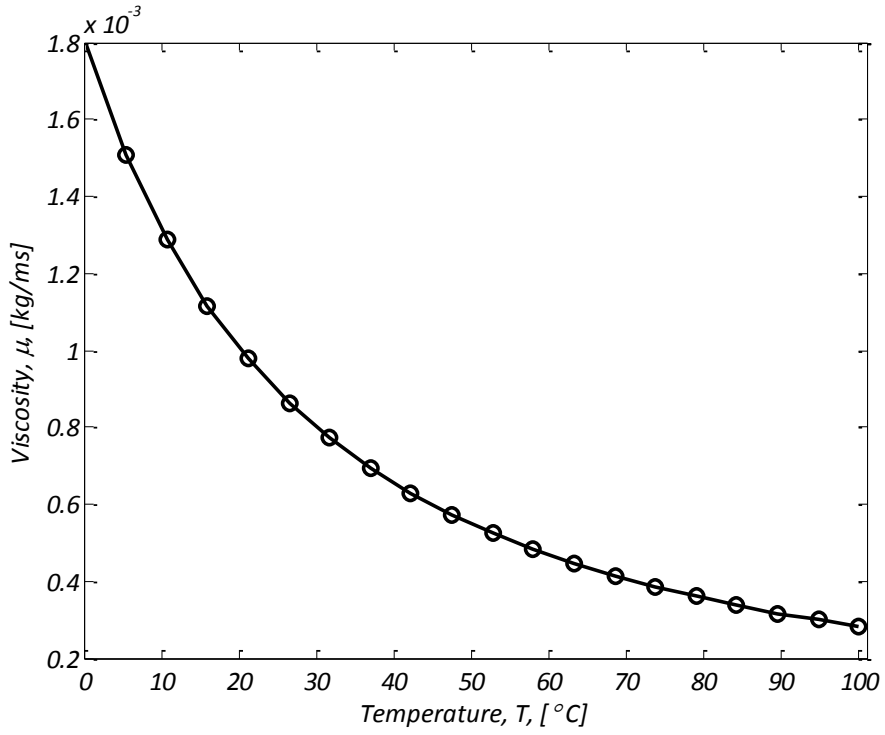

Figure A.4 Liquid water viscosity variation from 0°C to 100°C using equation A.4

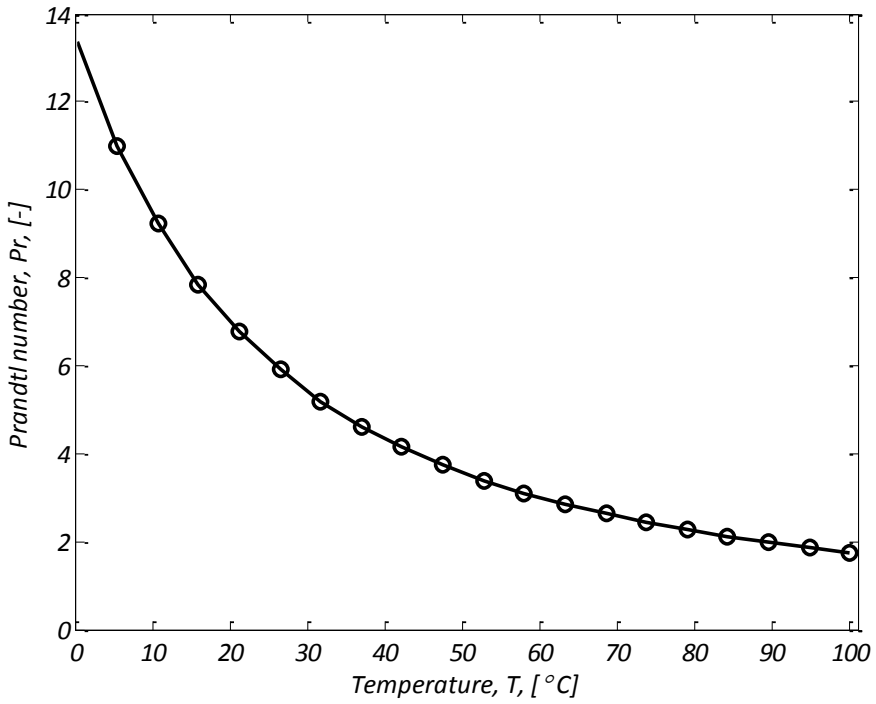

Figure A.5 Liquid water Prandtl number variation from 0°C to 100°C using equation A.5

A.3 References

[A.1] C. Popiel and J. Wojtkowiak, "Simple formulas for thermophysical properties of liquid," *Heat Transfer Engineering,* vol. 19, no. 3, pp. 87-101, 1998.

Appendix B Calibration of thermocouples

Nomenclature

c	Linear regression constant	℃
m	Linear regression gradient	–
T_{cal}	Exact thermocouple temperature	℃
T_{PT100}	PT100 temperature measurement	℃
$T_{thermocouple}$	Uncalibrated thermocouple measurement	℃

B.1 Introduction

Temperature measurements were taken using T-type thermocouples. The wall thermocouples used a smaller gauge #40 wire diameters to measure the microchannel wall temperature, while the inlet, outlet, insulation and ambient thermocouples used were the larger gauge #30. Four inlet and four outlet thermocouples were used to determine more accurate average temperatures, while eight wall thermocouples were placed along the side walls of the microchannel (four on each side, evenly spaced) to determine an average wall temperature. Insulation thermocouples were placed around the periphery of the first layer of insulation.

The inlet, outlet, insulation, ambient and heater element thermocouples were reused for the test sections. Inlet and outlet thermocouples were recalibrated, while the insulation, ambient and heater element thermocouples retained their first calibration coefficients. New wall thermocouples were used for each experiment. The inlet, outlet and wall thermocouples were calibrated together for each experiment.

B.2 Calibration procedure

The thermocouples were calibrated against a PT100 resistance temperature detector. The PT100 was purchased from *Wika Instruments* and came with a calibration certificate to quantify its accuracy. Thermocouple junctions were made either by soldering or welding. The smaller wall thermocouples were welded together as the soldering method did not fuse them adequately. The welding process resulted in smaller junctions, providing a better wall temperature measurement of the microchannel.

The thermocouples were secured to the PT100 and placed in the insulated chamber (see Figure B.1). The tips of the thermocouples were placed around the periphery of the PT100 tip to ensure that the probe and thermocouples measured the same temperature.

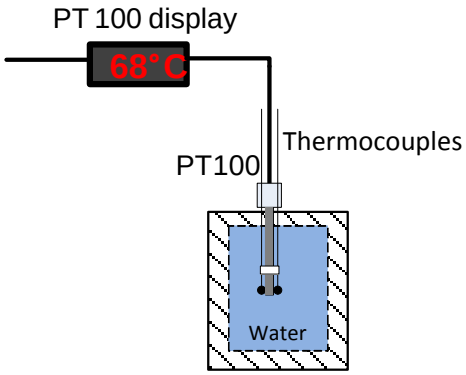

Figure B.1 Diagram of thermocouple calibration procedure

Calibration was performed by allowing hot water to naturally cool very slowly in the insulated chamber without any mixing or stirring. The chamber was filled with hot water at approximately 80°C. A Labview interface was programmed to start logging measurements when the temperature decreased to approximately 66°C. Each calibration point was based on 100 data points logged at a frequency of 20 Hz. The Labview script was automated so that once the first temperature was reached, the software set a new temperature at which logging would commence once reached. The decrement was kept at 2°C, chosen because a small increment provides a better linear approximation over the entire range. The insulation temperature was approximately 25°C.

All the data was appended to a single file, which was used to calibrate all the thermocouples. This file stored a timestamp for each measurement, the PT100 measurement and all the thermocouple measurements. The file was analysed by a Labview script, which averaged each set of measurements to a single value for each thermocouple. This resulted in up to 26 points that were used for the calibration procedure. A linear calibration model was applied to the thermocouple data. Each thermocouple was plotted against the PT100 in accordance to equation (B.1). The PT100, assumed to be the exact temperature, was placed on the *y-axis*, and the thermocouples on the x-axis.

$$T_{cal} \cong T_{PT100} = mT_{thermocuple} + c \qquad \text{(B.1)}$$

The linear coefficients (m and c) were determined for each thermocouple, and an example of the linear regression is given in Figure B.2 for a wall thermocouple. Figure B.2 shows the data for three thermocouples of different locations in the test section, and gives the calibration equation for the wall thermocouple only. The same procedure was done for all thermocouples.

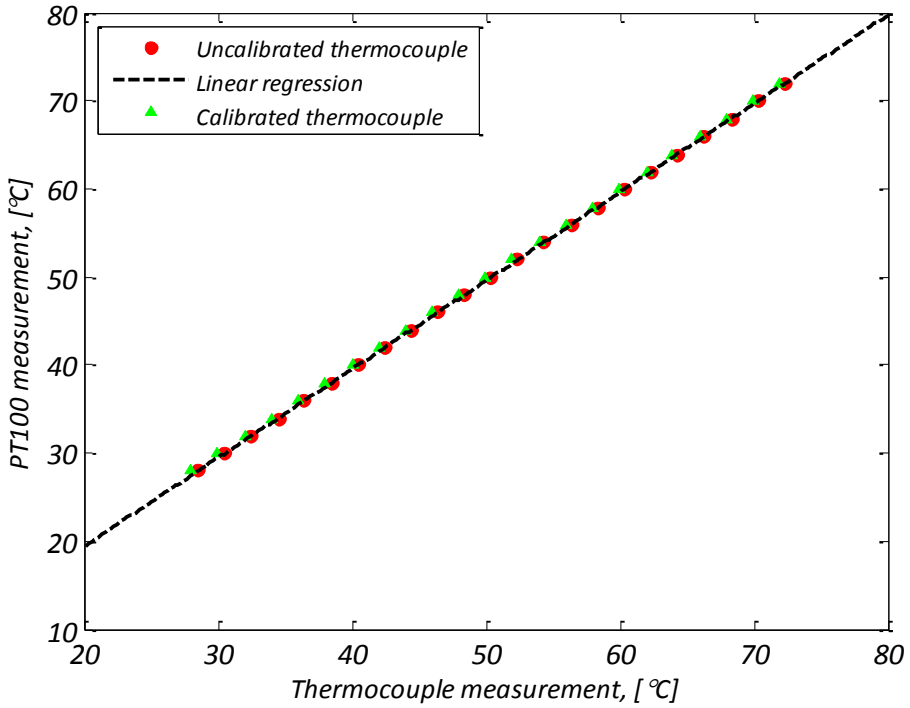

Figure B.2 Example of linear regression calibration

To ensure that the calibration was successful, each thermocouple was validated against the PT100 using two different temperature values, one high and one low. There was an associated uncertainty with this calibration method, which determined the accuracy of the calibration. Details of the uncertainty analysis are given in Appendix D. Approximately 99% of the thermocouples were determined to have an uncertainty below 0.1°C. An uncertainty of 0.1°C was adopted for each thermocouple as a cautious approach to the uncertainty analysis of the thermocouples. Information of the thermocouple calibration is given for each test section Tables B.1 to B.3. The uncertainty analysis procedure is given in Appendix D.

B.3 Thermocouple calibration information and data

B.3.1 Calibration data: 1.05mm test section

Location			*Calibration*		*Equation*		*Deviation from PT100*			*Uncertainty*	
	#	Code	Range (°C)		m	c	Maximum	Minimum	Average	PT100	Total
Inlet	1	T_{in} 1	70	28	1.002543	-0.27742	0.0583876	0.0551451	0.05632		0.0708
	2	T_{in} 2	70	28	1.00217	-0.56071	0.0588934	0.0555343	0.05672		0.0712
	3	T_{in} 3	70	28	1.002175	-0.2348	0.0578951	0.0546868	0.05585		0.0704
	4	T_{in} 4	70	28	1.00237	-0.28845	0.063001	0.0594973	0.06077		0.0746
Outlet	1	T_{out} 1	70	28	1.00443	-0.63824	0.0661234	0.0623618	0.0637		0.0773
	2	T_{out} 2	70	28	1.002911	-0.28535	0.0606537	0.0572905	0.05851		0.0727
	3	T_{out} 3	70	28	1.00296	-0.22488	0.0618623	0.0584533	0.0597		0.0737
	4	T_{out} 4	70	28	1.003797	-0.55759	0.0619856	0.0584763	0.05973		0.0738
Wall	1	T_w 1-1	60	26	1.0336	-3.30404	0.0615939	0.0566173	0.0582		0.0734
	2	T_w 1-2	60	26	1.037213	-3.14158	0.0651905	0.0600412	0.06173		0.0765
	3	T_w 2-1	60	26	1.035642	-3.03849	0.0647922	0.0597009	0.06137		0.0761
	4	T_w 2-2	60	26	1.032166	-2.8425	0.0670157	0.061805	0.06352		0.0780
	5	T_w 3-1	60	26	1.031081	-3.02419	0.0635749	0.0585375	0.06017		0.0751
	6	T_w 3-2	60	26	1.03798	-3.04048	0.0751069	0.0692412	0.07119		0.0851
	7	T_w 4-1	60	26	1.03803	-3.04668	0.0693618	0.0639427	0.06574	0.04	0.0801
	8	T_w 4-2	60	26	1.036746	-2.73552	0.0699844	0.0646525	0.06646		0.0806
Insulation	1	T_{ins} 1	58	28	0.996731	-0.50122	0.0627037	0.0580096	0.05967		0.0744
	2	T_{ins} 2	58	28	0.99747	-0.60356	0.0486353	0.0449601	0.04625		0.0630
	3	T_{ins} 3	58	28	0.995637	-0.44424	0.0555039	0.0513589	0.05282		0.0684
	4	T_{ins} 4	58	28	0.996019	-0.59154	0.0637158	0.0588791	0.06056		0.0752
	5	T_{ins} 5	58	28	0.997469	-0.55311	0.0482823	0.0446524	0.04593		0.0627
	6	T_{ins} 6	58	28	0.999948	-0.65714	0.0583999	0.0539975	0.05555		0.0708
	7	T_{ins} 7	58	28	0.998172	-0.3648	0.071511	0.06627	0.06816		0.0819
	8	T_{ins} 8	58	28	0.99811	-0.38688	0.0941666	0.0872388	0.08973		0.1023
	9	T_{ins} 9	58	28	0.994574	-0.36804	0.0682355	0.0631569	0.06495		0.0791
	10	T_{ins} 10	58	28	0.995477	-0.32004	0.0604532	0.0559981	0.05759		0.0725
	11	T_{ins} 11	58	28	0.998323	-0.49044	0.0529162	0.048984	0.05039		0.0663
	12	T_{ins} 12	58	28	0.997038	-0.65231	0.0495804	0.0458024	0.04712		0.0637
Heater	1	T_{he} 1	64	30	1.003358	-1.8868	0.0681832	0.0629909	0.06466		0.0791
Element	2	T_{he} 2	64	30	1.002929	-1.77682	0.0698647	0.0645917	0.0663		0.0805
Ambient	1	T_{amb} 1	58	28	0.997487	-0.31625	0.0647543	0.0600156	0.06172		0.0761
	2	T_{amb} 2	58	28	1.00089	-0.34505	0.0773802	0.0717756	0.07383		0.0871

Table B.1 Thermocouple calibration details for the 1.05mm test section

B.3.2 Calibration data: 0.85mm test section

Location			Calibration		Equation		Deviation from PT100			Uncertainty	
	#	Code	Range (°C)		m	c	Maximum	Minimum	Average	PT100	Total
Inlet	1	T_{in} 1	70	28	1.004907	-0.86949	0.069689	0.065654	0.06707		0.0804
	2	T_{in} 2	70	28	1.005296	-0.69308	0.068459	0.06455	0.065941		0.0793
	3	T_{in} 3	70	28	1.004344	-0.57209	0.065269	0.061576	0.0629		0.0766
	4	T_{in} 4	70	28	1.004485	-0.40323	0.065418	0.061772	0.063097		0.0767
Outlet	1	T_{out} 1	70	28	1.004761	-0.71129	0.070124	0.066108	0.067532		0.0807
	2	T_{out} 2	70	28	1.004239	-0.4516	0.074326	0.070162	0.071668		0.0844
	3	T_{out} 3	70	28	1.003870	-0.48655	0.065939	0.062233	0.063569		0.0771
	4	T_{out} 4	70	28	1.004160	-0.09252	0.066354	0.062737	0.064078		0.0775
Wall	1	T_w 1-1	70	28	1.002051	-2.75767	0.079717	0.074311	0.075968		0.0892
	2	T_w 1-2	70	28	1.002112	-2.67294	0.072199	0.067337	0.068835		0.0825
	3	T_w 2-1	70	28	1.001128	-2.34704	0.072272	0.067524	0.069009		0.0826
	4	T_w 2-2	70	28	1.001548	-2.4833	0.133311	0.124483	0.127234		0.1392
	5	T_w 3-1	70	28	1.001638	-2.42768	0.06814	0.063635	0.065038	0.04	0.0790
	6	T_w 3-2	70	28	1.001449	-2.54646	0.069988	0.065317	0.066764		0.0806
	7	T_w 4-1	70	28	1.001214	-2.56234	0.074747	0.06975	0.071295		0.0848
	8	T_w 4-2	70	28	1.002404	-2.77819	0.077462	0.072208	0.07382		0.0872
Insulation	1	T_{ins} 1	66	22	1.00453	-0.5687	0.050023	0.047282	0.048258		0.0640
	2	T_{ins} 2	66	22	1.00373	-0.63266	0.051548	0.048703	0.049707		0.0652
	3	T_{ins} 3	66	22	1.004712	-0.79905	0.054359	0.051328	0.052387		0.0675
	4	T_{ins} 4	66	22	1.004071	-0.67596	0.055167	0.052116	0.053191		0.0681
Heater Element	1	T_{ins} 5	66	22	1.004153	-1.81979	0.054905	0.051585	0.052664		0.0679
	2	T_{ins} 6	66	22	1.003126	-1.79327	0.050872	0.047797	0.048795		0.0647
Ambient	1	T_{ins} 7	66	22	1.004327	-0.44489	0.038493	0.036405	0.037156		0.0555
	2	T_{ins} 8	66	22	1.005454	-0.55972	0.04655	0.044006	0.044916		0.0614

Table B.2 Thermocouple calibration details for the 0.85mm test section

B.3.3 Calibration data: 0.57mm test section

Location			Calibration		Equation		Deviation from PT100			Uncertainty	
	#	Code	Range (°C)		m	c	Maximum	Minimum	Average	PT100	Total
Inlet	1	T_{in} 1	66	22	1.00819	-0.911392	0.05305545	0.05008264	0.05112367	0.04	0.0664
	2	T_{in} 2	66	22	1.006031	-0.667682	0.0470625	0.04446743	0.04538797		0.0618
	3	T_{in} 3	66	22	1.006846	-0.601666	0.05023775	0.04748588	0.0484705		0.0642
	4	T_{in} 4	66	22	1.006369	-0.433912	0.04950631	0.0468307	0.04780089		0.0636
Outlet	1	T_{out} 1	66	22	1.006803	-0.730736	0.04625061	0.04368787	0.04459368		0.0611
	2	T_{out} 2	66	22	1.00588	-0.498773	0.04437925	0.04196312	0.04283164		0.0597
	3	T_{out} 3	66	22	1.005897	-0.515997	0.04670215	0.04415635	0.04507028		0.0615
	4	T_{out} 4	66	22	1.005084	-0.143428	0.04334213	0.04102616	0.04187396		0.0590
Wall	1	T_w 1-1	66	22	1.005478	-2.722427	0.05993814	0.05606258	0.05725891		0.0721
	2	T_w 1-2	66	22	1.005806	-2.715063	0.06574543	0.06150061	0.0628132		0.0770
	3	T_w 2-1	66	22	1.004991	-2.438296	0.05805992	0.05438061	0.05553376		0.0705
	4	T_w 2-2	66	22	1.004787	-2.57043	0.0601675	0.05631659	0.0575138		0.0723
	5	T_w 3-1	66	22	1.004712	-2.501109	0.05639586	0.05280375	0.0539246		0.0691
	6	T_w 3-2	66	22	1.004927	-2.589521	0.05433543	0.05085085	0.05193244		0.0675
	7	T_w 4-1	66	22	1.005697	-2.636406	0.05790581	0.05418472	0.05533916		0.0704
	8	T_w 4-2	66	22	1.004775	-2.67084	0.0660287	0.06177659	0.06309256		0.0772
Insulation	1	T_{ins} 1	66	22	1.00453	-0.568703	0.05002295	0.0472819	0.04825785		0.0640
	2	T_{ins} 2	66	22	1.00373	-0.632664	0.05154784	0.04870314	0.04970683		0.0652
	3	T_{ins} 3	66	22	1.004712	-0.799052	0.05435894	0.05132755	0.0523872		0.0675
	4	T_{ins} 4	66	22	1.004071	-0.67596	0.05516748	0.05211635	0.05319105		0.0681
Heater Element	1	T_{ins} 5	66	22	1.004153	-1.819793	0.05490482	0.0515849	0.05266367		0.0679
	2	T_{ins} 6	66	22	1.003126	-1.793273	0.05087184	0.04779696	0.04879497		0.0647
Ambient	1	T_{ins} 7	66	22	1.004327	-0.444892	0.03849329	0.03640457	0.03715577		0.0555
	2	T_{ins} 8	66	22	1.005454	-0.559718	0.04654966	0.04400605	0.04491606		0.0614

Table B.3 Thermocouple calibration details for the 0.57mm test section

Appendix C Calibration of the pressure transducer diaphragms

Nomenclature

c	Linear regression constant	Pa
m	Linear regression gradient	Pa/V
V_{DP15}	DP15 raw input voltage	V

Greek letters

ΔP_{cal}	Calibrated differential pressure	Pa
ΔP_{exact}	Exact differential pressure	Pa
ΔP_{mano}	Digital manometer differential pressure measurement	Pa

C.1 Introduction

Two methods were employed to calibrate the pressure transducer diaphragms; a water column (for the low-pressure diaphragm) and a dead-weight system (for the high-pressure diaphragm). Table C.1 gives the diaphragms and the calibration information.

Diaphragm #	*Maximum pressure [kPa]*	*Calibration method*	*Manometer uncertainty [Pa]*
34	20	Water column	50
44	220	Dead-weight system	200

Table C.1 Pressure transducer calibration specifications

Figure C.1 gives the diagram of the connections between the pressure transducer, the digital manometer and the calibration unit (note that they are not drawn to scale). The digital manometer and the pressure transducer were connected in parallel to the calibration unit. The dead-weight system required that the low-pressure side be open to ambient, while the water column low-pressure terminal was connected to the short column. The calibration units were used independently and were not linked to the pressure transducer or digital manometer at the same time (as may be depicted by Figure C.1).

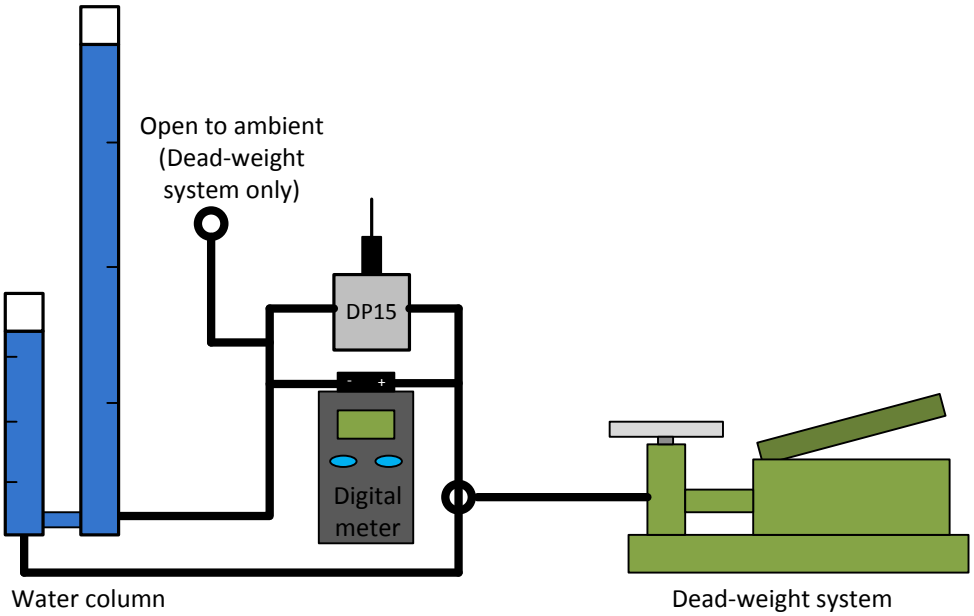

Figure C.1 Calibration equipment and connection diagram

C.2 Calibration of pressure transducer

The same calibration technique was applied for both the diaphragms regardless of the calibration method. The pressure transducer *zero* and *span* were set initially. For both calibration methods, the system was pressurised to a desired value, and both the digital manometer and pressure transducer voltage were logged. A linear relationship was then formed between the pressure transducer output voltage and the digital manometer pressure value using equation C.1.

$$\Delta P_{exact} \cong \Delta P_{cal} = \Delta P_{mano} = mV_{DP15} + c \quad \text{(C.1)}$$

The relationship attained was then verified by applying a pressure to the system and comparing the calibrated pressure transducer reading (ΔP_{cal}) with the digital manometer reading.

C.3 Pressure transducer calibration data and graphs

The calibration data for diaphragm #34 and diaphragm #44 are given in Table C.2 and Table C.3 respectively. The data was plotted and a linear curve fit was applied to the data and the calibration coefficients were determined, given in Figures C.2 and C.3. Details of the uncertainty analysis are given in Appendix D.

Voltage [V]	*ΔP_{mano} [Pa]*	*m*	*c*	*ΔP_{cal} [Pa]*	*Difference [Pa]*	*Deviation [%]*	*Average [Pa]*
0.76351	1720	2204.17	61.57	1744.48	24.478	1.423	28.567
1.72960	3880			3873.91	6.093	0.157	
2.68320	5980			5975.81	4.194	0.070	
3.53060	7900			7843.62	56.377	0.714	
4.51970	10040			10023.77	16.230	0.162	
5.34600	11870			11845.08	24.922	0.210	
6.24530	13860			13827.29	32.709	0.236	
7.59380	16830			16799.62	30.382	0.181	
8.46420	18720			18718.13	1.870	0.010	
9.71650	21390			21478.42	88.416	0.413	

Table C.2 DP15 #34 calibration data

Voltage [V]	*ΔP_{mano} [Pa]*	*m*	*c*	*ΔP_{cal} [Pa]*	*Difference [Pa]*	*Deviation [%]*	*Average [Pa]*
0.1151265	2140	21994.80	-466.42	2065.77	74.233	3.469	386.930
2.3462908	51050			51606.20	556.196	1.090	
4.8520662	106200			106720.22	520.221	0.490	
6.6787183	146500			146897.07	397.069	0.271	

Table C.3 DP15 #44 calibration data

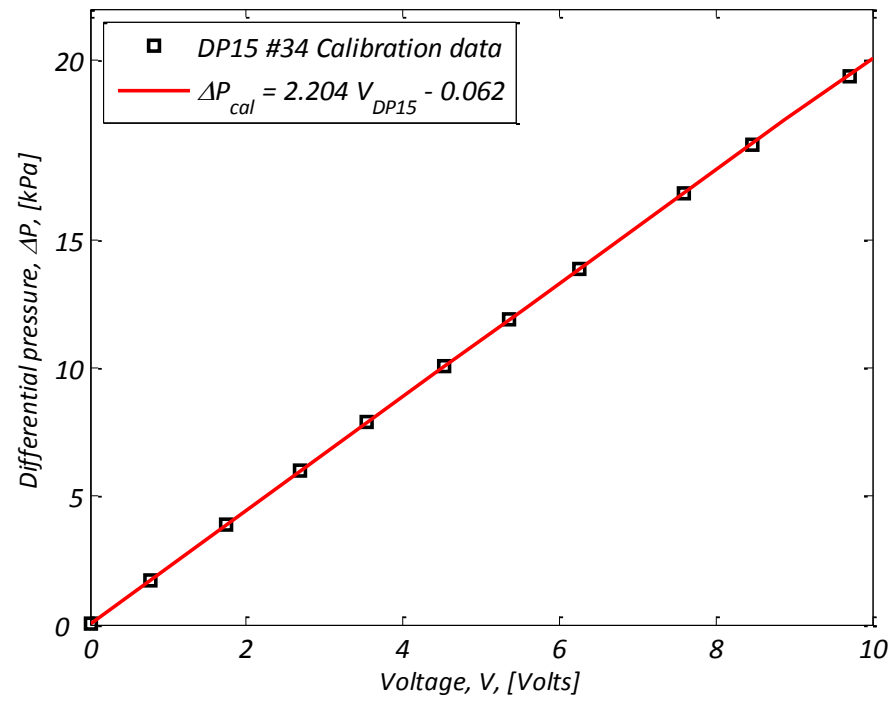

Figure C.2 DP15 #34 calibration points and linear regression curve

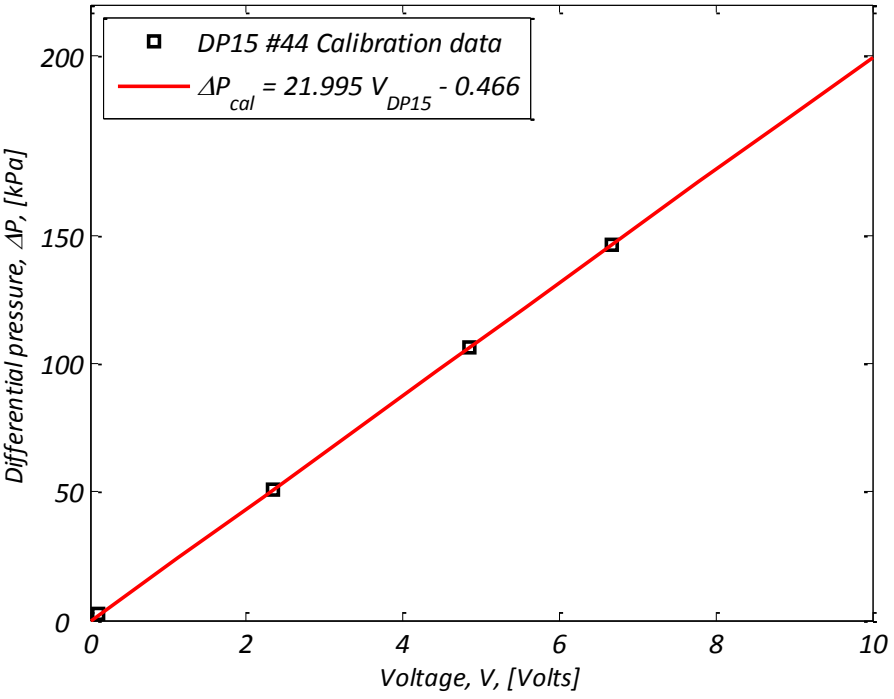

Figure C.3 DP15 #44 calibration points and linear regression curve

Appendix D Uncertainty analysis

Nomenclature

$a, b, c, .., m$	Constants	$-$
A_c	Cross-sectional area	m
A_s	Surface area	m
C_p	Specific heat	J/kgK
D_h	Hydraulic diameter	m
f	Friction factor	$-$
g	Function	$-$
$\bar{h}$	Average heat transfer coefficient	W/m^2K
H	Channel height	m
$\bar{I}$	Average input current	A
j	Colburn j-factor	$-$
k	Thermal conductivity	W/mK
L	Channel length	m
L_p	Channel pressure length	m
$\dot{m}$	Fluid mass flow rate	kg/s
n	Number of points	$-$
$\overline{Nu}$	Average Nusselt number	$-$
P	Random error	$units$
P_w	Wetted perimeter	m
ΔP	Differential pressure	Pa
Pr	Prandtl number	$-$
$\bar{\dot{Q}}_{in}$	Average power input	W
$\bar{\dot{Q}}_{out}$	Average power rate transferred by fluid	W
R	General equation	$-$
T	Single temperature value	$°C$

$\bar{T}_b$	Average bulk fluid temperature	$°C$
T_{cal}	Calibrated temperatures	$°C$
$\bar{T}_{in}$	Average inlet temperature	$°C$
$\bar{T}_{i,o}$	Average inlet-outlet temperature difference	$°C$
T_{node_i}	Non-specific wall node temperature	$°C$
$\bar{T}_{out}$	Average outlet temperature	$°C$
T_{PT100}	PT100 reference temperature	$°C$
T_{uncal}	Uncalibrated temperatures	$°C$
$\bar{T}_{uncal}$	Average uncalibrated temperatures	$°C$
$\bar{T}_{w,trap}$	Average trapezoidal wall temperature	$°C$
$\bar{T}_{w,b}$	Average wall-bulk temperature difference	$°C$
v	Fluid velocity	m/s
$\bar{V}$	Average input voltage	V
W	Channel width	m
$x_{1,2,3,\ldots,n}$	Variables	$-$
x_i	Non-specific variable	$-$
$x_{i,meas}$	Non-specific measurement value	$-$

Greek letters

ρ	Fluid density	kg/m^3
μ	Fluid viscosity	kg/ms
σ_{PT100}	Uncertainty of the variance of the thermocouple to the PT100	$°C$
$\sigma_{s,mfm}$	Mass flow meter uncertainty equation	$-$
σ_T	Calibration uncertainty of thermocouple	$°C$

D.1 Introduction

An uncertainty analysis was used to determine the accuracy of the instrumentation and the final results. The uncertainties associated with microchannel flow were not differently approached than with larger systems, but due to the low operating flow rates in the laminar regime and low temperature differences in the turbulent regime, a higher uncertainty was expected. The uncertainty of the results was calculated using the methods prescribed by Kline and McClintock [D.1] and Moffat [D.2]. The two approaches provided applicable methods to solve for the accuracy of the equipment. A 95.4% confidence level was adopted for this study. Though this resulted in a higher uncertainty value, it provided a higher quality of result accuracy.

D.2 Uncertainty analysis method

Moffat used the definition assuming that two types of errors exist, the bias (or fixed) errors, and the precision (or random) errors. Bias (B_i) errors are regarded as offset values, where the equipment calibration is out by a calculable magnitude. Precision (P_i) errors refer to the fluctuation of the measurement value at the point of calibration. These errors are dependent on the operating conditions of the equipment, manufacturer-specified stability, system vibration and other causes. This method was for a single-point measurement, and is defined by equation (D.1).

$$\delta x_i = [(B_i)^2 + (P_i)^2]^{\frac{1}{2}} \tag{D.1}$$

Kline and McClintock [D.1] defined a more applicable set of uncertainty definitions as not confined to single-point measurements, but also multipoint measurements, and is given in equation (D.2) .

$$x_i = x_{i,meas} \pm \delta x_i \tag{D.2}$$

Now, given as equation R, which has variables x_i, we define a general form of an equation, equation (D.3).

$$R = g(x_1, x_2, x_3, \dots, x_n) \tag{D.3}$$

If the uncertainties of x_i are known, the effect of a single-measurement uncertainty of R can be determined using equation (D.4).

$$\delta R = \frac{\partial R}{\partial x_i} \delta x_i \tag{D.4}$$

δR is known as the sensitivity coefficient, and was used to determine the effect that x_i has on the overall uncertainty. For a group of variables as defined in equation (D.3), a root-sum-squared method was applied to find the uncertainty caused by the independent variables, given by equation (D.5).

$$\delta R = \left[\left(\frac{\partial R}{\partial x_1}\delta x_1\right)^2 + \left(\frac{\partial R}{\partial x_2}\delta x_2\right)^2 + \left(\frac{\partial R}{\partial x_3}\delta x_3\right)^2 + \cdots + \left(\frac{\partial R}{\partial x_n}\delta x_n\right)^2\right]^{\frac{1}{2}} \quad \text{(D.5)}$$

The form of a general equation with powers is given by equation (D.6). These higher level equations were used in the data analysis procedure, such as the friction factor equation, where some variables contained powers. The uncertainty of this form of general equation is given by equation (D.7)

$$R = f(x_1^a, x_2^b, x_3^c, \ldots, x_n^m) \quad \text{(D.6)}$$

$$\frac{\delta R}{R} = \left[\left(a\frac{\delta x_1}{x_1}\right)^2 + \left(b\frac{\delta x_2}{x_2}\right)^2 + \left(c\frac{\delta x_3}{x_3}\right)^2 + \cdots + \left(m\frac{\delta x_n}{x_n}\right)^2\right]^{\frac{1}{2}} \quad \text{(D.7)}$$

Calculating a ratio for the uncertainty $\left(\frac{\delta R}{R}\right)$ provided a much easier method of analysing the data while keeping the uncertainty in a ratio with the general equation. This form of uncertainty is known as the relative uncertainty.

D.3 Uncertainty of water properties

Water properties are calculated by the equations prescribed by Popiel and Wojtkowiak [D.3] as discussed in Appendix A. The uncertainties associated with these equations were specified by the authors and are given in Table D.1.

	$\boldsymbol{\rho}$	$\boldsymbol{C_p}$	$\boldsymbol{k}$	$\boldsymbol{\mu}$	$\boldsymbol{Pr}$
Standard uncertainty [%]	0.004	0.06	2.0	1.0	2.3
95.4% Confidence level [%]	0.008	0.12	4.0	2.0	4.6

Table D.1 Uncertainties of the calculated fluid properties

D.4 Uncertainty of mass flow meter

The mass flow meter had a standard uncertainty of 0.05% of the measurement value for flow rates above 5% of the full-scale value of 1.36 kg/min. For a confidence interval of 95.4%, the mass flow meter uncertainty used for this study's analysis becomes 0.1% for values of flow above 5% of the

full-scale value. Flow rates below 5% have a larger uncertainty, which was calculated using equation (D.8).

$$\sigma_{s,mfm} = \frac{0.0034}{\dot{m}} \quad \{\dot{m} \leq 0.001133 kg/s\} \tag{D.8}$$

D.5 Microchannel dimension uncertainty

The dimensions of the microchannel were measured using a digital microscope of maximum uncertainty of 5 µm. The uncertainty of the measurement of the PTFE tape, which was used to seal the test section during clamping, was also 5 µm. This extra layer affected the overall microchannel height, and increased its uncertainty. The dimensional uncertainties are given in Table D.2.

Dimension	*Uncertainty [mm]*
W	0.005
H	0.071
L	0.20
L_p	0.05

Table D.2 Uncertainties of the dimensional characteristics of the microchannel

From the literature study, it was imperative that there should be high accuracy dimensional measurements as these have been known to cause result deviation (refer to Section 1.2 Previous Work).

D.6 Uncertainty of thermocouples

Equation (D.8) is used to determine the uncertainty of the thermocouple calibration procedure. The PT100 uncertainty (δT_{PT100}) was included in the analysis as it had its own manufacturer-specified accuracy. The method utilised for the calibration was that prescribed by Hocking [D.4]. The method determines the deviation of the calibrated temperature data (T_{cal}) from the calibration instrument, or in this case, the PT100 temperature (T_{PT100}). This value was determined using equation (D.9). The deviation of the uncalibrated temperature measurements (T_{uncal}) was factored into the equation to determine the precision error from calibration. This was calculated using equation (D.10), and included the calibration instrumentation uncertainty of equation (D.9).

$$\sigma_{PT100} = \sqrt{\frac{\sum_{cal=1}^{n}(T_{cal} - T_{PT100})^2}{(n-2)}} \quad \text{(D.9)}$$

$$\sigma_T = \sigma_{PT100}\sqrt{1 + \frac{1}{n} + \frac{(T_{cal} - \bar{T}_{uncal})^2}{\sum_{uncal=1}^{n}(T_{uncal} - \bar{T}_{uncal})^2}} \quad \text{(D.10)}$$

Where $\bar{T}_{uncal}$ is defined by equation (D.11)

$$\bar{T}_{uncal} = \frac{\sum_{uncal=1}^{n} T_{uncal}}{n} \quad \text{(D.11)}$$

Once this procedure was completed, the maximum thermocouple uncertainty (σ_T) was used to determine the final thermocouple uncertainty value, along with the PT100 uncertainty (δT_{PT100}). These were combined using equation (D.12). The maximum thermocouple uncertainty was multiplied by a factor of 2 to determine the 95.4% confidence level. The result of the thermocouple uncertainty analysis yielded uncertainties below 0.1°C (except in one case where there was an uncertainty above 0.1°C, as mentioned in Appendix B). To provide an easier but more cautious approach to the uncertainty analysis, a constant value of 0.1°C was adopted as the thermocouple uncertainty.

$$\delta T = (\delta T_{PT100}^2 + 2(\max(\sigma_T))^2)^{\frac{1}{2}} \quad \text{(D.12)}$$

D.6.1 Inlet and outlet thermocouples

Four thermocouples were attached to the inlet measuring section and four to the outlet measuring section of the test section. Since multiple thermocouples were used to measure a single value, the inlet and outlet temperatures were calculated as the average of the measured temperatures, given by equation (D.13).

$$\bar{T}_{in} = \frac{T_{in_1} + T_{in_2} + \cdots + T_{in_n}}{n} \quad \text{(D.13)}$$

The uncertainty of such a measurement was calculated using equation (D.14).

$$\delta\bar{T}_{in} = \left[\left(\frac{\delta T_{in_1}}{n}\right)^2 + \left(\frac{\delta T_{in_2}}{n}\right)^2 + \cdots + \left(\frac{\delta T_{in_n}}{n}\right)^2\right]^{\frac{1}{2}} \quad \text{(D.14)}$$

Since the values of the thermocouple uncertainties were all 0.1°C, equation (D.14) simplified to equation (D.15).

$$\delta\bar{T}_{in} = \sqrt{\frac{1}{n}}\,\delta T \tag{D.15}$$

Equation (D.15) was used to determine the uncertainty of all single-point temperature measurements that use multiple thermocouples, such as the inlet and outlet fluid temperature. These uncertainties are given in Table D.3.

Location	*Uncertainty [°C]*	*No. of thermocouples [-]*	*Final uncertainty [°C]*
Inlet	0.1	4	0.05
Outlet		4	0.05

Table D.3 Uncertainties of the fluid inlet and outlet temperature measurements

D.6.2 Wall temperature uncertainty

Four wall thermocouple positions were evenly spaced along the channel length. Each position had two thermocouples with which the wall temperatures from both the left and right side walls were measured. The node temperature was calculated by averaging the two wall temperatures, given by equation (D.16).

$$\bar{T}_{node_i} = \frac{1}{2}\left(T_{w_{i,1}} + T_{w_{i,2}}\right)\ [i = 1, \ldots, 4] \tag{D.16}$$

The temperature uncertainty of each node was calculated using equation (D.17).

$$\delta\bar{T}_{node_i} = \sqrt{\frac{1}{2}}\,\delta T \tag{D.17}$$

The average wall temperature was calculated using the trapezoidal rule. While four wall temperature nodes measured the wall temperatures at discrete locations of the channel wall, the trapezoidal rule required that the entire wall length temperature be averaged. The first and the last temperature nodes were extrapolated to determine the temperatures at end points of the channel. These calculated nodes were labelled T_{node_0} and T_{node_5}. This procedure is graphically represented in Figure D.1.

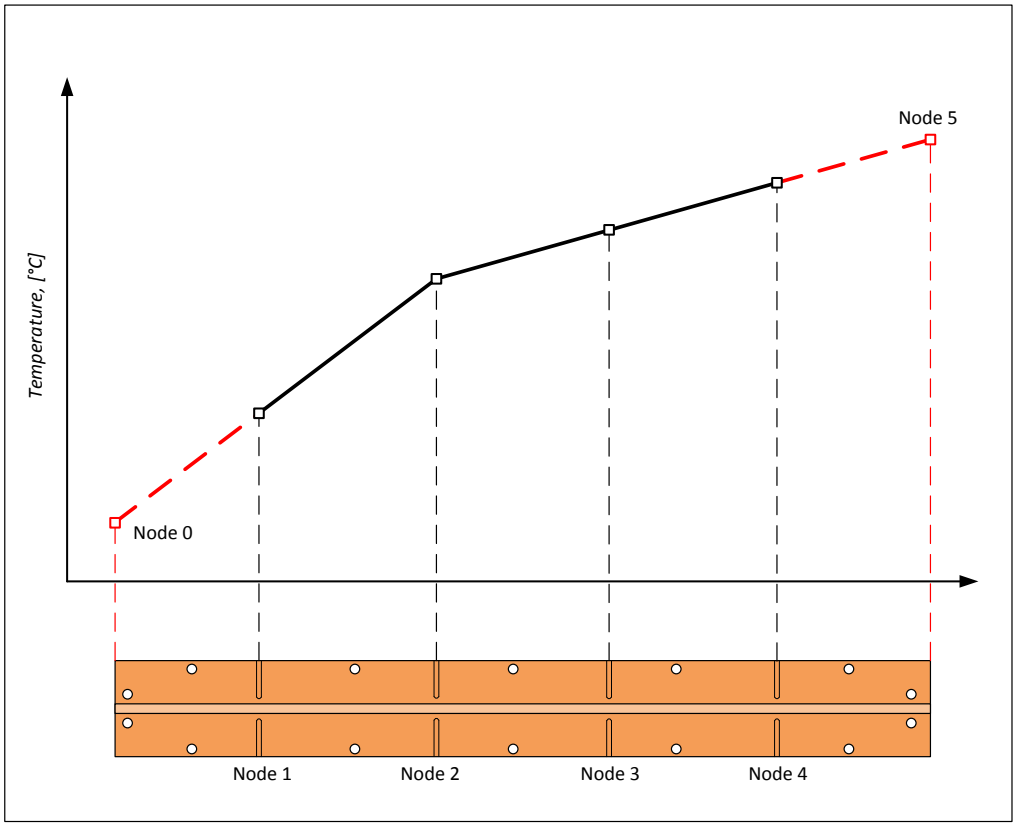

Figure D.1 Trapezoidal wall temperature extrapolation method

The extrapolation resulted in a total of six wall temperature measurements used for the trapezoidal rule. The trapezoidal average wall temperature was calculated using equation (D.18).

$$\bar{T}_{w,trap} = \frac{1}{2(n-1)}\left(\bar{T}_{node_0} + 2\bar{T}_{node_1} + 2\bar{T}_{node_2} + \cdots + 2\bar{T}_{node_{n-1}} + \bar{T}_{node_n}\right) \quad \text{(D.18)}$$

The trapezoidal average wall temperature uncertainty was then calculated using equation (D.19).

$$\delta\bar{T}_{w,trap} = \left[\frac{1}{4(n-1)^2}\left(\delta\bar{T}_{node_0}^{\,2} + \overline{\delta T}_{node_n}^{\,2}\right) + \frac{1}{(n-1)^2}\left(\delta\bar{T}_{node_1}^{\,2} + \cdots + \delta\bar{T}_{node_{n-1}}^{\,2}\right)\right]^{\frac{1}{2}} \quad \text{(D.19)}$$

The wall thermocouples were positioned at a maximum distance of 0.4 mm from the side walls. Numerical investigations determined that there was up to a 0.05°C temperature difference between the measurement and the ideal wall temperature. This low temperature difference was determined to have little effect on the heat transfer coefficient calculation, falling in the region of uncertainty. For this reason, the temperature difference due to location was deemed to be negligible.

D.6.3 Temperature difference uncertainty

In heat transfer and Nusselt number calculations, the temperature difference between the inlet and outlet temperatures, and bulk and wall temperatures, must be accurately calculated in order to produce the correct interpretation of the results. In the event that there is a very small temperature difference, the associated relative uncertainty can be very large. The inlet and outlet temperature difference is represented in equation (D.20).

$$\Delta\bar{T}_{i,o} = \bar{T}_{in} - \bar{T}_{out} \tag{D.20}$$

Applying the uncertainty analysis method results in equation (D.21)

$$\delta\Delta\bar{T}_{i,o} = \left(\delta\bar{T}_{in}^2 + \delta\bar{T}_{out}^2\right)^{\frac{1}{2}} \tag{D.21}$$

Similarly, this can be applied to the bulk and wall temperature difference, as shown in equation (D.22).

$$\delta\Delta\bar{T}_{w,b} = \left(\delta\bar{T}_{w,trap}^2 + \delta\bar{T}_{b}^2\right)^{\frac{1}{2}} \tag{D.22}$$

The result of the temperature difference uncertainty is tabulated in Table D.4.

Temperature difference [°C]	*Uncertainty range*
Outlet - Inlet	0.5% - 3%
Wall - Bulk	3% - 35%

Table D.4 Temperature difference uncertainties

The wall to bulk fluid temperature resulted in very high uncertainties due to the low difference between the two measurements in the turbulent regime. This dominated the high uncertainty that was associated with the Nusselt number in the turbulent regime.

D.7 Heat transfer rate uncertainty analysis

The average heat transfer rate is defined as the amount of heat transferred to the fluid from the heater element. This is calculated using equation (D.23).

$$\begin{aligned}\bar{\dot{Q}}_{out} &= \dot{m}C_p(\bar{T}_{in} - \bar{T}_{out}) \\ &= \dot{m}C_p\Delta T_{i,o}\end{aligned} \tag{D.23}$$

The uncertainty of the average heat transfer rate is given below:

$$\delta\bar{\dot{Q}}_{out} = \left[\left(\frac{\partial\bar{\dot{Q}}_{out}}{\partial\dot{m}}\delta\dot{m}\right)^2 + \left(\frac{\partial\bar{\dot{Q}}_{out}}{\partial C_p}\delta C_p\right)^2 + \left(\frac{\partial\bar{\dot{Q}}_{out}}{\partial\Delta\bar{T}_{i,o}}\delta\Delta\bar{T}_{i,o}\right)^2\right]^{\frac{1}{2}} \quad \text{(D.24)}$$

$$\therefore \frac{\delta\bar{\dot{Q}}_{out}}{\bar{\dot{Q}}_{out}} = \left[\left(\frac{\delta\dot{m}}{\dot{m}}\right)^2 + \left(\frac{\delta C_p}{C_p}\right)^2 + \left(\frac{\delta\Delta\bar{T}_{i,o}}{\Delta\bar{T}_{i,o}}\right)^2\right]^{\frac{1}{2}} \quad \text{(D.25)}$$

The average heat input from the heat element is calculated by equation (D.26).

$$\bar{\dot{Q}}_{in} = \bar{V}\bar{I} \quad \text{(D.26)}$$

The uncertainty analysis is given below:

$$\delta\bar{\dot{Q}}_{in} = \left[\left(\frac{\partial\bar{\dot{Q}}_{in}}{\partial\bar{V}}\delta\bar{V}\right)^2 + \left(\frac{\partial\bar{\dot{Q}}_{in}}{\partial\bar{I}}\delta\bar{I}\right)^2\right]^{\frac{1}{2}} \quad \text{(D.27)}$$

$$\therefore \frac{\delta\bar{\dot{Q}}_{in}}{\bar{\dot{Q}}_{in}} = \left[\left(\frac{\delta\bar{V}}{\bar{V}}\right)^2 + \left(\frac{\delta\bar{I}}{\bar{I}}\right)^2\right]^{\frac{1}{2}} \quad \text{(D.28)}$$

The uncertainties of the power input and power outputs are given in Table D.5.

Measurement	***Uncertainty range***
Average power input $[\bar{\dot{Q}}_{in}]$	0.51%
Average power output $[\bar{\dot{Q}}_{out}]$	0.35% - 44%

Table D.5 Power input and output uncertainties

The high power output uncertainty occurred at the lowest values of flow rate where the mass flow meter uncertainty was at its highest. This caused a very high uncertainty in the average power output measurement, especially in the 0.57 mm test section where the lowest flow rate was experienced.

D.8 Heat transfer coefficient and Nusselt number uncertainty

The heat transfer coefficient is used as a measure of the effectiveness of the heat transfer mechanism and is non-dimensionalised in the form of the Nusselt number. The average heat transfer coefficient is defined by equation (D.29)

$$\bar{h} = \frac{\bar{\dot{Q}}_{out}}{A_s\left(\bar{T}_{w,trap} - \bar{T}_b\right)} \tag{D.29}$$

The surface area A_s is the internal surface area of the microchannel, calculated using equation (D.30).

$$A_s = 2(W + H)L \tag{D.30}$$

The width and height combination uncertainty is given in equation (D.31).

$$\delta(W + H) = (\delta W^2 + \delta H^2)^{\frac{1}{2}} \tag{D.31}$$

The surface area uncertainty is given below:

$$\delta A_s = \left[\left\{\frac{\partial A_s}{\partial(W + H)}\delta(W + H)\right\}^2 + \left\{\frac{\partial A_s}{\partial L}\delta L\right\}^2\right]^{\frac{1}{2}} \tag{D.32}$$

$$\therefore \frac{\delta A_s}{A_s} = \left[\left\{\frac{\delta(W + H)}{(W + H)}\right\}^2 + \left\{\frac{\delta L}{L}\right\}^2\right]^{\frac{1}{2}} \tag{D.33}$$

The uncertainty of the heat transfer coefficient is calculated below:

$$\delta\bar{h} = \left[\left(\frac{\partial\bar{h}}{\partial\dot{Q}_{out}}\delta\dot{Q}_{out}\right)^2 + \left(\frac{\partial\bar{h}}{\partial A_s}\delta A_s\right)^2 + \left(\frac{\partial\bar{h}}{\partial\Delta\bar{T}_{w,b}}\delta\Delta\bar{T}_{w,b}\right)^2\right]^{\frac{1}{2}} \tag{D.34}$$

$$\therefore \frac{\delta\bar{h}}{\bar{h}} = \left[\left(\frac{\delta\dot{Q}_{out}}{\dot{Q}_{out}}\right)^2 + \left(\frac{\delta A_s}{A_s}\right)^2 + \left(\frac{\delta\Delta\bar{T}_{w,b}}{\Delta\bar{T}_{w,b}}\right)^2\right]^{\frac{1}{2}} \tag{D.35}$$

The average Nusselt number is defined by equation (D.36).

$$\overline{Nu} = \frac{\bar{h}D_h}{k} \tag{D.36}$$

The hydraulic diameter D_h is defined in Section 2.3.1, and is given here in two forms, equation (D.37) and equation (D.38).

$$D_h = \frac{4A_c}{P_w} \tag{D.37}$$

$$\therefore D_h = \frac{4WH}{2(W + H)} \tag{D.38}$$

The resulting hydraulic diameter uncertainty equation is given below:

$$\delta D_h = \left[\left\{\frac{\partial D_h}{\partial W}\delta W\right\}^2 + \left\{\frac{\partial D_h}{\partial H}\delta H\right\}^2 + \left\{\frac{\partial D_h}{\partial (W+H)}\delta (W+H)\right\}^2\right]^{\frac{1}{2}} \quad \text{(D.39)}$$

$$\therefore \frac{\delta D_h}{D_h} = \left[\left\{\frac{\delta W}{W}\right\}^2 + \left\{\frac{\delta H}{H}\right\}^2 + \left\{\frac{\delta (W+H)}{(W+H)}\right\}^2\right]^{\frac{1}{2}} \quad \text{(D.40)}$$

The average Nusselt number uncertainty is defined below:

$$\delta \overline{Nu} = \left[\left(\frac{\partial \overline{Nu}}{\partial \bar{h}}\delta \bar{h}\right)^2 + \left(\frac{\partial \overline{Nu}}{\partial D_h}\delta D_h\right)^2 + \left(\frac{\partial \overline{Nu}}{\partial k}\delta k\right)^2\right]^{\frac{1}{2}} \quad \text{(D.41)}$$

$$\therefore \frac{\delta \overline{Nu}}{\overline{Nu}} = \left[\left(\frac{\delta \bar{h}}{\bar{h}}\right)^2 + \left(\frac{\delta D_h}{D_h}\right)^2 + \left(\frac{\delta k}{k}\right)^2\right]^{\frac{1}{2}} \quad \text{(D.42)}$$

The uncertainty of the average Nusselt number for each test section is given in Table D.6.

D.9 Reynolds number uncertainty

The Reynolds number is given by equation (D.43).

$$Re = \frac{\rho v D_h}{\mu} \quad \text{(D.43)}$$

The uncertainty of the Reynolds number is given below:

$$\delta Re = \left[\left(\frac{\partial Re}{\partial \rho}\delta \rho\right)^2 + \left(\frac{\partial Re}{\partial v}\delta v\right)^2 + \left(\frac{\partial Re}{\partial D_h}\delta D_h\right)^2 + \left(\frac{\partial Re}{\partial \mu}\delta \mu\right)^2\right]^{\frac{1}{2}} \quad \text{(D.44)}$$

$$\therefore \frac{\delta Re}{Re} = \left[\left(\frac{\delta \rho}{\rho}\right)^2 + \left(\frac{\delta v}{v}\right)^2 + \left(\frac{\delta D_h}{D_h}\right)^2 + \left(\frac{\delta \mu}{\mu}\right)^2\right]^{\frac{1}{2}} \quad \text{(D.45)}$$

The uncertainty of the Reynolds number is given in Table D.6.

D.10 Friction factor uncertainty

The friction factor is calculated as discussed in Section 3.5.1, given below in equation (D.46).

$$f = \Delta P \frac{D_h}{L_p} \frac{2}{\rho v^2} \tag{D.46}$$

The uncertainty of the friction factor is calculated below:

$$\delta f = \left[\left(\frac{\partial f}{\partial \Delta P} \delta \Delta P \right)^2 + \left(\frac{\partial f}{\partial D_h} \delta D_h \right)^2 + \left(\frac{\partial f}{\partial L_p} \delta L_p \right)^2 + \left(\frac{\partial f}{\partial \rho} \delta \rho \right)^2 + \frac{1}{4} \left(\frac{\partial f}{\partial v} \delta v \right)^2 \right]^{\frac{1}{2}} \tag{D.47}$$

$$\therefore \frac{\delta f}{f} = \left[\left(\frac{\delta \Delta P}{\Delta P} \right)^2 + \left(\frac{\delta D_h}{D_h} \right)^2 + \left(\frac{\delta L_p}{L_p} \right)^2 + \left(\frac{\delta \rho}{\rho} \right)^2 + 4 \left(\frac{\delta v}{v} \right)^2 \right]^{\frac{1}{2}} \tag{D.48}$$

The uncertainty of the friction factor is given in Table D.6.

D.11 j-factor uncertainty

The j-factor is discussed in Section 3.5.3 and is defined in equation (D.49).

$$j = \frac{\overline{Nu}}{RePr^{\frac{1}{3}}} \tag{D.49}$$

The uncertainty analysis of the j-factor is found below:

$$\delta j = \left[\left(\frac{\partial j}{\partial \overline{Nu}} \delta \overline{Nu} \right)^2 + \left(\frac{\partial j}{\partial Re} \delta Re \right)^2 + \left(\frac{\partial j}{\partial Pr} \delta Pr \right)^2 \right]^{\frac{1}{2}} \tag{D.50}$$

$$\therefore \frac{\delta j}{j} = \left[\left(\frac{\delta \overline{Nu}}{\overline{Nu}} \right)^2 + \left(\frac{\delta Re}{Re} \right)^2 + \left(\frac{\delta Pr}{Pr} \right)^2 \right]^{\frac{1}{2}} \tag{D.51}$$

The uncertainty of the Colburn j-factor is given in Table D.6.

D.12 Result uncertainties

Hydraulic diameter	*Result*	*Range [-]*	*Uncertainty [±]*
1.05 mm	*Reynolds number*	365 – 2 620	2.32% - 26.1%
	Friction factor	0.028 - 0.14	2.16% - 27.4%
	Nusselt number	3 - 16.3	4.98% - 26.4%
	Colburn j-factor	0.0018 - 0.0051	5.71% - 37.2%
0.85 mm	*Reynolds number*	371 – 3 000	2.47% - 30.1%
	Friction factor	0.029 - 0.094	2.82% - 50.7%
	Nusselt number	4.35 - 31.71	6.48% - 30.5%
	Colburn j-factor	0.0017 - 0.0049	7.11% - 42.9%
0.57 mm	*Reynolds number*	357 – 2 833	2.95% - 45.4%
	Friction factor	0.038 - 0.13	3.98% - 46.3%
	Nusselt number	2.53 - 29.84	12.6% - 45.6%
	Colburn j-factor	0.0021 - 0.0039	15.3% - 64.4%

Table D.6 Uncertainties of final results for all three test sections

D.13 References

[1] S. Kline and F. McClintock, "Describing uncertainties in single-sample experiments," *Mechanical Engineering,* vol. 75, pp. 2-8, 1953.

[2] R. Moffat, "Describing the uncertainties in experimental results," *Experimental Thermal and Fluid Science,* vol. 1, pp. 3-17, 1988.

[3] C. Popiel and J. Wojtkowiak, "Simple formulas for thermophysical properties of liquid," *Heat Transfer Engineering,* vol. 19, no. 3, pp. 87-101, 1998.

[4] R. Hocking, "8.6 Calibration," in *Methods and Applications of Linear Models: Regression and Analysis of Variance*, Hoboken, New Jersey, John Wiley & Sons, 2003, pp. 289-290.